

## **Master thesis and internship[BR]- Master's thesis : Design of a coaxial counterrotating rotor for an emergency drone[BR]- Internship**

**Auteur :** Tamburrini, Robin

**Promoteur(s) :** Hillewaert, Koen

**Faculté :** Faculté des Sciences appliquées

**Diplôme :** Master en ingénieur civil en aérospatiale, à finalité spécialisée en "aerospace engineering"

**Année académique :** 2023-2024

**URI/URL :** <http://hdl.handle.net/2268.2/21013>

---

### *Avertissement à l'attention des usagers :*

*Tous les documents placés en accès ouvert sur le site le site MatheO sont protégés par le droit d'auteur. Conformément aux principes énoncés par la "Budapest Open Access Initiative"(BOAI, 2002), l'utilisateur du site peut lire, télécharger, copier, transmettre, imprimer, chercher ou faire un lien vers le texte intégral de ces documents, les disséquer pour les indexer, s'en servir de données pour un logiciel, ou s'en servir à toute autre fin légale (ou prévue par la réglementation relative au droit d'auteur). Toute utilisation du document à des fins commerciales est strictement interdite.*

*Par ailleurs, l'utilisateur s'engage à respecter les droits moraux de l'auteur, principalement le droit à l'intégrité de l'oeuvre et le droit de paternité et ce dans toute utilisation que l'utilisateur entreprend. Ainsi, à titre d'exemple, lorsqu'il reproduira un document par extrait ou dans son intégralité, l'utilisateur citera de manière complète les sources telles que mentionnées ci-dessus. Toute utilisation non explicitement autorisée ci-avant (telle que par exemple, la modification du document ou son résumé) nécessite l'autorisation préalable et expresse des auteurs ou de leurs ayants droit.*

---



---

# Design of a Coaxial Counterrotating Rotor for an Emergency Drone

---

Author: **Robin Tamburrini**

Academic Supervisor: **Prof. Koen Hillewaert (University of Liège)**

Industry Supervisor: **Christophe Greffe (Generix)**

Master in Aerospace Engineering  
University of Liège - Faculty of Applied Sciences

**Final Thesis submitted in fulfillment of the requirements for the degree of  
Master in Civil Engineering in Aerospace Engineering  
by Robin Tamburrini**

Academic Year 2023-2024

# Abstract

This study focuses on validating and enhancing BEMT models for coaxial rotor designs. Coaxial rotors offer significant advantages in efficiency and torque cancellation, making them highly suitable for a variety of UAV applications. The research leverages the Rotare code, an open-source MATLAB implementation renowned for its versatility in analyzing rotor systems, including coaxial configurations.

The research builds upon the existing implementation in the Rotare code, introducing modifications to better account for previously neglected physical aspects. These enhancements include incorporating tangential velocity effects in rotor interactions while maintaining angular momentum conservation. Furthermore, improvements eliminate the far-field approximation where the lower rotor operates within the fully developed wake of the upper rotor. Instead, operational conditions and rotor geometry are now accurately considered in coaxial models, enhancing fidelity. A critical enhancement integrates the elimination of total torque into the code, crucial for functional design optimization.

This study validates BEMT models and coaxial models within the Rotare code for coaxial rotor designs. Validation efforts confirm the accuracy of these models. For single-rotor configurations, various solution methods demonstrate good correspondence with experimental data, with the induced velocities approach proving the most effective. Coaxial rotor models similarly align well with experimental results. The general Multiple Stream Tube (MST) model, identified for its superior fidelity in representing velocity and angle distributions while maintaining computational efficiency, is recommended as optimal for coaxial rotor design applications.

In the design phase, the study optimized coaxial rotor systems through BEMT simulations, focusing on counter-rotating coaxial rotors with SAB blades tested by Generix. Computational predictions closely matched experimental thrust measurements, validating model reliability. Torque balance predictions also aligned well with experimental data. Critical design parameters, including the collective pitch of the lower rotor, airfoil geometry, chord length, and differential blade diameters, have been identified as essential for enhancing drone performance.

# Acknowledgments

First and foremost, I would like to thank my promoter in Uliège, Professor Koen Hillewaert, for his continuous support and advice all along this project. I would also like to sincerely thank my industrial promoter at Generix, Christophe Greffe, for his availability and numerous insightful suggestions. A special thank you goes to the PhD student, Thomas Lambert, whose precious assistance at the beginning of my thesis helped me to familiarize myself with his code and effectively take it in hand. His help was crucial during the initial stages of my project. Moreover, I would like to thank Maxime Borbousse, PhD student at the University of Liège, for his presence and assistance in the development of my thesis.

Finally, I am deeply grateful to my family and close friends for their unconditional support. Their encouragement and confidence in me throughout this thesis and my entire master's program, have been invaluable.

# Contents

1	Introduction . . . . .	5
1.1	Motivation . . . . .	5
1.2	Methodology . . . . .	6
2	Theoretical Aspect . . . . .	7
2.1	Momentum Theory . . . . .	7
2.1.1	Hover . . . . .	7
2.1.2	Axial climb . . . . .	9
2.1.3	Axial descent and upflow . . . . .	10
2.2	Blade Element Theory . . . . .	11
2.3	Blade Element Momentum theory . . . . .	13
2.4	Tip loss correction . . . . .	15
2.5	Performance characterisation . . . . .	16
2.5.1	Operating point parameters . . . . .	16
2.5.2	Performance parameters . . . . .	17
2.6	Solvers . . . . .	17
2.6.1	Small Angle Approximations . . . . .	18
2.6.2	Induction factor . . . . .	20
2.6.3	Induced velocity . . . . .	22
2.6.4	Single equation . . . . .	24
2.7	Coaxial rotor systems . . . . .	25
2.7.1	Single Streamtube (SST) . . . . .	26
2.7.2	Multiple Streamtubes models . . . . .	28
3	Improvements . . . . .	30
3.1	Incorporation of tangential velocity induced by the upper rotor on the lower rotor . . . . .	30
3.2	Wake contraction . . . . .	31
3.3	Torque cancelation . . . . .	35
4	Model Validation . . . . .	37
4.1	Single rotor . . . . .	37
4.1.1	Convergence with the number of elements . . . . .	37
4.1.2	Comparison of the solvers . . . . .	38
4.1.3	Stall analysis . . . . .	43
4.1.4	Impact of the polars . . . . .	45
4.2	Coaxial rotor . . . . .	48

4.2.1	Overall assessment of predictive performance validity . . . .	48
4.2.2	Impact of the incorporation of tangential velocity induced by the upper rotor on the lower rotor. . . . .	53
4.2.3	Impact of the wake contraction . . . . .	54
4.2.4	Comparison of the coaxial models . . . . .	60
4.3	Summary . . . . .	66
5	Design . . . . .	67
5.1	The effect of variation in differential collective pitch. . . . .	69
5.2	The effect of the variation of the airfoil geometry. . . . .	70
5.3	The effect of the variation of the chord length. . . . .	71
5.4	The effect of the variation of the inter-rotor distance. . . . .	71
5.5	The effect of the variation in differential blade diameters. . . . .	72
6	Conclusion . . . . .	74
<b>Bibliography</b>		<b>76</b>
<b>A BEMT Configurations</b>		<b>79</b>

# 1 Introduction

## 1.1 Motivation

The development of unmanned aerial vehicles (UAVs) has seen significant advancements in recent years, driven by the need for improved performance in various applications such as surveillance, delivery, and agricultural monitoring. Among the diverse UAV configurations, coaxial rotor designs have emerged as a promising alternative, particularly for their potential to overcome the limitations faced by small UAV designers in terms of energy efficiency and aerodynamic performance. This study focuses on the validation of Blade Element Momentum Theory (BEMT) models with the objective of utilizing them to accurately compute the performance of coaxial rotors, thereby facilitating their design and optimization.

Coaxial rotors, defined as a pair of counter-rotating rotors rotating about a common shaft axis [1], have a long history. It begins with Igor Sikorsky's non-piloted prototype in 1909 and further developments by pioneers like Corradine d'Asconio in 1930 [2]. Despite their early promise, coaxial rotors were not widely adopted in the industry due to the complexity of their rotor hub design, which made manufacturing and maintenance more challenging and expensive compared to simpler main-tail rotor configurations. Russian manufacturer Kamov successfully produced coaxial rotor helicopters from the late 1940s, though these were not designed for high-speed operations. In the 1970s, the Sikorsky X-59 introduced the Advancing Blade Concept (ABC), achieving improved efficiency at high speeds by balancing lift between advancing and retreating blades [3]. While the X-59 did not enter production, Sikorsky's X2 Technology Demonstrator (X2 TD) revitalized the ABC concept with modern technologies, relaunching interest in coaxial rotors.

Coaxial rotors offer several advantages that are particularly relevant for UAVs [4]. One of the primary motivations for investigating coaxial rotors is their superior lift-to-drag ratio, which translates to greater efficiency in hover, forward flight, and maneuvering than single rotors of the same solidity and blade geometry [3, 5]. This efficiency is crucial for UAVs that require extended flight times and improved aerodynamic performance to meet operational demands.

The contra-rotating nature of coaxial rotors provides intrinsic torque cancellation, eliminating the need for a tail rotor or electronic stabilization systems. This configuration allows for a larger lift capacity for a given rotor diameter, which is particularly advantageous in applications where vehicle size is constrained, such as in urban environments or naval operations [6]. The ability to generate higher lift within a compact footprint makes coaxial rotors ideal for UAVs that need to operate in confined spaces.

## 1.2 Methodology

The methodology for this study builds upon Lambert’s thesis [7] and leverages the Rotare code, a feature-rich and open-source implementation of the Blade Element Momentum Theory (BEMT) in MATLAB. Originally developed for teaching purposes, this code supports the analysis and design of various rotors, including helicopter main/tail rotors, aircraft propellers, and wind/tidal turbines. Over time, the code has been expanded to incorporate different solvers, numerous extensions to the base methodology, and the ability to handle more complex geometries, transforming it into a comprehensive analysis tool applicable beyond academic settings. This robust foundation allows for an in-depth exploration and enhancement of coaxial rotor systems in the present research.

Initially, the theoretical aspects related to BEMT are revisited. This includes an in-depth discussion of the Momentum Theory and Blade Element Theory, along with the addition of the Prandtl-Glauert tip loss correction. The various models used to solve the nonlinear equations of BEMT are thoroughly described. Furthermore, different models that account for interactions between rotors in the coaxial case are explored in detail, providing a solid theoretical foundation for subsequent analyses.

Building on the existing implementation in the Rotare code, modifications are introduced to better account for certain physical aspects that have been previously neglected. These modifications include considering the tangential velocity in rotor interactions while conserving angular momentum. Additionally, the current version of the code assumed the far-field condition where the lower rotor is positioned within the fully developed wake of the upper rotor. The improvement involves eliminating this approximation and taking into account the operational conditions and rotor geometry when considering the interaction in the coaxial models. A last significant enhancement involves integrating the elimination of total torque into the code. This final step was necessary to achieve a functional design.

Then, the methodology proceeds to compare and verify the validity of the models for a simple case consisting of a single rotor. This step is crucial as it establishes the reliability and accuracy of the models in a controlled and simplified scenario. Once the models are validated for the simple rotor case, the focus shifts to the coaxial rotor system. Here, the validity of the models is again compared and verified, but this time in the context of the interactions between the upper and lower rotors.

Finally, the methodology involves identifying factors that could impact the performance of a coaxial rotor system. This analysis, based on insights derived from the code and current literature, seeks to identify potential pathways for design optimization.



## 2 Theoretical Aspect

### 2.1 Momentum Theory

Drones, as rotating-wing vehicles, must navigate through a variety of flight regimes including hovering, climbing, descending, and forward motion. These vehicles also can perform complex maneuvers that integrate these fundamental flight modes. One of the key aspects of drone operation is during hover or axial flight, where the airflow through the rotor is axisymmetric, moving either upward or downward, indicating no lateral or longitudinal movement. This condition is generally the simplest to analyze and should theoretically be the easiest to predict using mathematical models. However, even with advanced modeling techniques for rotor airflow, accurately predicting a drone's hover performance remains a challenging task. It is essential to recognize that the actual physical airflow around the rotor involves a complex vortical wake structure. Despite the complexities, the essential functionality of the rotor can be assessed using the simpler momentum theory. This approach allows for an initial estimate of the rotor's thrust and power, providing a foundational basis for more detailed investigations into rotor aerodynamics.

The Momentum theory, also called Actuator Disk Theory or Rankine-Froude Theory, simplifies the analysis of propeller behavior by abstracting away the complexities of its physical shape and intricate flow dynamics near the blades. Instead, it focuses on the global flow passing through the rotor. In the general approach of this theory, the assumption is made that the flow passing through the rotor adheres to certain characteristics: it is considered one-dimensional, quasi-steady, incompressible, and inviscid.

#### 2.1.1 Hover

Initially, the analysis will be focused on a single rotor operating in a hover state. In this scenario, the drone maintains zero forward speed and zero vertical speed, focusing purely on the aerodynamics of stationary flight in an upright position.

The following procedure, derived from Leishman [2], adapts the general equations of fluid mass, momentum, and energy to analyze a hovering drone rotor. Referring to Figure 1, cross-section 0 indicates the plane far upstream of the rotor, where the fluid remains still in the hovering scenario ( $V_c = 0$ ). The rotor disk area is labeled  $A$ , with cross-sections 1 and 2 situated just above and below the rotor disk, and cross-section  $\infty$  representing the "far" wake. At the rotor plane, the induced velocity, or the velocity imparted to the air mass at the rotor disk, is denoted as  $v_i$ . In the far wake, this velocity increases and is symbolized by  $w$ .

Assuming quasi-steady flow and applying the principle of conservation of mass, the mass flow rate,  $\dot{m}$ , must be constant within the rotor wake (control volume). Thus, the mass flow rate is expressed as

$$\dot{m} = \iint_0 \rho \mathbf{V} \cdot d\mathbf{S} = \iint_2 \rho \mathbf{V} \cdot d\mathbf{S}, \quad (2.1)$$

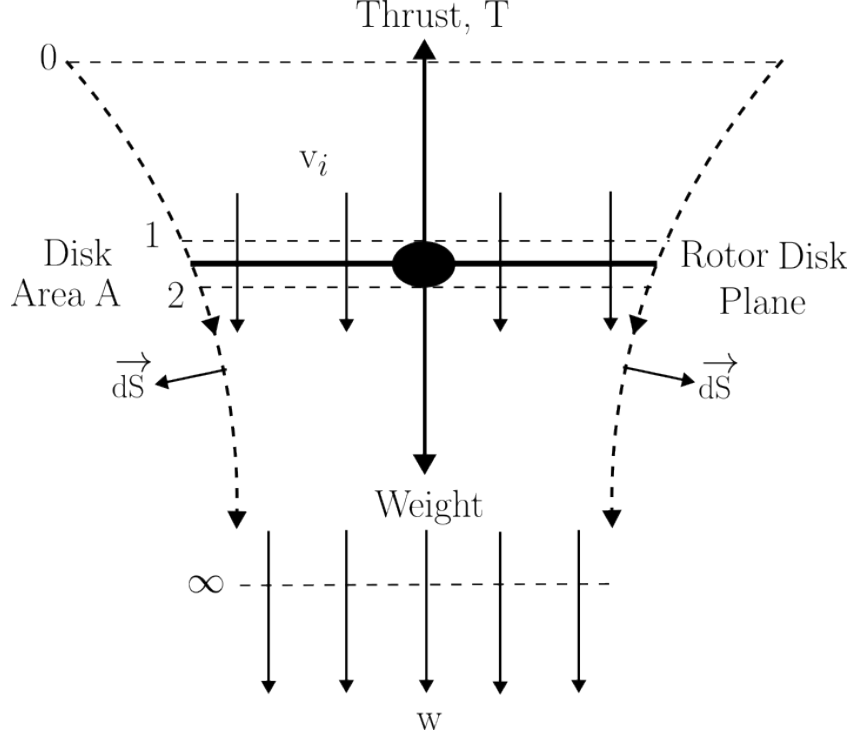


Figure 1: Flow model for momentum theory analysis of a rotor in hovering flight.

which, under the assumption of 1-D incompressible flow, simplifies to

$$\dot{m} = \rho A_0 V_c = \rho A_2 v_i = \rho A_\infty w. \quad (2.2)$$

Using the principle of conservation of momentum, the rotor thrust,  $T$ , is related to the net rate of change of fluid momentum within the control volume, as per Newton's second law. The thrust is the force exerted on the fluid, given by

$$T = \iint_{\infty} (\rho \mathbf{V} \cdot d\mathbf{S}) \mathbf{V} - \iint_0 (\rho \mathbf{V} \cdot d\mathbf{S}) \mathbf{V}. \quad (2.3)$$

For hovering flight, the upstream velocity  $V_c$  is zero, simplifying the thrust to

$$T = \iint_{\infty} (\rho \mathbf{V} \cdot d\mathbf{S}) \mathbf{V} = \dot{m} w. \quad (2.4)$$

The principle of conservation of energy states that the work done on the rotor equals the increase in the energy of the fluid per unit of time. The power consumed by the rotor is given by  $T v_i$ , leading to the equation

$$T v_i = \iint_{\infty} \frac{1}{2} (\rho \mathbf{V} \cdot d\mathbf{S}) \mathbf{V}^2 - \iint_0 \frac{1}{2} (\rho \mathbf{V} \cdot d\mathbf{S}) \mathbf{V}^2. \quad (2.5)$$

For hover, with  $V_c = 0$ , this reduces to

$$T v_i = \int_2^\infty \frac{1}{2} (\rho \mathbf{V} \cdot d\mathbf{S}) \mathbf{V}^2 = \frac{1}{2} \dot{m} w^2. \quad (2.6)$$

From equations 2.4 and 2.6, we derive that

$$v_i = \frac{1}{2} w, \quad (2.7)$$

or  $w = 2v_i$ , providing a direct relationship between the induced velocity at the rotor plane,  $v_i$ , and the velocity  $w$  in the far wake. Thus, the thrust is given by:

$$T = \dot{m} w = \dot{m} (2v_i) = 2(\rho A v_i) v_i = 2\rho A v_i^2. \quad (2.8)$$

### 2.1.2 Axial climb

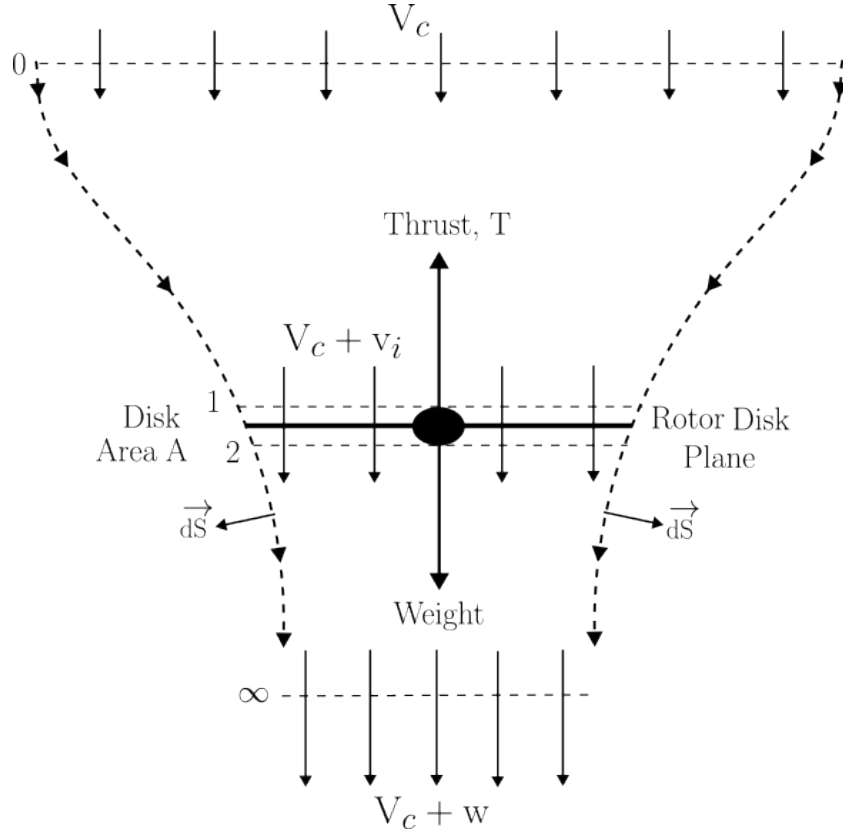


Figure 2: 2D model representation.

In this case, the three conservation laws will be now applied to a control volume surrounding the climbing rotor and its flow field, as illustrated in Figure 2. Assuming a quasi-1-D problem, we consider the flow properties to vary only in the vertical direction over cross-sectional planes parallel to the disk, with uniform distribution at each cross-section. Unlike the hover

case, where the climb velocity is zero, the relative velocity far upstream relative to the rotor is  $V_c + v_i$ , and the slipstream velocity in the vena contracta is now  $V_c + w$ . Then, by the conservation of mass, the mass flow rate is constant within the boundaries of the wake and so

$$\dot{m} = \iint_{\infty} \rho \mathbf{V} \cdot d\mathbf{S} = \iint_2 \rho \mathbf{V} \cdot d\mathbf{S} \quad (2.9)$$

$$= \rho A_{\infty}(V_c + w) = \rho A(V_c + v_i). \quad (2.10)$$

The application of the principle of conservation of momentum gives

$$T = \iint_{\infty} (\rho \mathbf{V} \cdot d\mathbf{S}) \mathbf{V} - \iint_0 (\rho \mathbf{V} \cdot d\mathbf{S}) \mathbf{V} \quad (2.11)$$

$$= \dot{m}(V_c + w) - \dot{m}V_c = \dot{m}w. \quad (2.12)$$

Notice that this is the same equation obtained for the rotor thrust in the hover case (Eq. 2.4). Because the work done by the climbing rotor is now  $T(V_c + v_i)$ , then

$$T(V_c + v_i) = \iint_{\infty} \frac{1}{2}(\rho \mathbf{V} \cdot d\mathbf{S}) \mathbf{V}^2 - \iint_0 \frac{1}{2}(\rho \mathbf{V} \cdot d\mathbf{S}) \mathbf{V}^2 \quad (2.13)$$

$$= \frac{1}{2} \dot{m}(V_c + w)^2 - \frac{1}{2} \dot{m}V_c^2 \quad (2.14)$$

$$= \frac{1}{2} \dot{m}w(2V_c + w). \quad (2.15)$$

From equations 2.12 and 2.15, it can be seen that:

$$V_c + v_i = \frac{1}{2}(2V_c + w), \quad (2.16)$$

and

$$v_i = \frac{1}{2}w, \quad (2.17)$$

Therefore, the thrust is now given by:

$$T = \dot{m}w = \rho A(V_c + v_i)w = 2\rho A(V_c + v_i)v_i. \quad (2.18)$$

### 2.1.3 Axial descent and upflow

In a descent (where  $V_c < 0$ ), the climb flow model cannot be used because  $V_c$  is directed upward, placing the slipstream above the rotor. This situation arises whenever  $|V_c|$  exceeds twice the average induced velocity at the disk. Within the range  $-2v_h \leq V_c \leq 0$ , where  $v_h$  is the induced velocity in hover, the velocity at any plane through the rotor slipstream can be either upward or downward.

Under these conditions, a more complex recirculating flow pattern, which is often more turbulent and aperiodic, known as Vortex Ring State (VRS), may occur at the rotor. Momentum theory is not applicable because it is impossible to establish a definitive control volume surrounding the rotor and its wake. This same limitation applies to the blade element momentum theory (BEMT). Due to the complexities and unique characteristics of descent conditions, Rotare does not allow a negative operating speed.

In certain cases, some blade sections may experience a negative effective angle of attack even when the axial velocity remains positive. For instance, a proprotor in hover or operating at low forward speeds demonstrates this scenario [8]. A coaxial rotor can also experience this phenomenon in the region affected by the upper rotor. This creates an upflow on those sections due to the negative induced velocity, resulting in negative thrust and energy extraction from the flow. To maintain consistency with mass flow and momentum balances, these sections should be treated as if they were in a descent scenario, while other sections should be treated as if they were in a general axial climb or hover condition.

It is impractical to change conventions within a single simulation based on section position or iteration number. Therefore, Rotare uses a consistent approach by always following the default convention, where  $\infty$  is above the rotor and  $w$  is below it. The absolute value of the mass flow is used in the thrust equations. This method allows for negative induced velocities when necessary and is crucial when predicting an upflow through the rotor annulus. Therefore, the thrust is defined as:

$$T = 2\rho A|V_c + v_i|v_i. \quad (2.19)$$

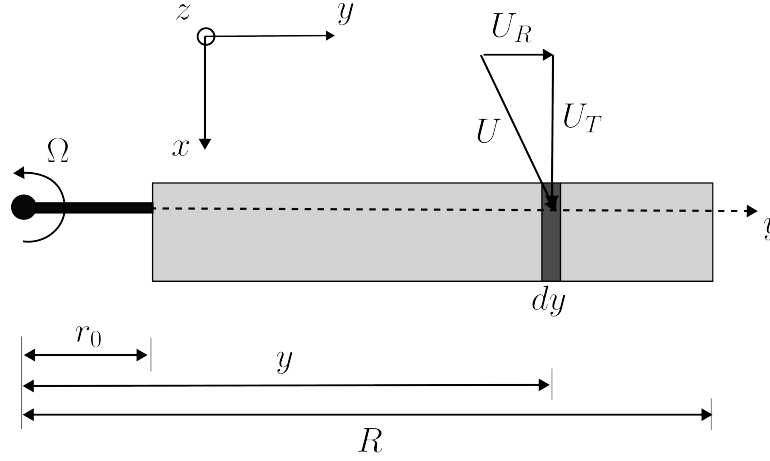
## 2.2 Blade Element Theory

The blade element theory (BET) is an essential tool for analyzing any rotor aerodynamics. It supports nearly all modern computational methods used for rotor performance, airloads, and aeroelastic analyses. BET operates by representing the airloads on 2-D sections of the blades and integrating their effects to determine the rotor's overall performance. This approach offers significant flexibility, allowing for detailed examination of airfoil shape effects, Reynolds number, Mach number, and nonlinear aerodynamic phenomena, including stall.

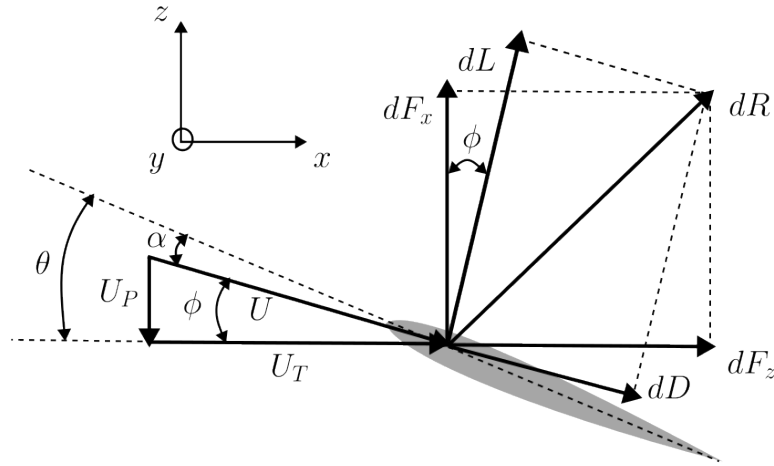
BET provides estimates of radial and azimuthal distributions of aerodynamic loading across the rotor disk. It assumes each blade section behaves as a quasi-2D airfoil generating aerodynamic forces and moments. By integrating sectional airloads over the blade length and averaging over a rotor revolution, BET facilitates rotor blade design, considering blade twist, platform distribution, and airfoil shape to achieve desired rotor performance.

Figure 3 illustrates the flow environment and aerodynamic forces on a representative blade element of the rotor. These aerodynamic forces are assumed to arise solely from the velocity and the angle of attack normal to the leading edge of the blade section. The 2-D aerodynamic characteristics of the airfoil, dependent on the angle of attack and the Reynolds number, can

be found in the airfoil database. The inflow angle of attack,  $\phi$ , primarily results from the velocity induced by the rotor and its wake. Consequently, the induced velocity modifies the direction of the relative flow velocity vector, altering the angle of attack at each blade element from its 2-D value. This induced velocity also tilts the local lift vectors, which act perpendicular to the resultant velocity vector at the blade element. This tilting generates induced drag and is the source of the induced power required at the rotor shaft.



(a) Top view of the blade.



(b) Blade element.

Figure 3: Incident velocities and aerodynamic environment at a typical blade element.

The resultant local flow velocity at any blade element at a radial distance  $y$  from the rotational axis has an out-of-plane component  $U_P = V_c + v_i$  normal to the rotor as a result of climb and induced inflow, and an in-plane component  $U_T = \Omega y$  parallel to the rotor due to blade rotation relative to the disk plane. The resultant velocity at the blade element is, therefore,

$$U = \sqrt{U_T^2 + U_P^2}. \quad (2.20)$$

The relative inflow angle (or induced angle of attack) at the blade element will be

$$\phi = \tan^{-1} \left( \frac{U_P}{U_T} \right) \approx \frac{U_P}{U_T}, \quad \text{for small angles.} \quad (2.21)$$

Thus, if the pitch angle at the blade element is  $\theta$ , then the aerodynamic or effective angle of attack is

$$\alpha = \theta - \phi. \quad (2.22)$$

The resultant incremental lift  $dL$  and drag  $dD$  per unit span on this blade element are

$$dL = \frac{1}{2} \rho U^2 c C_L dy, \quad \text{and} \quad dD = \frac{1}{2} \rho U^2 c C_D dy, \quad (2.23)$$

where  $C_L$  and  $C_D$  are the lift and drag coefficients, respectively, and  $c$  is the local blade chord. These forces act perpendicular and parallel to the resultant flow velocity, respectively. Resolving these forces perpendicular and parallel to the rotor disk plane gives

$$dF_z = dL \cos \phi - dD \sin \phi, \quad \text{and} \quad dF_x = dL \sin \phi + dD \cos \phi. \quad (2.24)$$

Therefore, the contributions to the thrust, torque, and power of the rotor are

$$dT = N_b dF_z, \quad dQ = N_b dF_x y, \quad \text{and} \quad dP = N_b dF_x \Omega y, \quad (2.25)$$

where  $N_b$  is the number of blades comprising the rotor. In hover or axial flight conditions, substituting the results for  $dF_x$  and  $dF_z$  gives

$$dT = N_b (dL \cos \phi - dD \sin \phi), \quad (2.26)$$

$$dQ = N_b (dL \sin \phi + dD \cos \phi) y, \quad (2.27)$$

$$dP = N_b (dL \sin \phi + dD \cos \phi) \Omega y. \quad (2.28)$$

### 2.3 Blade Element Momentum theory

The Blade Element Momentum Theory (BEMT) combines the principles of blade element theory (BET) and Momentum Theory (MT) to compute thrust and torque in rotating wing systems. This method divides rotor blades into small segments, calculating the aerodynamic characteristics (lift, drag, and moment) of each segment based on theoretical models or empirical data. By integrating these incremental loads, the total thrust, torque, and power consumption of the rotor are determined.

Consider first the application of the conservation laws to an annulus of the rotor disk, as shown in as shown in Figure 4. This is the essence of Freud's original differential theory for propellers in axial motion. This annulus is at a distance  $y$  from the rotational axis and has a width  $dy$ . The area of this annulus is, therefore,  $dA = 2\pi y dy$ . The incremental thrust,  $dT$ , on this annulus may be calculated based on simple momentum theory and with the 2-D assumption that successive rotor annuli have no mutual effects on each other. As might be expected, this approach has good validity except near the blade tips. The removal of this 2-D restriction requires a considerably more advanced treatment of the problem using a vortex wake theory. However, a good approximation to the tip-loss effect on the inflow distribution can be made using Prandtl's "circulation-loss" function.

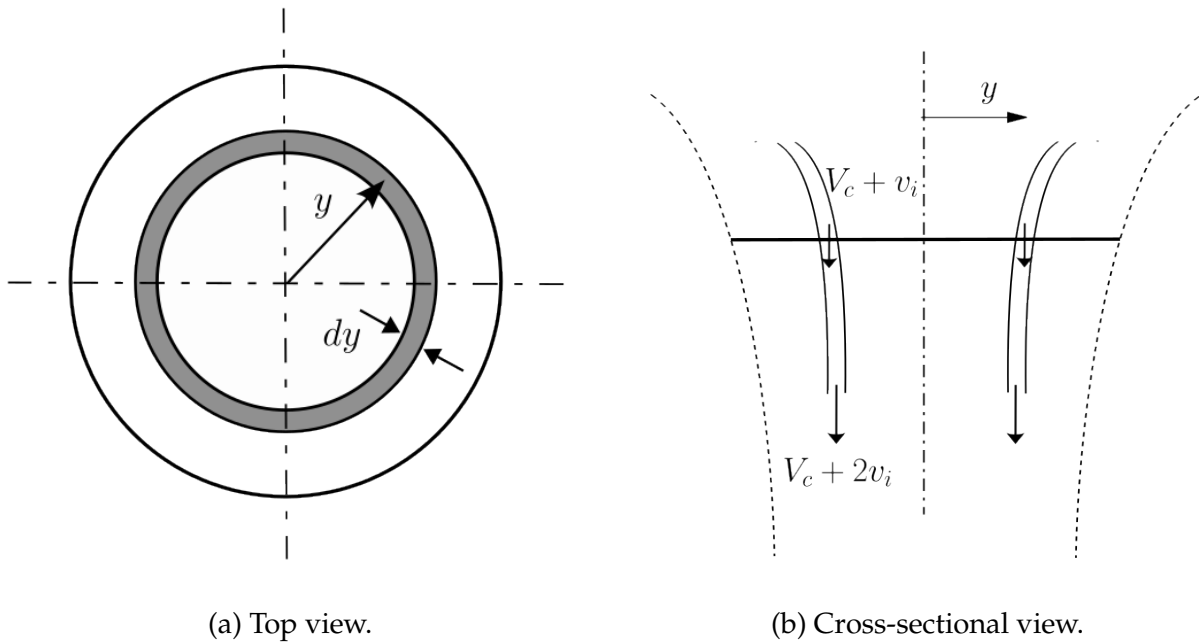


Figure 4: Annulus of rotor disk as used for a local momentum analysis of the hovering rotor.

Based on the simple one-dimensional momentum theory, we may compute the incremental thrust on the rotor annulus as the product of the mass flow rate through the annulus and the induced velocity at that section. In this case, the mass flow rate over the annulus of the disk is

$$d\dot{m} = \rho A(V_c + v_i) = 2\pi\rho(V_c + v_i) y dy. \quad (2.29)$$

As discussed in section 2.1.3, the absolute value of the mass flow is taken to prevent the cases where negative induced velocities occur. Therefore, incremental thrust on the annulus is given by

$$dT = |d\dot{m}|v_i \quad (2.30)$$

$$= 4\pi\rho|V_c + v_i|v_i y dy. \quad (2.31)$$



The incremental torque is defined as the product of an incremental radial force ( $|d\dot{m}|(u_2 - u_1)$ ) and its lever arm ( $y$ ).

$$dQ = |d\dot{m}|(u_2 - u_1)y \, dy \quad (2.32)$$

$$= 4\pi\rho|V_c + v_i|u_i y^2 \, dy. \quad (2.33)$$

The combination of Blade Element Theory (BET) and Momentum Theory (MT) results in the following system of equations:

$$\begin{cases} N_b(dL \cos \phi - dD \sin \phi) &= 4\pi\rho|V_c + v_i|v_i y \, dy, \\ N_b(dL \sin \phi + dD \cos \phi)y &= 4\pi\rho|V_c + v_i|u_i y^2 \, dy. \end{cases} \quad (2.34)$$

## 2.4 Tip loss correction

The Blade Element Momentum Theory (BEMT) assumes the flow is inviscid, incompressible, steady, irrotational, and moves uniformly from upstream to downstream. It models the wind rotor as a rotating actuator disk, representing an infinite number of blades, allowing continuous airflow and causing a pressure jump at the disk. This simplification assumes that forces on an annulus are only due to the local pressure jump, implying no flow interaction between annuli and uniform thrust across the rotor area. The wake is modeled as a cylinder rotating oppositely to the rotor. These assumptions limit BEMT's accuracy, especially near the blade tips where flow is non-uniform.

To correct these limitations, the Prandtl-Glauert tip loss factor is introduced. This factor accounts for the reduced efficiency near the blade tips due to the helical wake structure and non-uniform flow and is often used in the literature (see [8, 9, 10]). It uses conformal mapping to describe the curved flow around the wake sheets, initially modeled as flow around a circle. By mapping this to a flat plate, Prandtl derived a factor describing the non-uniform flow's impact, which Glauert simplified for practical use in BEMT, such as:

$$F_{\text{tip}} = \frac{2}{\pi} \arccos \left( \exp \left( -\frac{N_b}{2} \frac{R - r}{r} \frac{1}{|\sin \phi|} \right) \right). \quad (2.35)$$

Additionally, the flow near the root of the blade, like the tip, experiences unique aerodynamic effects that aren't captured by the standard BEMT assumptions. The flow interaction at the root can lead to increased drag and reduced lift. To correct for these root effects, a root correction factor is applied. Thus, for each blade element, the total induced velocity must incorporate both the tip loss and root loss corrections. Buhl extended Glauert's empirical relation to include these factors, ensuring that the calculations reflect the combined impact of tip and root losses. This is expressed as:

$$F = \frac{2}{\pi} \arccos \left( e^{-f_{\text{tip}} \cdot f_{\text{root}}} \right).$$

Where,

$$f_{\text{tip}} = \frac{N_b}{2} \frac{R - r}{r |\sin \phi|}, \quad (2.36)$$

$$f_{\text{tip}} = \frac{N_b}{2} \frac{r - r_0}{r |\sin \phi|}. \quad (2.37)$$

However, at  $\phi = 90^\circ$  for  $dC_T$  and  $\phi = 0^\circ$  for  $dC_P$ , the tip vortices do not contribute to the induced velocities  $w_i$  and  $u_i$ . To account for this physical behavior, the expressions for the decreases in thrust and power should gradually decrease to zero as the angles between the tip vortex axes and the blade force vectors decrease. Consequently, the differential momentum theory equations for the thrust and power coefficients can be modified to read

$$dT = 4\pi\rho K_T |V_c + v_i| v_i y \, dy, \quad (2.38)$$

$$dQ = 4\pi\rho K_T |V_c + v_i| u_i y^2 \, dy. \quad (2.39)$$

Where,

$$K_T = [1 - (1 - F) \cos \phi], \quad (2.40)$$

$$K_P = [1 - (1 - F) \sin \phi]. \quad (2.41)$$

Consequently, the system of equation 2.34 becomes:

$$\begin{cases} N_b(dL \cos \phi - dD \sin \phi) = 4\pi\rho K_T |V_c + v_i| v_i y \, dy, \\ N_b(dL \sin \phi + dD \cos \phi) y = 4\pi\rho K_T |V_c + v_i| u_i y^2 \, dy. \end{cases} \quad (2.42)$$

## 2.5 Performance characterisation

To facilitate comparisons between rotors with varying geometries and operating under different conditions, performance metrics are typically expressed using nondimensional coefficients. However, due to the diverse range of rotor applications, the focus points can vary significantly among helicopters, aircraft propellers, and wind turbines. As a result, different definitions for performance metrics arise depending on the application type. Adding to the complexity, the conventional definitions of helicopter coefficients generally include an additional factor of  $1/2$  in the denominator in most regions of the world, except for the United States.

### 2.5.1 Operating point parameters

First, the parameters that concern the operation point are considered. The first one is the advance ratio, which is proportional to the ratio between the flight speed and the tip rotational speed. It is defined differently depending on whether it applies to helicopters or propellers.

$$\text{Helicopter: } \gamma = \frac{V_\infty}{\Omega R} \quad (2.43)$$

$$\text{Propeller: } J = \frac{V_\infty}{nD} \quad (2.44)$$

where  $\Omega$  and  $n$  are, respectively, measured in radians and rotations per second. The advance ratio can also be defined as the ratio of the forward distance covered by the air to the tangential distance traveled by the rotor tip during a single revolution. Additionally, there is the Reynolds number, which is used to determine the flow conditions and that is defined as:

$$Re = \frac{\rho U c}{\mu}. \quad (2.45)$$

### 2.5.2 Performance parameters

The performance parameters, such as the thrust, torque, and power coefficients, are also dependent on the application type: helicopter, propeller, or wind turbine. Note that the last one will not be of interest in this study. The definitions of these coefficients, depending on whether they apply to helicopters or propellers, are summarized in Table 1.

Table 1: Force, moment, and power coefficients definitions for helicopter rotor and propeller applications. Greyed out 1/2 factor only used in non-US convention.

	Thrust $C_T$	Torque $C_Q$	Power $C_P$
<b>Helicopters</b>	$\frac{T}{\frac{1}{2}\rho A(\Omega R)^2}$	$\frac{Q}{\frac{1}{2}\rho A\Omega^2 R^3}$	$\frac{P}{\frac{1}{2}\rho A(\Omega R)^3}$
<b>Propellers</b>	$\frac{T}{\rho n^2 D^4}$	$\frac{Q}{\rho n^2 D^5}$	$\frac{P}{\rho n^3 D^5}$

Note that for coaxial rotor systems, particular attention must be paid to the parameters by which the numbers are made dimensionless when considering the total system performance. If the contributions of each rotor are to be added, they must be nondimensionalized by the same speed, the same radius, and so on.

## 2.6 Solvers

The system of equation 2.42 is inherently nonlinear, necessitating numerical methods for solution. Over time, several strategies have been proposed to address this complexity, each with its own advantages and drawbacks. Among these strategies, four are commonly encountered. The first involves making supplementary assumptions to linearize the system, while the remaining three approaches the base equations from different angles, ultimately leading to equivalent results.

### 2.6.1 Small Angle Approximations

The small angles approximation method, introduced by Leishman [2], linearizes the system to enable an analytical solution for the inflow velocity.

This methodology uses the following simplifying assumptions:

1. The out-of-plane velocity  $U_P$  is much smaller than the in-plane velocity  $U_T$ , so  $U = \sqrt{U_T^2 + U_P^2} \approx U_T$ . This approximation holds except near the blade root, where the aerodynamic forces are negligible.
2. The induced angle  $\phi$  is small, such that  $\phi = U_P/U_T$ . Additionally,  $\sin \phi \approx \phi$  and  $\cos \phi \approx 1$ . Given the small angles assumption, the lift coefficient is treated as a linear function of the effective angle of attack, expressed as  $c_l(\alpha) = c_{l\alpha}\alpha$ . If it is assumed that the airfoil follows thin airfoil theory, the lift curve slope is directly established as  $c_{l\alpha} = 2\pi \text{ rad}^{-1}$ . However, in practical cases, Leishman suggests using  $5.73 \text{ rad}^{-1}$  to account for finite thickness and Reynolds number effects. Under the small angle assumption, the drag coefficient can be assumed constant and equal to  $c_{d0}$ .
3. Finally, due to the small inflow angle, the drag is considered at least an order of magnitude less than the lift, resulting in  $dD \cos \phi \approx dD$  and  $dD \sin \phi \approx 0$ .

Applying these simplifications to equations 2.26-2.28 results in

$$dT = N_b dL, \quad (2.46)$$

$$dQ = N_b (\phi dL + dD) y, \quad (2.47)$$

$$dP = N_b \Omega(\phi dL + dD) y. \quad (2.48)$$

Proceeding further, it is convenient to introduce nondimensional quantities by dividing lengths by  $R$  and velocities by  $\Omega R$ . This leads to the nondimensional radius  $r$  and the axial inflow ratio  $\lambda$ . These quantities are defined as follows:

$$r = \frac{y}{R} \quad \text{and} \quad \lambda = \frac{V_c + v_i}{\Omega R}. \quad (2.49)$$

Similarly, it is convenient to define the induced velocity ratio  $\lambda_i = -v_i/(\Omega R)$  as well as the axial velocity ratio  $\lambda_c = V_c/(\Omega R)$ . Additionally, the local solidity can be defined as:

$$\sigma_l = \frac{N_b c(r)}{2\pi y} \quad (2.50)$$

which should not be confused with the global solidity, reduced to  $\sigma = N_b c/(\pi R)$ , corresponding to untapered blades. Finally, note that the performance coefficients will be considered using their definitions specific to the helicopter case.

Using these new assumptions and definitions, the momentum equation 2.38 can be rewritten as:

$$dC_T = \frac{dT}{\rho A (\Omega R)^2} = \frac{4\pi \rho K_T |V_c + v_i| v_i y dy}{\rho \pi R^2 (\Omega R)^2}, \quad (2.51)$$

$$= 4F |V_c + v_i| \lambda_i r dr, \quad (2.52)$$

$$= 4F |\lambda_c + \lambda_i| \lambda_i r dr, \quad (2.53)$$

$$= 4F |\lambda| (\lambda - \lambda_c) r dr. \quad (2.54)$$

Similarly, the elementary thrust and torque coefficients which were obtained by blade element theory and simplified using small inflow angle assumption (Eqs. 2.46-2.48) can be reformulated as follows:

$$dC_T = \frac{dT}{\rho A (\Omega R)^2} = \frac{N_b dL}{\rho A (\Omega R)^2}, \quad (2.55)$$

$$= \frac{N_b \left( \frac{1}{2} \rho U^2 c_l(\alpha) c dy \right)}{\rho \pi R^2 (\Omega R)^2}, \quad (2.56)$$

$$= \frac{N_b c}{2\pi R} \frac{U_T^2}{(\Omega R)^2} c_l d \left( \frac{y}{R} \right), \quad (2.57)$$

$$= \frac{N_b c}{2\pi y} r \left( \frac{\Omega y}{\Omega R} \right)^2 c_{l,\alpha} dr, \quad (2.58)$$

$$= \sigma_l r^3 c_l (\beta - \alpha_0 - \phi) dr, \quad (2.59)$$

$$= \sigma_l r^2 c_l (r(\beta - \alpha_0) - \lambda) dr. \quad (2.60)$$

$$dC_Q = \frac{dQ}{\rho A \Omega^2 R^3} = \frac{N_b (dL\phi + dD) y}{\rho A \Omega^2 R^3}, \quad (2.61)$$

$$= \frac{N_b dL}{\rho A (\Omega R)^2} \frac{\phi y}{R} + \frac{N_b \left( \frac{1}{2} \rho U^2 c_d(\alpha) c dy \right)}{\rho A \Omega^2 R^3}, \quad (2.62)$$

$$= dC_T \frac{\phi y}{R} + \frac{N_b c_l}{2\pi R} \frac{U_T^2}{(\Omega R)^2} c_d \frac{y}{r} \left( d \frac{y}{R} \right), \quad (2.63)$$

$$= dC_T \phi r + \sigma_l \left( \frac{\Omega y}{\Omega R} \right)^2 c_d r^2 dr, \quad (2.64)$$

$$= dC_T \lambda + \sigma_l c_d r^4 dr. \quad (2.65)$$

$$dC_P = \frac{dP}{\rho A \Omega^2 R^3} = \frac{N_b \Omega (dL\phi + dD) y}{\rho A (\Omega R)^3}, \quad (2.66)$$

$$= \frac{N_b (dL\phi + dD) y}{\rho A \Omega^2 R^3} = dC_Q. \quad (2.67)$$

where  $c_d = c_{d0}$  under the small angle assumption. Having reformulated the thrust coefficient using the blade element and moment theories under the new assumptions, Eq. 2.54 and Eq. 2.60 can now be set equal to each other:

$$4F|\lambda|(\lambda - \lambda_c)r dr = \sigma_l r^2 c_l (r(\beta - \alpha_0) - \lambda) dr. \quad (2.68)$$

Rearranging the terms provides a quadratic equation in  $\lambda$ :

$$\lambda^2 + (\mathbb{B} - \lambda_c)\lambda - \mathbb{B}r(\beta + \alpha_0) = 0. \quad (2.69)$$

where,

$$\mathbb{B} = \text{sgn}(\lambda) \frac{\sigma_l r c_l}{4F}. \quad (2.70)$$

Since  $\mathbb{B}$  explicitly depends on the sign of  $\lambda$ , there are two potential solutions. However, it is possible to pre-determine the correct solution by evaluating Eq. 2.69 at  $\lambda = 0^+$  as follows:

$$\mathbb{H}(\lambda = 0^+) = -\mathbb{B}(\lambda = 0^+)r(\beta + \alpha_0), \quad (2.71)$$

$$= \frac{\sigma_l r^2 c_l}{4F}(\beta + \alpha_0). \quad (2.72)$$

If  $\mathbb{H}(0^+) < 0$ , then the inflow ratio  $\lambda$  must necessarily be positive and is given by:

$$\lambda^+(r, \lambda_c) = \sqrt{\left(\frac{\mathbb{B}^+}{2} - \frac{\lambda_c}{2}\right)^2 + \mathbb{B}^+r(\beta + \alpha_0)} - \left(\frac{\mathbb{B}^+}{2} - \frac{\lambda_c}{2}\right). \quad (2.73)$$

If  $\mathbb{H}(0^+) > 0$ , then the inflow ratio  $\lambda$  is negative and is given by:

$$\lambda^-(r, \lambda_c) = \sqrt{\left(\frac{-\mathbb{B}^+}{2} - \frac{\lambda_c}{2}\right)^2 - \mathbb{B}^+r(\beta + \alpha_0)} - \left(\frac{-\mathbb{B}^+}{2} - \frac{\lambda_c}{2}\right), \quad (2.74)$$

where  $\mathbb{B}^+ = \mathbb{B}(\lambda \geq 0)$ . It should be noted, however, that the analytical expression for  $\lambda$  still depends on the tip-loss factor  $F$ , which, in turn, depends on the inflow angle (and thus  $\lambda$ ). Therefore, if the calculation includes the tip-loss correction, it must be solved iteratively. Once the inflow ratio is determined, the total thrust, torque, and power can be computed using the equations of the blade element theory (Eqs. 2.60, 2.65 and 2.67).

## 2.6.2 Induction factor

This solver is frequently used (see [9, 11]) since it does not require additional assumptions, but instead reformulates the momentum equations using induction factors. This approach simplifies the expressions and is relatively intuitive. However, its primary drawback is that the resulting equations are not directly applicable to the analysis of rotors at zero external

velocity, such as helicopters in hover or propellers in idle. The equations are derived by initially defining the axial and tangential (swirl) induction factors:

$$a = \frac{v_i}{V_c} \quad \text{and} \quad b = \frac{u_i}{\Omega y}. \quad (2.75)$$

It leads to:

$$U_P = (1 + a) V_c, \quad (2.76)$$

$$U_T = (1 - b) \Omega y. \quad (2.77)$$

Additionally, integrating this change of variable in equations 2.38 and 2.39, we find:

$$dT = 4\pi\rho |V_c + v_i| v_i y dy, \quad (2.78)$$

$$= 4\pi\rho \left| 1 + \frac{v_i}{V_c} \right| \frac{v_i}{V_c} V_c^2 y dy, \quad (2.79)$$

$$= 4\pi\rho |1 + a| a V_c^2 y dy. \quad (2.80)$$

and

$$dQ = 4\pi\rho |V_c + v_i| u_i y^2 dy, \quad (2.81)$$

$$= 4\pi\rho \left| 1 + \frac{v_i}{V_c} \right| (b \Omega y) V_c y^2 dy, \quad (2.82)$$

$$= 4\pi\rho |1 + a| b \Omega y^3 dy. \quad (2.83)$$

The system of equations 2.34 becomes:

$$N_b (dL \cos \phi - dD \sin \phi) = 4\pi\rho |1 + a| a V_c^2 y dy, \quad (2.84)$$

$$N_b (dL \sin \phi + dD \cos \phi) y = 4\pi\rho |1 + a| b \Omega y^3 dy, \quad (2.85)$$

where the inflow angle is now defined as follows:

$$\phi = \tan^{-1} \left( \frac{U_P}{U_T} \right) = \tan^{-1} \left( \frac{(1 + a) V_c}{(1 - b) \Omega y} \right). \quad (2.86)$$

For each annulus, the axial induction factor  $a(r)$  and angular induction factor  $b(r)$  can now be calculated with an iterative algorithm:

1. Assume initial values for  $a_0(r)$  and  $b_0(r)$ .
2. Compute the inflow angle  $\phi_n(r)$  with equation 2.86.
3. Compute the angle of attack  $\alpha_n(r)$  with equation 2.22.
4. Compute the velocity components  $U_{p,n}(r)$  and  $U_{T,n}(r)$  based on equations 2.76 and 7 as well as the velocity magnitude  $U_n(r)$ :

$$U_n(r) = \sqrt{U_{P,n}(r)^2 + U_{T,n}(r)^2}. \quad (2.87)$$

5. Compute the angle of attack  $\alpha$  with equation 2.22 and the Reynolds numbers  $Re_n$  with:

$$Re_n(r) = \frac{\rho_d U_n(r) c(r)}{\mu}. \quad (2.88)$$

6. Determine the lift coefficient  $c_l$  and drag coefficient  $c_d$  corresponding to the calculated angle of attack using airfoil data, and therefore the lift and drag forces:

$$dL_n(r) = c_l(\alpha_n(r), Re_n(r)) \frac{1}{2} \rho_d U_n(r)^2 c dr, \quad (2.89)$$

$$dD_n(r) = c_d(\alpha_n(r), Re_n(r)) \frac{1}{2} \rho_d U_n(r)^2 c dr. \quad (2.90)$$

7. Calculate new values for the axial induction factor  $a_{n+1}(r)$  and angular induction factor  $b_{n+1}(r)$ :

$$a_{n+1}(r) = \frac{N_b (dL_n(r) \cos \phi_n(r) - dD_n(r) \sin \phi_n(r))}{4K_T \pi \rho V_c^2 |1 + a_n(r)| y dy}, \quad (2.91)$$

$$b_{n+1}(r) = \frac{N_b (dL_n(r) \sin \phi_n(r) + dD_n(r) \cos \phi_n(r)) y}{4K_P \pi \rho V_c |1 + a_n(r)| \Omega y^3 dy}. \quad (2.92)$$

8. As long as the induction factors change more than a specified tolerance throughout an iteration, we start again at point 1. If the results are accepted, the thrust and torque force can be calculated with equations 2.80, 2.83 respectively.

### 2.6.3 Induced velocity

This solver directly resolves the system of equations (cf. Eqs 2.34) without extensive rewriting or added assumptions. Although it is somewhat more formal, it is advantageous because it can be applied to any flow condition. However, it is rarely seen in the literature [12], probably due to its apparent complexity. Since,  $v_i = U_P - V_c$ , the momentum equations (Eqs 2.38-2.39) can be rewritten as:

$$dT = 4\pi \rho U_P (U_P - V_c) y dy, \quad (2.93)$$

$$dQ = 4\pi \rho U_P U_T y^2 dy. \quad (2.94)$$

Or, such that

$$dT = 2d\dot{m} (U_P - V_c), \quad (2.95)$$

$$dQ = 2d\dot{m} U_T y. \quad (2.96)$$

And, we know that:

$$U_P = \frac{V_c + U_{P,+}}{2}, \quad (2.97)$$

$$U_T = \frac{U_{T,+}}{2}, \quad (2.98)$$



where  $U_{P,+}$  and  $U_{T,+}$  denote, respectively, the axial and tangential velocities immediately downstream of the disk. Therefore,

$$dT = 2d\dot{m} \frac{U_{P,+} - V_c}{2} = d\dot{m} (U_{P,+} - V_c), \quad (2.99)$$

$$dQ = 2d\dot{m} \frac{U_{T,+}}{2} y = d\dot{m} U_{T,+} y. \quad (2.100)$$

The computation of the radial variation of thrust and torque needs to be done iteratively for each considered radius. We need to iteratively determine  $U_{P,+}(r)$  and  $U_{T,+}(r)$  such that the momentum balances are satisfied (cf. Eqs 2.99 and 2.100). The iterative procedure proceeds as follows:

1. We start with initial estimates for  $U_{P,0+}(r)$  and  $U_{T,0+}(r)$ .
2. First, we compute the velocity components at the propeller disk:

$$U_{P,n}(r) = \frac{V_c + U_{P,n-}(r)}{2}, \quad (2.101)$$

$$U_{T,n}(r) = \Omega R - \frac{U_{T,n+}(r)}{2}. \quad (2.102)$$

3. Then, we find the local mass flow:

$$d\dot{m}(r) = 2\pi r dr \rho_d U_{P,n}(r). \quad (2.103)$$

4. From the relative velocity components, we first compute new estimates for the velocity magnitude  $U_n(r)$  and flow angle  $\beta_n(r)$ :

$$U_n(r) = \sqrt{U_{P,n}(r)^2 + U_{T,n}(r)^2}, \quad (2.104)$$

$$\phi_n(r) = \tan^{-1} \left( \frac{U_{P,n}(r)}{U_{T,n}(r)} \right). \quad (2.105)$$

Combined with the local pitch angle  $\theta$  and chord  $c(r)$ , we compute the angle of attack  $\alpha_n(r)$  and Reynolds number  $Re_n(r)$ :

$$\alpha_n(r) = \theta(r) - \phi_n(r), \quad (2.106)$$

$$Re_n(r) = \frac{\rho_d U_n(r) c(r)}{\mu}, \quad (2.107)$$

which allow us to determine the lift and drag coefficients  $c_l$  and  $c_d$  from the airfoil polar, and therefore the lift and drag forces:

$$dL_n(r) = c_l(\alpha_n(r), Re_n(r)) \frac{1}{2} \rho_d U_n(r)^2 c(r) dr. \quad (2.108)$$

$$dD_n(r) = c_d(\alpha_n(r), Re_n(r)) \frac{1}{2} \rho_d U_n(r)^2 c(r) dr. \quad (2.109)$$

Then, the contribution of the thrust and the torque can be obtained from equations 2.26

5. From the forces, we find new approximations for the absolute velocity components:

$$U_{P,n+1,+}(r) = U_{P,n}(r) + \frac{dT_n(r)}{d\dot{m}_n(r)}, \quad (2.110)$$

$$U_{T,n+1,+}(r) = \frac{dQ_n(r)}{d\dot{m}_n(r)} + U_c(r). \quad (2.111)$$

6. As long as the velocity components change more than a specified tolerance throughout an iteration, we start again at point 1.

The iteration can be initiated by assuming  $U_{P,0+}(r) = U_{P,0-}(r)$  and  $U_{T,0+}(r) = 0$ .

#### 2.6.4 Single equation

Rather than solving the system of equations 2.42 concurrently, Winarto [13] proposed expressing the thrust and power equations in terms of the inflow angle  $\psi$ , combining them into a single transcendental equation. This reduces the problem to solving only one equation. Stahlhut and Leishman [8] later expanded this method to include tip losses and account for potential upflow in the normal working state. Using the small angle approximation, this approach begins by rewriting the momentum equations (Eqs. 2.38 and 2.39) and BEM equations (Eq. 2.26 and 2.27) in terms of nondimensional quantities. In addition to the nondimensional quantities used in the small angle approximation method (cf. Eq ??), the swirl ratio  $\xi = (U_T + u_i)/(\Omega R)$  will also be used. Therefore, the system 2.42 begins:

$$\begin{cases} \sigma_l r \frac{U^2 (c_l \cos \phi - c_d \sin \phi)}{(\Omega R)^2} dr = 4 K_T |\lambda| (\lambda - \lambda_c) r dr, \\ \sigma_l r^2 \frac{U^2 (c_l \sin \phi + c_d \cos \phi)}{(\Omega R)^2} dr = 4 K_P |\lambda| (r - \xi) r^2 dr. \end{cases} \quad (2.112)$$

By defining  $\tan \gamma = c_d/c_l$ , while also nondimensionalizing by  $(\Omega R)^2$ , we obtain:

$$\begin{cases} \sigma_l U^2 c_l \sec \gamma (\cos \gamma \cos \phi - \sin \gamma \sin \phi) = 4 K_T U \sin |\phi| (U \sin \phi - V_c), \\ \sigma_l U^2 c_l \sec \gamma (\sin \gamma \sin \phi + \cos \gamma \cos \phi) = 4 K_P U \sin |\phi| (U \cos \phi - \Omega y). \end{cases} \quad (2.113)$$

Using the identities  $\cos(\phi + \gamma) = \cos \phi \cos \gamma - \sin \phi \sin \gamma$  and  $\sin(\phi + \gamma) = \sin \gamma \sin \phi + \cos \gamma \cos \phi$  the above system can be rearranged into the form

$$\begin{cases} \frac{1}{8 K_T} \frac{1}{r} \sigma U c_l \sec \gamma \csc |\phi| \cos(\phi + \gamma) = U \sin \phi - V_c, \\ \frac{1}{8 K_P} \frac{\sigma}{r} c_l \sec \gamma \csc |\phi| \sin(\phi + \gamma) = -U \cos \phi - \Omega y. \end{cases} \quad (2.114)$$

Based on this system of equation, the function  $\mathbb{B}_1(\phi)$  and  $\mathbb{B}_2(\phi)$  can be defined:

$$\mathbb{B}_1(\phi) = \frac{V_c}{U} = \sin \phi - \frac{1}{4 K_T} \frac{\sigma}{r} c_l \sec \gamma \csc |\phi| \cos(\phi + \gamma), \quad (2.115)$$

$$\mathbb{B}_2(\phi) = \frac{\Omega y}{U} = \cos \phi + \frac{1}{4 K_P} \frac{\sigma}{r} c_l \sec \gamma \csc |\phi| \sin(\phi + \gamma). \quad (2.116)$$

Both functions  $\mathbb{B}_1(\phi)$  and  $\mathbb{B}_2(\phi)$  can be combined into a single transcendental equation

$$g(\phi) = [\mathbb{B}_1(\phi) \Omega y - \mathbb{B}_2(\phi) V_c] \sin \phi = 0. \quad (2.117)$$

Or

$$g(\phi) = (\Omega y \sin \phi - V_\infty \cos \phi) \sin \phi, \\ - \operatorname{sgn}(\phi) \frac{\sigma c_l \sec \gamma}{8 r} \left[ \frac{\Omega y}{K_T} \cos(\phi + \gamma) + \frac{V_\infty}{K_P} \sin(\phi + \gamma) \right]. \quad (2.118)$$

In Eq. 2.118, the inflow angle  $\phi$  is the only unknown. The values of  $C_l$ ,  $C_d$ ,  $K_T$ , and  $K_P$  are functions of several variables, with  $\phi$  being the sole unknown. Once the inflow angle has been determined, the inflow ratios  $\lambda$  and  $\xi$  can be evaluated, enabling the calculation of the thrust and torque for each element. To ensure better convergence, the Rotare code uses the bisection method to solve this function. This approach is recommended over fixed-point iteration, which is more prone to convergence issues, ensuring reliable and consistent results.

## 2.7 Coaxial rotor systems

In a coaxial rotor system, interactions between the rotors and their wakes create a more complex flow field compared to a single rotor. The upper rotor affects the lower one, and vice versa; the lower rotor induces a slight additional velocity over the entire upper rotor. For lightly loaded rotors, this impact can be reasonably neglected, allowing the upper rotor to be analyzed as if it were operated in isolation. This study adopts this assumption, as it is usually done throughout the literature on coaxial rotors [2], thereby avoiding iterative system-wide approaches.

Regarding the influence of the upper rotor on the lower one, since the lower rotor operates in the vena contracta of the upper rotor, the inner area of the lower rotor encounters incoming stream tubes with an upstream velocity dependent on the upper rotor, denoted  $U_{P,w}$ . Figure 5 shows that the upstream velocity of the lower rotor, denoted as  $V_\perp$ , can be composed as:

$$V_\perp = \begin{cases} U_{P,w}, & \text{for } y_{hub} < y < y_c, \\ V_c, & \text{for } y > y_c. \end{cases} \quad (2.119)$$

Thus, the methodology adopted in this study involves initially solving the upper rotor as if it were operating in isolation, followed by the resolution of the lower rotor, where the axial velocity component  $V_c$  is substituted with  $V_\perp$  within the different solvers. The primary challenge lies in accurately determining the upstream velocity and the resultant stream tube

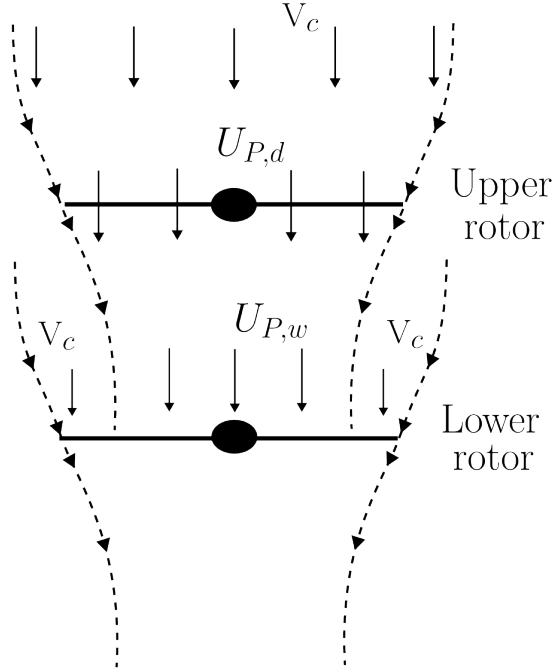


Figure 5: Flow model for a coaxial rotor analysis.

contraction induced by the upper rotor. This issue can be addressed by employing either a single stream tube approach (see Figure 6a), as in the single stream tube model (SST), or by using multiple stream tubes (see Figure 6b), as in the general multiple stream tubes model (MST) or the simplified multiple stream tube model (SMST).

In each case, the lower rotor is assumed to be positioned within the fully developed wake of the upper rotor. Therefore, based on the momentum theory (cf. equation 2.17), the axial velocity in the wake  $U_{P,w}$  can be rewritten as:

$$U_{P,w} = V_c + w, \quad (2.120)$$

$$= V_c + 2v_i, \quad (2.121)$$

$$= 2(V_c + v_i) - V_c, \quad (2.122)$$

$$= 2U_{P,d} - V_c. \quad (2.123)$$

### 2.7.1 Single Streamtube (SST)

A straightforward approach is the single stream tube (SST) model, also referred as the simple momentum theory. This model is based on the assumption of a constant axial velocity upstream of the second rotor while ignoring the wake swirl velocity. Figure 6a illustrates the velocities for this model.

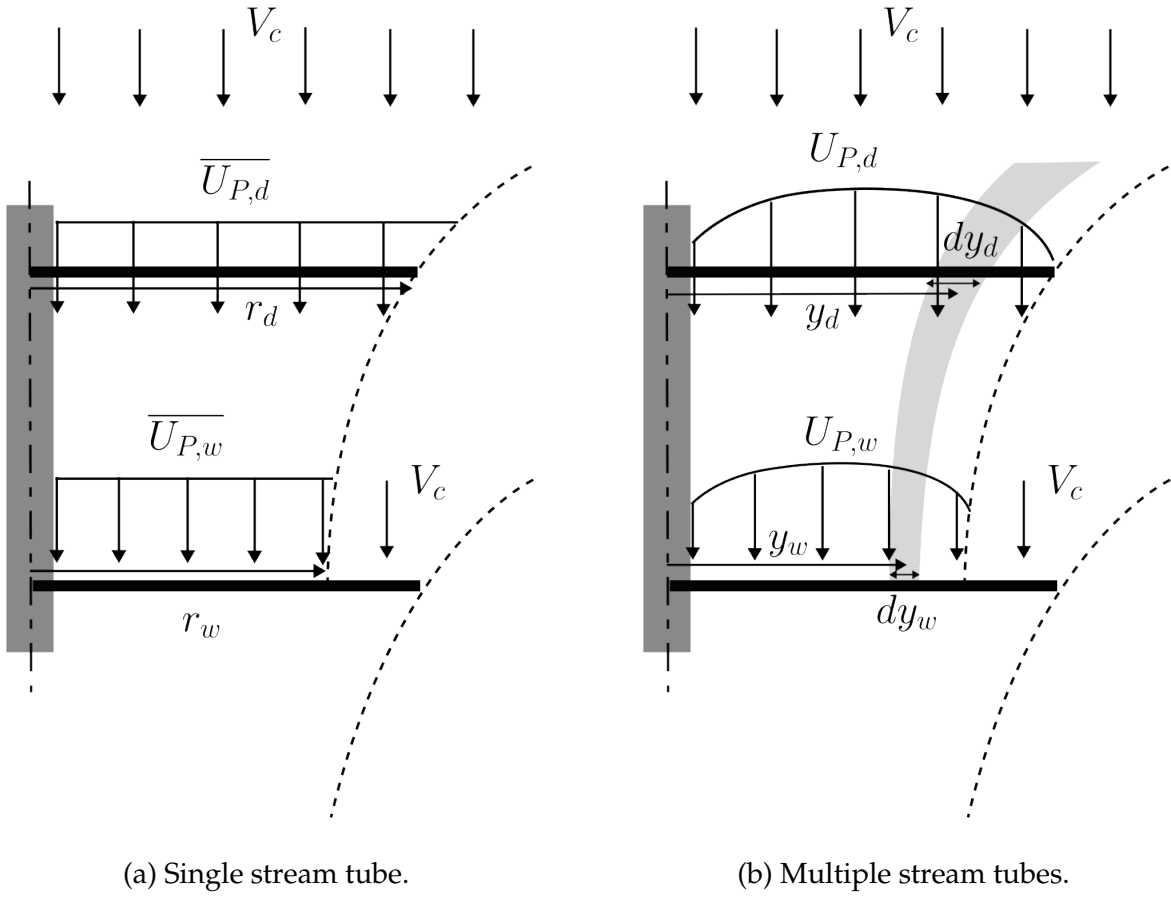


Figure 6: Coaxial models representation.

In this case, the axial velocity in the wake  $U_{P,w}$  in equation 2.123 simplifies:

$$\overline{U}_{P,w} = 2\overline{U}_{P,d} - V_c. \quad (2.124)$$

By conservation of mass, we have:

$$\dot{m}_w = \dot{m}_d, \quad (2.125)$$

$$A_w \overline{U}_{P,w} = A_d \overline{U}_{P,d}, \quad (2.126)$$

$$2\pi r_w^2 \overline{U}_{P,d} = 2\pi r_d^2 \overline{U}_{P,w}. \quad (2.127)$$

By defining the nondimensional radial contraction of the upper wake, denoted as  $a$ , as

$$a = \frac{r_w}{r_d}. \quad (2.128)$$

It comes:

$$a = \sqrt{\frac{\overline{U}_{P,d}}{\overline{U}_{P,w}}} = \sqrt{\frac{\overline{U}_{P,d}}{2\overline{U}_{P,d} - V_c}}. \quad (2.129)$$

### 2.7.2 Multiple Streamtubes models

It is important to emphasize that these models do not exist in the literature and have been specifically developed by Lambert [7]. Within the multiple stream tube models, each stream tube undergoes contraction in relation to the thrust it produces. Consequently, the velocity is no longer uniform within the wake of the upper rotor.

$$U_{P,w}(y) = 2U_{P,d}(y) - V_c. \quad (2.130)$$

Therefore, the principle of mass flow conservation between the disk and the wake can be applied for each annulus of the upper rotor

$$d\dot{m}_w(y) = d\dot{m}_d(y), \quad (2.131)$$

$$dA_w(y) U_{P,w}(y) = dA_d(y) U_{P,d}(y), \quad (2.132)$$

$$2\pi y_w dy_w^2 U_{P,w}(y) = 2\pi y_d dy U_{P,d}(y), \quad (2.133)$$

$$y_w dy_w = a(y)^2 y_d dy. \quad (2.134)$$

Where  $a(y)$  is the contraction ratio specific to each annulus:

$$a(y) = \sqrt{\frac{U_{P,d}(y)}{U_{P,w}(y)}} = \sqrt{\frac{U_{P,d}(y)}{2U_{P,d}(y) - V_c}}. \quad (2.135)$$

#### Simplified Multiple Streamtubes (SMST)

It is apparent from Eq. 2.134 that the contraction affects both the mean radius of the annulus  $y_w$  and its width  $dy_w$ . A simplified multiple stream tube (SMST) model can be derived by postulating that the mean radii and widths of all annuli identically undergo contraction. Under this assumption, the solution is simplified, allowing the center position and the width of each stream tube to be directly determined:

$$y_w = a(y) y_d \quad \text{and} \quad dy_w = a(y) dy_d. \quad (2.136)$$

#### General Multiple Streamtubes (MST)

Within the general MST model, the calculation of tube radius and width can be performed iteratively, proceeding from the innermost tube to the outermost one. As the tubes are impermeable, each tube lies perfectly against the previous one. This boundary condition offers a direct means to establish the connection between the tube's mean radius and width. For any given annulus indexed as  $i$ , the following relations can be established:

$$y_i - \frac{dy_i}{2} = y_{i-1} + \frac{dy_{i-1}}{2}. \quad (2.137)$$

Incorporating this relation into the equation 2.134, it leads to:

$$\left[ \left( y_{w,i-1} + \frac{dy_{w,i-1}}{2} \right) + \frac{dy_{w,i}}{2} \right] dy_{w,i} = y_{d,i} dy_{d,i} a(y)^2. \quad (2.138)$$

By developing this equation, it leads to the following second-order equation:

$$dy_{w,i}^2 + 2dy_{w,i} \left( y_{w,i-1} + \frac{dy_{w,i-1}}{2} \right) - y_{d,i} dy_{d,i} a(y)^2 = 0. \quad (2.139)$$

Whose solution is:

$$dy_{w,i} = - \left( y_{w,i-1} + \frac{dy_{w,i-1}}{2} \right) \pm \sqrt{\left( y_{w,i-1} + \frac{dy_{w,i-1}}{2} \right)^2 + 2 y_{d,i} dy_{d,i} a(y)^2}. \quad (2.140)$$

The negative solution is excluded since the width must be positive. The thickness and post-contraction radius of the first annulus can be computed by initiating from the innermost radius. Indeed, since the rotor hub is also assumed to be impermeable, the inner wall of the first tube must maintain a straight alignment against it.

$$y_0 - \frac{dy_0}{2} = y_{\text{hub}}. \quad (2.141)$$

Subsequently, this process is repeated iteratively for each successive annulus, progressing outward until the last one is reached.

### 3 Improvements

#### 3.1 Incorporation of tangential velocity induced by the upper rotor on the lower rotor

In the upper rotor, a tangential velocity is induced and, although it is calculated by the different solvers, it has not been accounted for on the lower rotor until now.

As illustrated in Figure 7, the velocity before the first rotor is zero, and thus the velocity just behind the disk can be directly obtained with:

$$U_{T,d+} = 2 U_{T,d}. \quad (3.1)$$

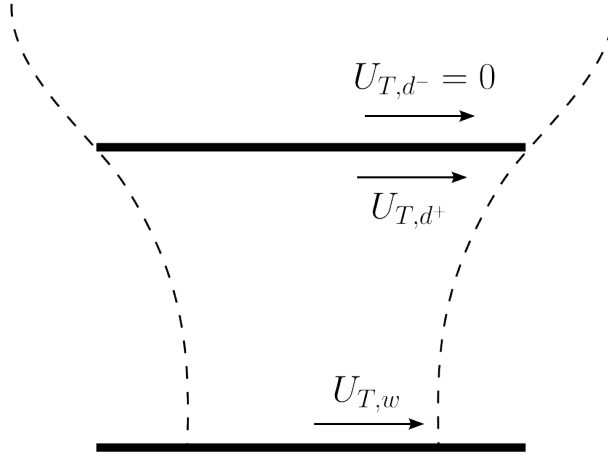


Figure 7: Tangential velocity distribution before and after the first rotor.

By conservation of angular momentum, this velocity increases as the wake contracts. Therefore, it is given by:

$$y_w U_{T,w}(y) = y_d U_{T,d+}(y), \quad (3.2)$$

$$U_{T,w}(y) = 2 \frac{y_d}{y_w} U_{T,d}(y). \quad (3.3)$$

Once the tangential velocity upstream of the lower rotor is calculated, it is added to or subtracted from the rotational speed of the lower rotor depending on the direction of rotation of the rotors. If they rotate in the same direction, the tangential velocity will negatively contribute to the second rotor. However, if a contra-rotating coaxial rotor system is considered, as in the case of interest in this study, the opposite occurs, the upstream tangential velocity will positively contribute and further increase the rotation of the second rotor. Therefore, the methodology applied will consist of calculating the tangential velocity in the wake of the first rotor. This velocity will then be respectively added to or subtracted from the rotational speed  $\Omega y$  depending on whether the rotors are contra-rotating or not.



### 3.2 Wake contraction

Until now, it was assumed that the lower rotor was positioned within the fully developed wake of the upper rotor. When the distance between the two rotors is reduced, the upstream velocity at the second rotor  $U_{P,w}$  is no longer equivalent to  $V_c + w$ , and therefore, Equation 2.123 is no longer valid. By starting from the definition of thrust and applying the conservation equations, a new definition of  $U_{P,w}$  can be derived. The thrust is defined as:

$$T = A_d (p_d^+ - p_d^-). \quad (3.4)$$

From the conservation of axial momentum, it is found that:

$$T = \dot{m} (U_{P,w} - V_c) = \rho A_d U_{P,d} (U_{P,w} - V_c). \quad (3.5)$$

Therefore, it follows that:

$$p_d^+ - p_d^- = \rho U_{P,d} (U_{P,w} - V_c). \quad (3.6)$$

Under the assumption of no losses in the upstream and downstream sections of the rotor, the Bernoulli equation can be used to calculate the change in static pressure across the rotor:

$$p_\infty + \frac{1}{2} \rho V_c^2 = p_d^- + \frac{1}{2} \rho U_{P,d}^2 \quad \text{and} \quad p_d^+ + \frac{1}{2} \rho U_{P,d}^2 = p_w + \frac{1}{2} \rho U_{P,w}^2. \quad (3.7)$$

Thus, it is found that:

$$p_d^+ - p_d^- = \frac{1}{2} \rho (U_{P,w}^2 - V_c^2) + (p_w - p_\infty). \quad (3.8)$$

By combining Equations 3.6 and 3.8, the following equation is obtained:

$$\rho U_{P,d} (U_{P,w} - V_c) = \frac{1}{2} \rho (U_{P,w}^2 - V_c^2) + (p_w - p_\infty). \quad (3.9)$$

This can be rewritten as a quadratic equation for  $U_{P,w}$ :

$$U_{P,w}^2 - 2U_{P,d} U_{P,w} - V_c^2 + 2V_c U_{P,d} + \frac{2}{\rho} (p_w - p_\infty) = 0. \quad (3.10)$$

The solution to this quadratic equation is:

$$U_{P,w} = \frac{2U_{P,d} \pm \sqrt{U_{P,d}^2 - 4 \left( V_c^2 + 2V_c U_{P,d} + \frac{2}{\rho} (p_w - p_\infty) \right)}}{2}, \quad (3.11)$$

$$= \frac{2U_{P,d} \pm \sqrt{4(U_{P,d} - V_c)^2 - \frac{8}{\rho} (p_w - p_\infty)}}{2}, \quad (3.12)$$

$$= U_{P,d} \pm \sqrt{(U_{P,d} - V_c)^2 - \frac{2}{\rho} (p_w - p_\infty)}. \quad (3.13)$$

By conservation of mass, the velocity at the disk  $U_{P,d}$  will increase as the tube contracts. Therefore, the unique final solution is:

$$U_{P,w} = U_{P,d} + \sqrt{(U_{P,d} - V_c)^2 - \frac{2}{\rho}(p_w - p_\infty)}. \quad (3.14)$$

Note that in the far-field case, where  $p_w = p_\infty$ , Equation 2.123 is retrieved. Conversely, when  $p_w > p_\infty$ , the axial velocity  $U_{P,w}$  is reduced. In the context of the blade element momentum theory, it is not feasible to determine the exact pressure value upstream of the second rotor. Consequently, an empirical formula may be employed to directly determine the wake contraction ratio. This formula should incorporate the distance between the two rotors, denoted as  $H$ , along with the operating conditions such as the rotational speed ( $\Omega$ ), the advance ratio ( $\gamma$ ), the pitch angle ( $\alpha_0$ ), and the thrust coefficient ( $C_T$ ). These considerations can be translated into the following relations:

$$a = \frac{r_w}{r_d} = f(H, \Omega, \gamma, \alpha_0, C_T). \quad (3.15)$$

To address this, Anton J. Landgrebe [14] conducted a comprehensive analytical and experimental investigation to systematically acquire data on model rotor performance and wake geometry in hovering conditions. The tests encompassed a wide range of rotor configurations, including variations in the number of blades, blade planform shapes, and twist. Throughout this study, various analytical methods were rigorously evaluated, and an empirical formula was derived based on the experimental wake data. Indeed, for the hovering case, the tip vortex radial coordinate can be accurately represented by the following equation:

$$a = A + (1 - A)e^{-\lambda\psi_w}. \quad (3.16)$$

In this equation, the constant  $A$  was determined to be 0.78, while the constant  $\lambda$  can be expressed as a function of the rotor thrust coefficient  $C_T$  only, which must be computed specifically for helicopter applications (refer to Table 1):

$$\lambda = 0.145 + 27 C_T. \quad (3.17)$$

It should be noted that these values were chosen to accurately fit the near-wake radial coordinates. Note that in equation 3.16,  $\psi_w$  represents the wake azimuth angle, which is equivalent to the blade azimuth travel from the time it generates the vortex cross-section and can be defined as:

$$\psi_w = \Omega \frac{H}{U_P}. \quad (3.18)$$

Figure 8 illustrates the evolution of wake contraction as a function of the wake azimuthal angle and the thrust coefficient. It is evident that an increase in the azimuthal angle of the wake, corresponding to an increased distance between the rotors, results in the contraction asymptotically approaching a value of 0.78. This convergence occurs more rapidly with higher thrust coefficients. The observed value of 0.78 deviates from the theoretical far-field

value ( $a = \sqrt{1/2}$ ). However, this value aligns more closely with experimental observations [2]. This phenomenon is primarily a consequence of fluid viscosity, the non-uniform inflow affecting the rotor disk, and a small swirling component of velocity induced in the wake by the spinning rotor blades.

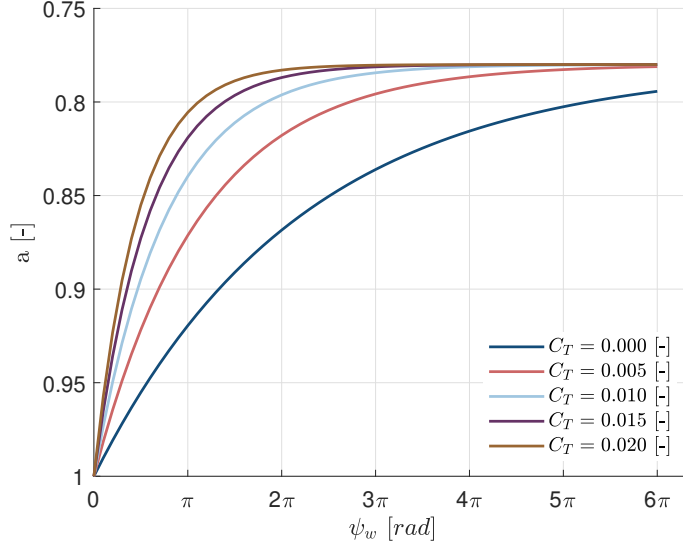


Figure 8: Evolution of the wake contraction with the wake azimuthal angle and the thrust coefficient.

As previously mentioned, the empirical modeling of the trailing vortex geometry primarily concerns the hovering flight case. Only a few investigations have focused on axial or forward flight. An example of empirical modeling of the propeller wake, sufficiently comprehensive to serve as input data for a free wake analysis code, is provided by Favier [15]. Based on analogous work [14, 16], the propeller wake has been investigated over a wide range of thrust coefficients and operating conditions, specifically with angles of attack ( $\alpha_0$ ) ranging from  $23^\circ$  to  $32.5^\circ$ , and advance ratios ( $\gamma$ ) between 0.2 and 1.1. The propeller used is a model of an aerial quad-blade propeller, of the MARQUIS type, with blades defined by the NACA 64A408 airfoil series. Based on this study, the contraction of the tip vortex has been synthesized according to the following expression:

$$a = A + (1 - A)e^{-\psi_w/B}. \quad (3.19)$$

Where,

$$A(\alpha_0, \gamma) = P_A(\gamma) + \alpha_0 Q_A(\gamma), \quad (3.20)$$

$$B(\alpha_0, \gamma) = P_B(\gamma) + \alpha_0 Q_B(\gamma). \quad (3.21)$$

The terms depending on  $\gamma$  are second-degree polynomials of the form:

$$\begin{aligned}
P_A(\gamma) &= a_0 + a_1 \gamma + a_2 \gamma^2, & Q_A(\gamma) &= a'_0 + a'_1 \gamma + a'_2 \gamma^2, \\
P_B(\gamma) &= b_0 + b_1 \gamma + b_2 \gamma^2, & Q_B(\gamma) &= b'_0 + b'_1 \gamma + b'_2 \gamma^2.
\end{aligned}$$

For the studied propeller and within the range of considered parameters, these coefficients have the following values:

$$\begin{aligned}
a_0 &= 0.836692, & a_1 &= 0.113536, & a_2 &= 0.079580, \\
a'_0 &= -0.002059, & a'_1 &= -0.000298, & a'_2 &= -0.001806, \\
b_0 &= 161.727490, & b_1 &= 60.400684, & b_2 &= -28.530729, \\
b'_0 &= -4.160263, & b'_1 &= 3.816861, & b'_2 &= 0.523051.
\end{aligned}$$

It is important to note that equation 3.19 holds for  $\psi_w < \psi_s$ , where  $\psi_s$  denotes the azimuthal position in the far wake region where vortex instability appears. Beyond  $\psi_w > \psi_s$ , the accuracy in determining the position of the tip vortices decreases rapidly. The azimuthal position  $\psi_s$  in the far wake has also been synthesized according to the following empirical law:

$$\psi_s = \frac{N_b \psi_b}{4} \left[ 8.5 - \frac{\alpha_0}{10} - \gamma(2 + \gamma) \right] + \psi_b. \quad (3.22)$$

Where,  $\psi_b = 360^\circ / N_b$ .

Figure 9 illustrates the evolution of wake contraction and the parameter  $\psi_s$  with respect to the wake azimuthal angle and the advance ratio for two different pitch angles.

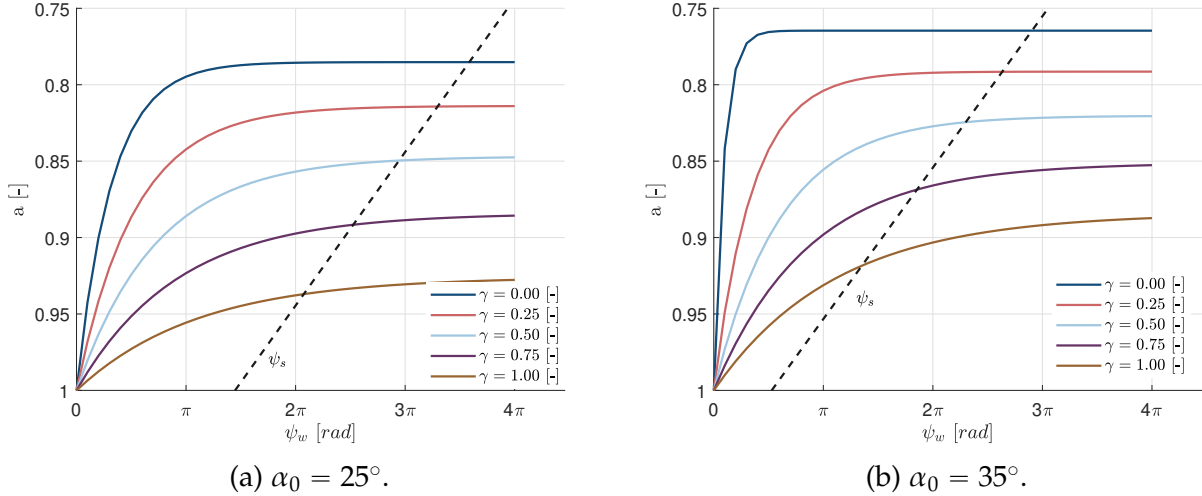


Figure 9: Evolution of the wake contraction and  $\psi_s$  parameter for  $N_b = 4$  with the wake azimuthal angle and the advance ratio for (a)  $\alpha_0 = 25^\circ$  and (b)  $\alpha_0 = 35^\circ$ .

Notably, the contraction no longer uniformly converges towards the previously observed value of 0.78. Instead, it exhibits greater sensitivity to both the pitch angle  $\alpha_0$  and the advance ratio  $\gamma$ . Specifically, these curves demonstrate a more pronounced radial contraction as  $\gamma$  decreases or  $\alpha_0$  increases, indicative of higher thrust conditions.

Furthermore, as  $\gamma$  decreases, distant wake instability becomes evident at larger azimuth angles. In addition, the contraction reaches its asymptotic value more swiftly with decreasing  $\gamma$ , suggesting that for small values of  $\gamma$ , vortex instability occurs when the contraction is nearly completed. Specifically, when  $\gamma$  approaches zero, the wake has already fully completed. Conversely, at higher  $\gamma$  values, instabilities manifest well before the wake achieves its final asymptotic contraction. It is therefore crucial to apply this empirical model with prudence in configurations involving high advance ratios and significant wake azimuthal angles.

It can now be considered how these empirical models of radial wake contraction should be applied to the different contraction models presented in Section 2.7. For the SST model, it is evident that the azimuthal angle will be obtained by taking the average velocity. For simplicity, this will be the velocity measured at the disk of the first rotor. The same applies to the thrust coefficient, it will be the thrust coefficient measured for the first rotor. Additionally, the angle  $\alpha_0$  will be taken at 75% of the chord, and the advance ratio will be that of the upper rotor. Once the wake contraction ratio  $a$  has been determined, the averaged axial velocity in the wake  $\overline{U_{P,w}}$  can be obtained by the conservation of mass flow, expressed as:

$$\overline{U_{P,w}} = \frac{\overline{U_{P,d}}}{a^2} \quad (3.23)$$

For the MST and SMST models, the application is less straightforward. It must be determined whether the wake contraction ratio should be measured separately for each annulus. This approach would involve considering the velocity at the disk at the level of each annulus, along with the previously mentioned parameters calculated at that specific radial position ( $C_T(y)$ ,  $\gamma(y) = V_c/\Omega y$ , and  $\alpha_0(y)$ ). It is essential to assess whether the empirical relationships for the wake contraction ratio will remain adequately representative of the actual physical behavior. Alternatively, the calculation can be performed by maintaining a constant contraction across the entire span, as in the SST model. The velocities for each tube would then be obtained by applying the conservation of mass at each annular level:

$$U_{P,w}(y) = \frac{U_{P,d}(y)}{a^2} \quad \text{or,} \quad U_{P,w}(y) = \frac{U_{P,d}(y)}{a(y)^2} \quad (3.24)$$

### 3.3 Torque cancelation

The cancellation of torque in coaxial counter-rotating rotors is crucial in drone design as it prevents undesired rotational motion of the drone's body. This inherent torque cancellation in counter-rotating systems results in enhanced stability and control, eliminating the need for constant adjustments by the control system. Energy efficiency is improved as power is

not diverted to counteract torque, allowing more power for lift and propulsion, extending flight time, and enabling precise maneuvers and hovering capabilities.

To achieve torque cancellation in coaxial counter-rotating rotors, two main strategies can be employed: adjusting either the collective pitch or the rotational speed of the lower rotor. By applying the secant method, either the collective pitch or the rotational speed of the lower rotor is fine-tuned to cancel out the torque from the upper rotor while the other parameter remains fixed. The secant method is an iterative numerical technique used to find the root of a function, in this case, the difference in torques between the two rotors. The process is as follows:

1. The function  $f(x) = Q_{\text{upper}} - Q_{\text{lower}}(x)$  is defined, where  $x$  is the variable parameter (either collective pitch or rotational speed).
2. Initial guesses are used to compute the values of the function. For the collective pitch strategy, the two starting points are respectively one degree under and over the collective pitch of the upper rotor. For the second strategy, the secant method starts with initial points 100 RPM under and over the upper rotor's speed.
3. The secant formula is applied to find the next approximation:

$$x_{n+1} = x_n - f(x_n) \frac{x_n - x_{n-1}}{f(x_n) - f(x_{n-1})} \quad (3.25)$$

4. The process is iterated until  $f(x_{n+1})$  is sufficiently close to zero, indicating that the torques are matched.

By carefully adjusting the chosen parameter (collective pitch or rotational speed) of the lower rotor using the secant method, the torque from the lower rotor can be matched to that of the upper rotor, achieving the desired torque cancellation and ensuring stable and efficient flight.

## 4 Model Validation

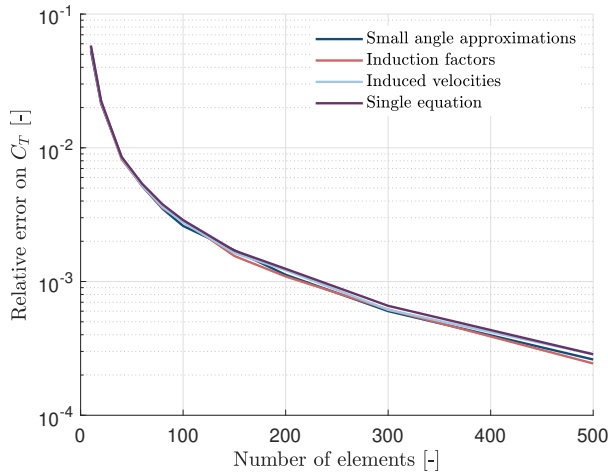
### 4.1 Single rotor

Before verifying the validity of the models for the coaxial rotor, it is crucial to first check the accuracy of the models for the single rotor. Indeed, if the model cannot accurately represent the simpler scenario where the rotor operates independently, it will not be capable of handling more complex cases involving interactions between rotors, such as in a coaxial rotor system.

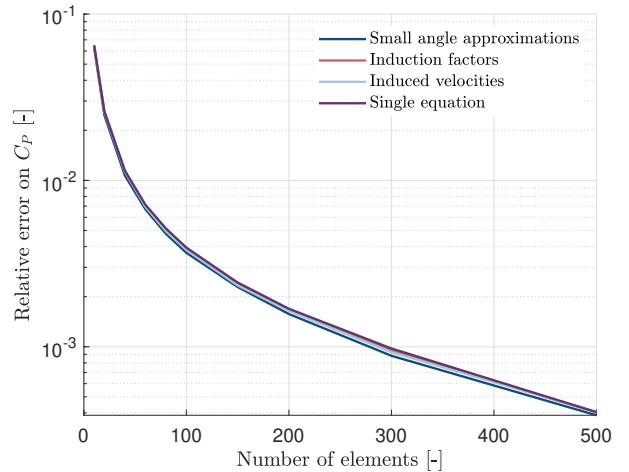
#### 4.1.1 Convergence with the number of elements

Before the validation of BEMT models for the single rotor configuration, it is essential to investigate the convergence of results as a function of the number of elements for each model. This step is crucial to identify an adequate number of elements that ensures a sufficiently converged solution, thereby facilitating a precise comparison of the models and enabling the validation of their accuracy.

In Figure 10, the relative error in performance is depicted as a function of the number of elements. This analysis is conducted on a thin electric APC 14x12 propeller as described in Tables A.1 and A.2. It is observed that the results converge uniformly across all models. Furthermore, Figure 11 illustrates the variation in computation time for a single operating point as a function of the number of elements. It is evident that the Leishman model, which employs linearized equations, exhibits the fastest computation time. Conversely, the Stahlhut model demonstrates significantly longer computation times, exceeding ten seconds per operating point when more than 500 blade elements are used.



(a) Thrust coefficient.



(b) Power coefficient.

Figure 10: Evolution of the relative error in performance as a function of the number of elements.

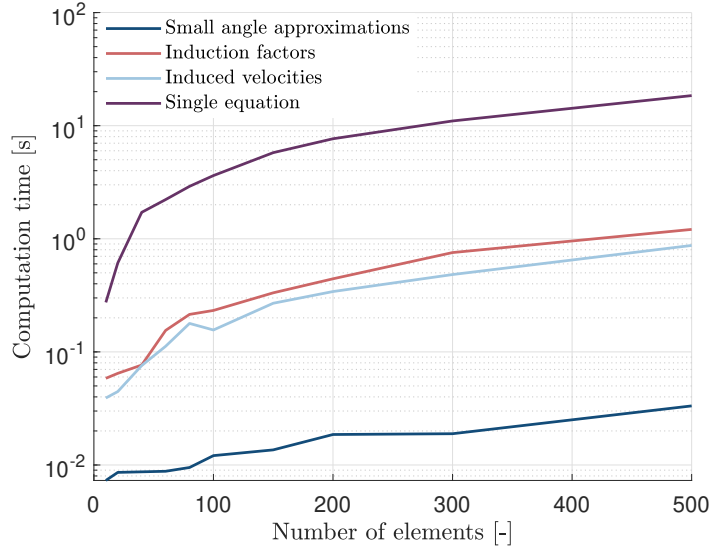


Figure 11: Evolution of the computation time as a function of the number of elements.

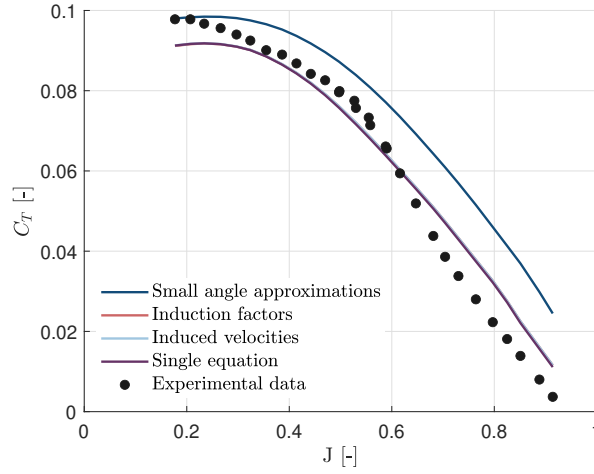
Based on these observations, a configuration with 100 blade elements is deemed to provide an optimal balance between accuracy and computational efficiency. The relative error is maintained below 0.3% for all models, and the computation time does not exceed 3 seconds per operating point, even for the most computationally demanding models.

#### 4.1.2 Comparison of the solvers

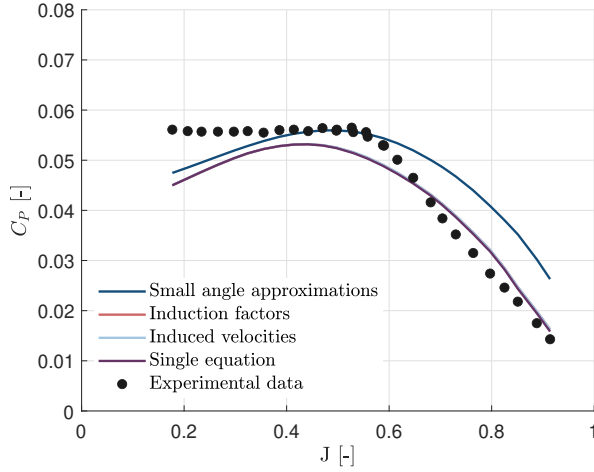
To verify the validity of the different models, the results will be compared with experimental data. A database of propellers for small UAVs will be used to accomplish this validation. This database corresponds to tests conducted at the University of Illinois at Urbana-Champaign (UIUC) [17]. Recognizing the lack of data on propellers suited for the growing number of UAVs, they carried out wind tunnel measurements for nearly 140 propellers typically used on small UAVs and model aircraft. These propellers, mostly in the 9- to 11-inch diameter range, were tested operating in the Reynolds number range of 50,000 to 100,000, typical for many UAVs. The measurements included data on thrust and torque coefficients over a range of advance ratios for specific RPMs. During these tests, the propeller speed (RPM) was kept constant while varying the wind tunnel speed to cover a range of advance ratios until reaching the windmill state (zero thrust). Additionally, measurements were taken in static conditions for a sweep over RPMs. To examine the effects of the Reynolds number, several different RPMs, ranging from 1,500 to 7,500 RPM depending on the propeller diameter, were tested for each propeller.

In Figure 12, the results from the Rotare's models are compared with the experimental data [17] for a thin electric APC 14x12 as described in Tables A.1 and A.3. In comparing the different models with the experimental data for thrust coefficient, power coefficient, and

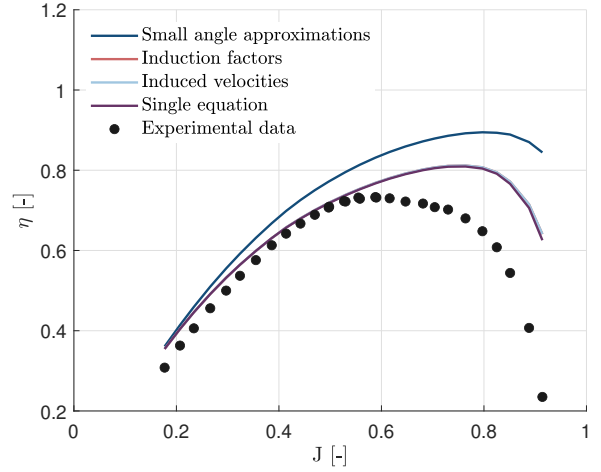




(a) Thrust coefficient.



(b) Power coefficient.



(c) Efficiency.

Figure 12: Comparison between the results obtained with the different models implemented in Rotare and experimental data [17] for the thin electric APC 14x12 propeller (cf. Tables A.1 and A.3).

efficiency, distinct trends and levels of accuracy are observed across the models. For the thrust coefficient, the small angle approximations model starts with a similar value at low  $J$  and drops less steeply, deviating significantly from the experimental data, especially at higher  $J$  values. In contrast, the induction factors, induced velocities, and single equation models, which are superimposed, provide a closer match to the experimental data. When examining the power coefficient, an increase to a peak around  $J \approx 0.4$  to  $0.6$  is indicated by the experimental data, followed by a decrease. A similar trend is predicted by all the solvers but they tend to increasingly underestimate the power coefficient as the axial velocity decreases. In addition, the small angle approximations model overestimates the power coefficient at higher  $J$  values. The induction factors, induced velocities, and single equation models offer

a more accurate fit to the experimental data, especially at higher  $J$  values, demonstrating improved predictive capability. For efficiency, an increase to a peak around  $J \approx 0.6$  is shown by the experimental data before declining. The small angle approximations model overestimates efficacy at low  $J$  and fails to align well with the experimental data at higher  $J$ . Conversely, the induction factors, induced velocities, and single equation models closely match the experimental data, particularly around the peak efficiency region. The overlap of the single equation model with the induction factors and induced velocities models suggests that very similar results are produced, accurately reflecting the experimental trends. The global enhanced accuracy of the small angle approximations model at lower axial speeds can be attributed to its assumption of small angles, which implies that the induced velocity is much less than the freestream velocity. Consequently, this model is particularly well-suited for applications such as hover or slow axial flow conditions.

Furthermore, it may be valuable for the results obtained with Rotare to be compared to those from other BEMT simulations found in the literature [18]. In Figure 13, Rotare's induction factor model is compared with an existing induction factor simulation for the thin electric APC 14x12 (cf. Tables A.1 and A.3). The results are found to be very similar, with small differences that could be attributed to the quality of the polars, as will be explained in section 4.1.4. This similarity is a good indication of the validity of the models.

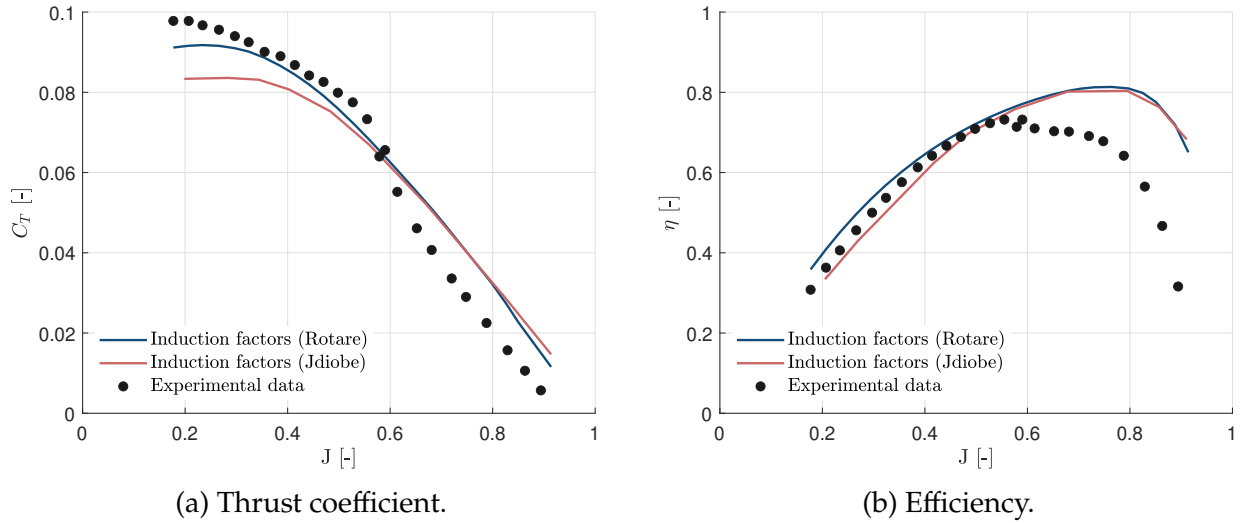


Figure 13: Comparison between the results obtained with the induction factor model implemented by Rotare and the results from an existing induction factor simulation (Jdiobe [18]) for the thin electric APC 14x12 propeller (cf. Tables A.1 and A.3).

Additionally, static conditions can be examined. Figure 14 compares the results from Rotare's models with experimental data [17] for the thin electric APC 14x12 propeller in hover. The operating conditions are now described in Tables A.1 and A.4. The solvers generally tend to underestimate the power coefficient across the entire RPM range. This trend is consistent with the observations in Figure 12, where decreasing axial velocity leads to an increased

underestimation of the power coefficient. For the thrust coefficient, the results show that Rotare's models closely match the experimental data, with the small angle approximation method providing the best fit. This consistency indicates that the solvers are generally reliable for predicting the thrust coefficient under static conditions.

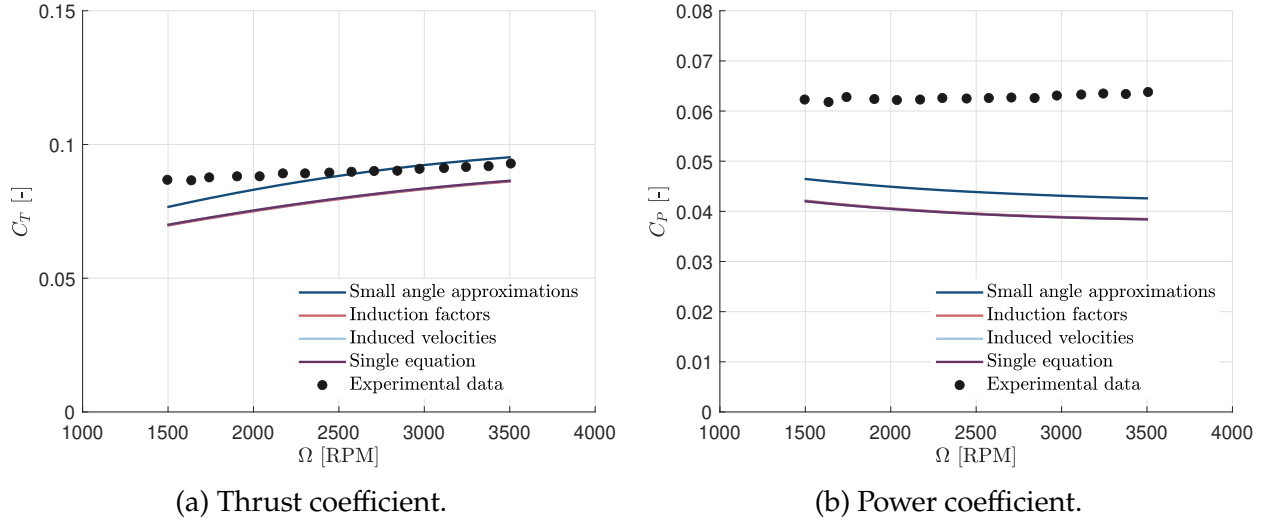
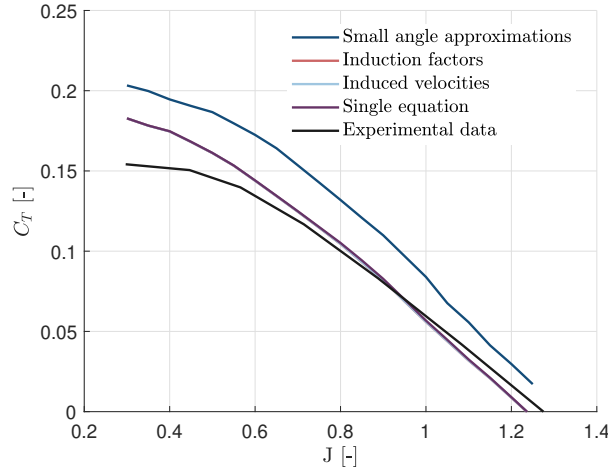


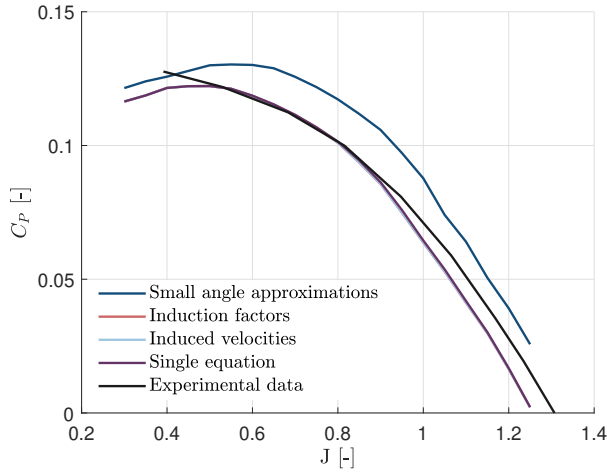
Figure 14: Comparison between the results obtained with the different models implemented in Rotare and experimental data [17] for the thin electric APC 14x12 propeller (cf. Tables A.1 and A.4).

To provide a comprehensive validation of the models under different conditions, another data set will be used. The experimental results obtained by Biermann et al. [19] will be reproduced. It should be noted that the focus is on the propeller designed with the Clark Y blade profile, referred to as 5868-9. The configuration of this propeller is described in Tables A.5 and A.6.

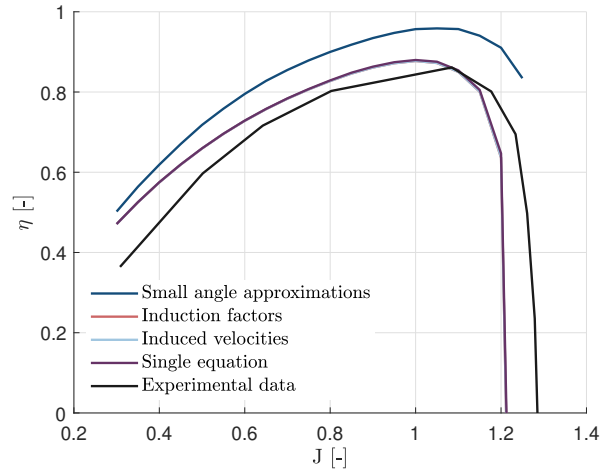
Figure 15 presents the comparison of the results from the different models with the experimental data from [19]. It can be seen that the small angle approximations model overestimates the thrust coefficient, particularly at smaller  $J$  values. On the other hand, the induction factors, induced velocities, and single equation models provide a closer match to the experimental. When examining the power coefficient, the small angle tends to overestimate a bit the power coefficient. The other models offer a more accurate fit to the experimental data, especially near the peak region. For efficiency, the experimental data show an increase to a peak around  $J \approx 0.6$  before declining. The small angle approximations model overestimates efficiency, while induction factors, induced velocities, and single equation models closely match the experimental data, particularly around the peak efficacy region. This trend parallels the findings in the APC 14x12 comparison, where the solvers also demonstrated better alignment with experimental data near the efficiency peak.



(a) Thrust coefficient.



(b) Power coefficient.



(c) Efficiency.

Figure 15: Comparison of the results from the Rotare's models with the experimental data [19] for the 5868-9 propeller (cf. Tables A.5 and A.6).

In conclusion, it has been observed that the Induction factors, Induced velocities, and Single equation models yield comparable results in both hover and axial flight. These results have been found to be in reasonable agreement with experimental data and other BEMT simulations conducted independently of this study. Additionally, it has been noted that these models generally exhibit a closer correlation with experimental data compared to the results produced by the Small angle approximation model.

An important aspect that has not yet been addressed is the convergence behavior of the iterative systems. It has been determined that the Induction factors and Induced velocities models do not consistently converge to a solution. Although the Single equation model enhances convergence, it is significantly more time-consuming (see Figure 11).

Given that the study will involve a coaxial rotor where torque cancellation is required, necessitating an additional iterative process (cf. section 3.3), computational time becomes a crucial parameter. Consequently, to ensure an accurate solution while maintaining manageable simulation times, the Induced velocities model will be employed in the subsequent phases of this study.

### 4.1.3 Stall analysis

It could be beneficial to vary the collective pitch angle as done in the experiment [19]. By doing so, the code's ability to represent stall can be observed, ensuring it is consistently aligned with both experimental data and the expected physical behavior.

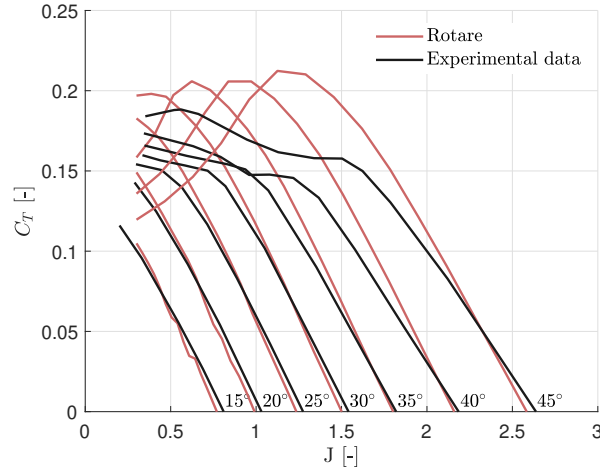
Figure 16 shows the evolution of the thrust coefficient, power coefficient, and efficiency with the blade angle (cf. Tables A.5 and A.7). Significant discrepancies are observed between the results from Rotare and the experimental data at higher collective pitches when the advance ratio is low. Specifically, in the experimental data, thrust exhibits a nearly continuous increase as the advance ratio decreases. In contrast, the BEMT simulation indicates a decrease in thrust beyond a certain threshold of the advance ratio, suggesting the onset of stall. Indeed, when the axial velocity is decreasing, the angle of attack is increasing. Therefore, if the lift is decreasing, it means that the stall point has been reached. It can also be observed that the power coefficient is decreasing, although the drag coefficient is supposed to increase with the angle of attack. Thus, it would be interesting to look at the distribution of the lift and the drag relative to the power to check if no errors have been introduced in the code.

Therefore, to investigate this further, the case where the collective pitch is equal to 45 degrees will be examined. Two advance ratios will be considered: the first one is where the thrust coefficient is maximal, and the second one is lower, where the thrust is decreasing, indicating the stall region. These advance ratios are respectively  $J = 1.2$  and  $J = 0.5$ . Figure 17 shows the distributions of the angle of attack, lift coefficient, and drag coefficient along the span for these advance ratios. It can be seen that when  $J = 0.5$ , the flow is detached over the entire span. Therefore, the idea that a stall occurs at this operating point is confirmed. It can be observed that the drag coefficient continues to increase while the lift coefficient has indeed decreased, except at the inner part of the radius, where even the detached flow produces more lift than when the flow was attached.

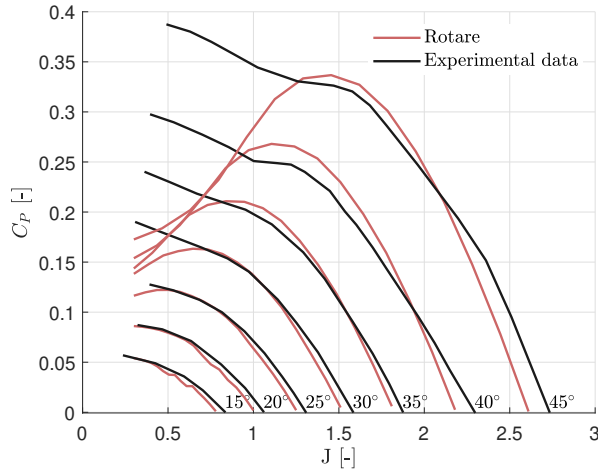
Given the significant increase in the drag coefficient, it raises the question of whether the observed decrease in the power coefficient is expected (cf. Figure 16). The power distribution is calculated based on equation 2.28 and can be decomposed into two components: induced power ( $dP_i$ ) and profile power ( $dP_p$ ), as expressed by:

$$dP_i = N_b \sin \phi dL \Omega y \quad \text{and} \quad dP_p = N_b \cos \phi dD \Omega y. \quad (4.1)$$

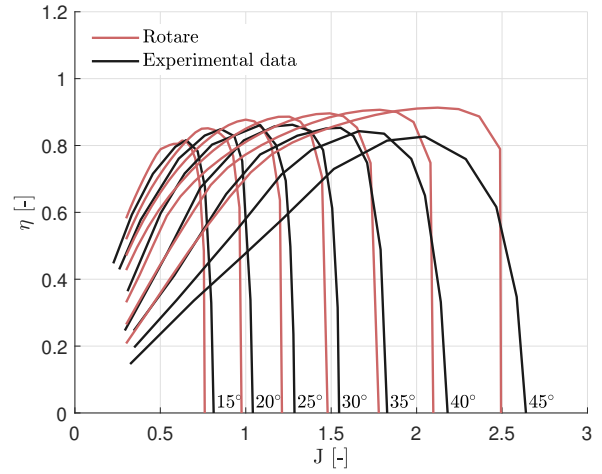
Figure 18 presents the distributions of profile power and induced power in the region of the power coefficient peak ( $J = 1.3$ ) and the stall region ( $J = 0.5$ ). It is evident that although



(a) Thrust coefficient.



(b) Power coefficient.



(c) Efficiency.

Figure 16: Comparison of the results from Rotare with the experimental data [19] for the 5868-9 propeller (cf. Tables A.5, A.7 and A.9).

profile drag increases significantly with the onset of stall, the predominant contribution is from induced drag. Consequently, as the lift force diminishes during the stall, the total power also decreases. This effect is further exacerbated by the reduction in the inflow angle during stall (cf. Figure 17a), resulting in a lift force that is less aligned with the tangential direction, thereby further reducing its contribution to the power.

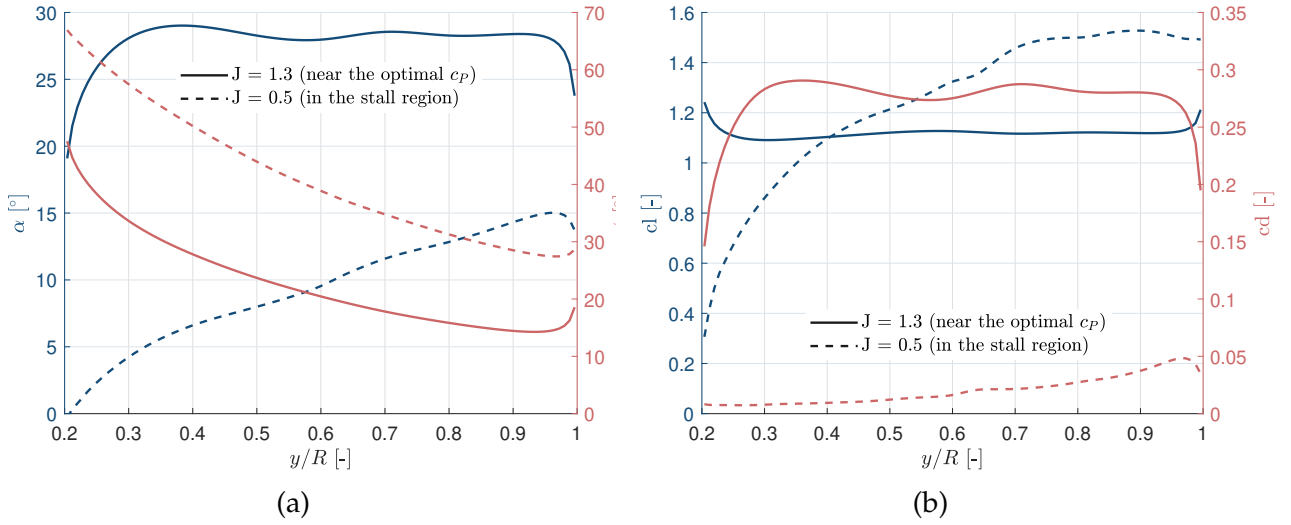


Figure 17: Distributions of (a) the angle of attack and inflow angle and (b) the lift and drag coefficients along the span for the 5868-9 propeller in the region of the power coefficient peak ( $J = 1.3$ ) and the stall region ( $J = 0.5$ ) (cf. Tables A.5 and A.9).

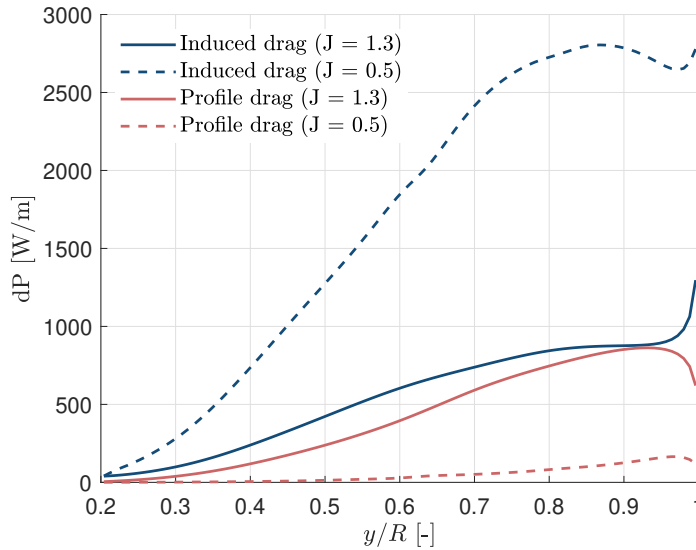


Figure 18: Distributions of profile power and induced power along the span for the 5868-9 propeller in the region of the power coefficient peak ( $J = 1.3$ ) and the stall region ( $J = 0.5$ ) (cf. Tables A.5 and A.9).

#### 4.1.4 Impact of the polars

The APC propellers predominantly use NACA 4412 airfoils. Therefore, this airfoil cross-section was assumed for each propeller segment in Rotare. For that, the 2-D aerodynamic input data has been generated using the XFOIL tool. However, for the 14-inch diameter pro-

propeller, the Reynolds numbers range from 14000 to 74000 for the propeller operating at 3500 RPM with an advance ratio varying from 0.2 to 0.9 (cf. Figure 19a) and range from 5000 to 65000 for the static conditions with the RPM varying from 1500 RPM to 3500 RPM (cf. Figure 19b). Consequently, for such low Reynolds numbers, the flow is dominated by viscous forces.

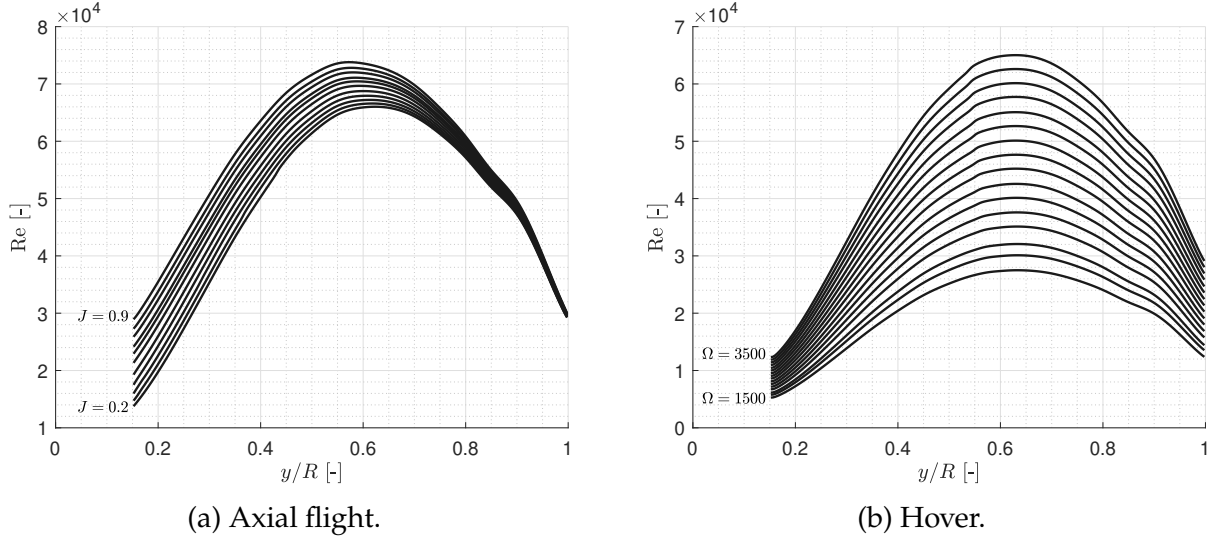


Figure 19: Reynolds number distribution for the thin electric APC 14x12 propeller (a) in axial flight (cf. Tables A.1 and A.3) and (b) in hover (cf. Tables A.1 and A.4).

Even though XFOIL is widely used for analyzing subsonic airfoils, it has limitations, especially at low Reynolds numbers. These arise from its simplified boundary layer and transition models, which are less effective at capturing complex flow behaviors, such as laminar separation bubbles and significant viscous effects.

Additionally, XFOIL assumes a smooth transition from laminar to turbulent flow. However, at low Reynolds numbers, this transition is highly sensitive to disturbances and surface roughness, leading to earlier and more abrupt transitions.

Moreover, at low Reynolds numbers, flow characteristics become more complex and prone to instability, especially near stall angles where flow separation occurs. XFOIL's iterative methods might struggle to converge under these conditions, leading to less reliable predictions. The laminar separation bubbles that form at low Reynolds numbers are challenging for XFOIL to model accurately, as they require detailed simulation of the viscous-inviscid interaction, which is beyond XFOIL's capabilities.

Comparative studies [20, 21] often show that XFOIL underpredicts the effects of laminar separation bubbles and fails to capture the full complexity of low Reynolds number flows. For accurate results, advanced CFD tools, which solve the Navier-Stokes equations with greater detail, are recommended. These tools provide more precise simulations by incor-



porating sophisticated models for turbulence and boundary layer interactions. Additionally, experimental methods like wind tunnel testing offer essential validation and insights that computational tools might miss.

However, certain modifications can be done in XFOIL software to be more accurate. First, the critical amplification factor ( $N_{crit}$ ), typically set around 9 for high Reynolds numbers, should be adjusted to lower values like 5 to better simulate these earlier transitions. This adjustment helps capture the onset of turbulence more accurately. The impact of the critical amplification factor is shown in Figures 20 and 21. It can be seen that the results are significantly improved for  $N_{crit} = 5$  compared to  $N_{crit} = 9$ . Additionally, increasing the number of panels can improve the resolution of the airfoil surface, leading to more accurate predictions of aerodynamic characteristics. By using a finer panel distribution, the detailed features of the flow, especially around critical areas such as the leading edge and separation points, can be better captured.

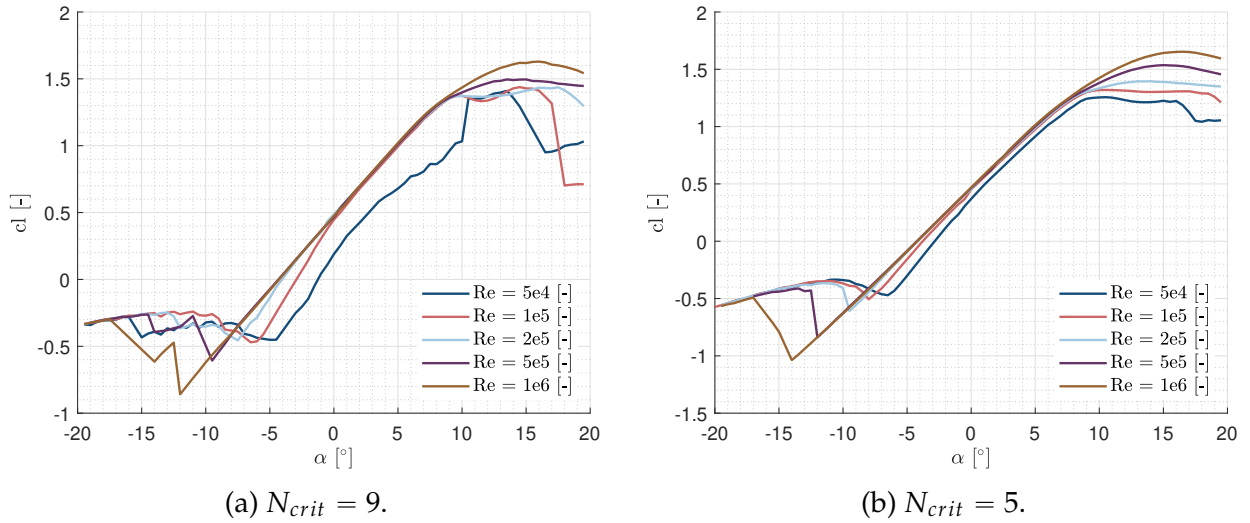


Figure 20: Lift coefficient from XFOIL for (a)  $N_{crit} = 9$  and for (b)  $N_{crit} = 5$  for a NACA 4412 airfoil.

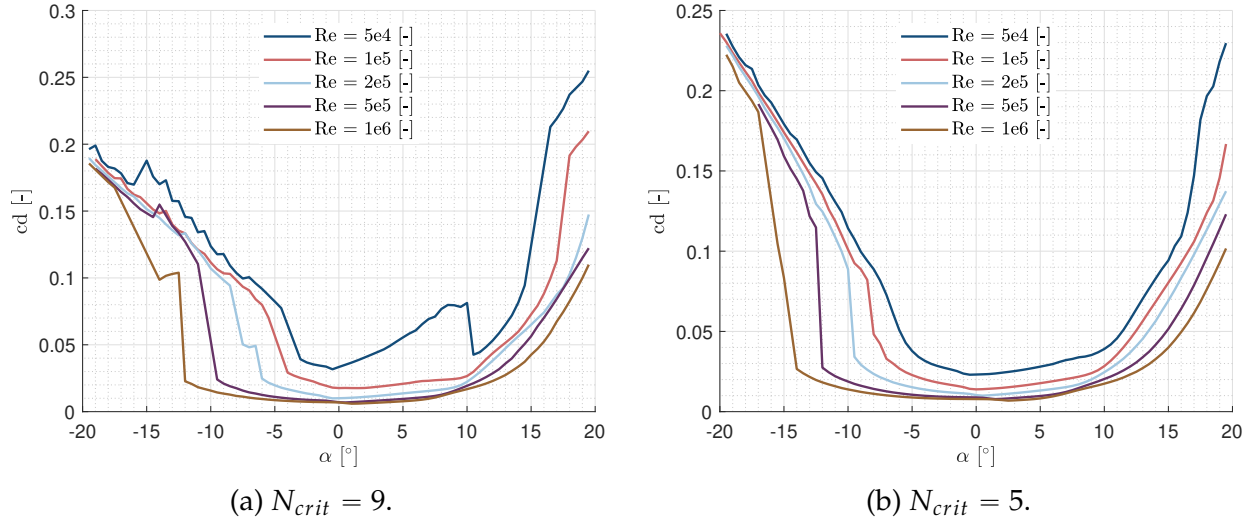


Figure 21: Drag coefficient from XFOIL for (a)  $N_{crit} = 9$  and for (b)  $N_{crit} = 5$  for a NACA 4412 airfoil.

Even by varying these parameters, the results remain inaccurate for Reynolds numbers below 50,000. This limitation is why such low Reynolds number effects have been disregarded.

## 4.2 Coaxial rotor

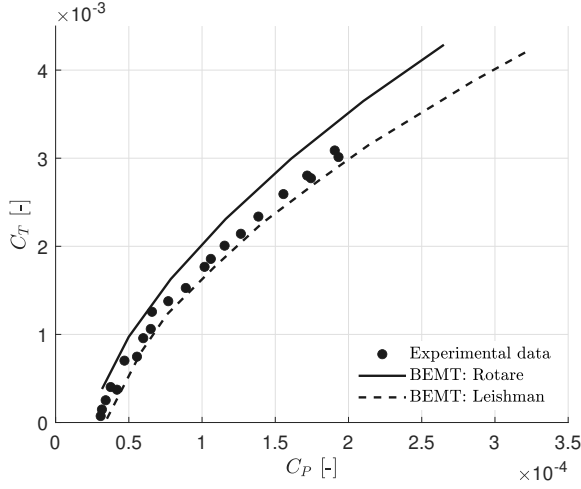
In the previous subsection, it was observed that the computational model produced accurate results for a single rotor configuration, demonstrating good agreement with experimental data. With the model validated for the single rotor case, the investigation can now be extended to the coaxial rotor configuration. This transition permits the assessment of the reliability of the various contraction models.

### 4.2.1 Overall assessment of predictive performance validity

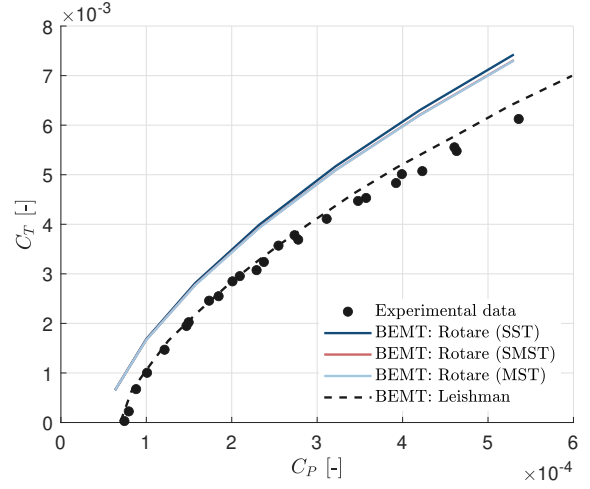
When considering contra-rotating coaxial rotors, the standard reference is the measurements taken by Harrington [22] using two sets of nominally full-scale rotors in hovering conditions. The geometries and technical information of these rotors are given in Tables A.10, A.11, A.12, and A.11.

Figures 22 and 23 compare Harrington's rotors results using the different coaxial models with the measurements made by Harrington [22]. Furthermore, it also compares these results with the BEMT results from Leishman [23, 24]. It is important to note that an upstream velocity  $U_{P,w} = V_c + v_i/a^2$  is used for the lower rotor in the studies from Leishman, which is contrary to what was determined in equations 3.23 and 3.24. This is considered incorrect since mass conservation is no longer guaranteed with this equation. However, this is not an issue in

this case because, for Harrington rotors, measurements are made in hover, so  $V_c = 0$  and the equations are equivalent.

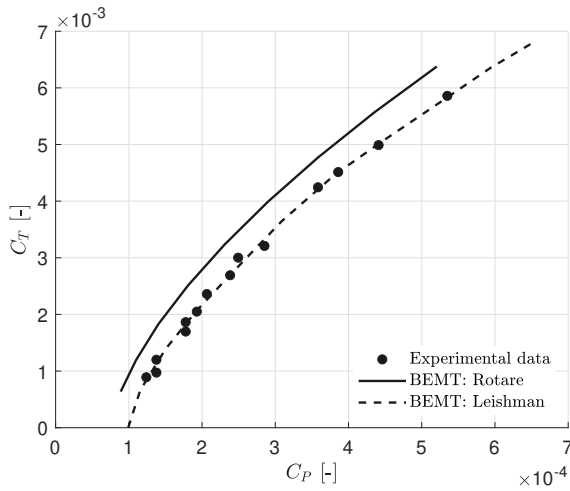


(a) Single rotor.

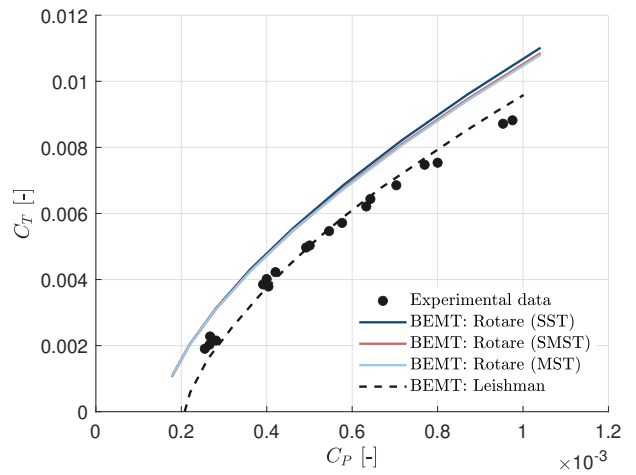


(b) Coaxial rotors.

Figure 22: Validation of the coaxial models from Rotare for (a) single and (b) coaxial rotors against measurements [22] and Leishman's BEMT [23, 24] of for Harrington Rotor 1 (cf. Tables A.10 and A.11).



(a) Single rotor.



(b) Coaxial rotors.

Figure 23: Validation of the coaxial models from Rotare for (a) single and (b) coaxial rotors against measurements [22] and Leishman's BEMT [23, 24] of for Harrington Rotor 2 (cf. Tables A.12 and A.13).

By examining the results, the first observation is that the coaxial models produce very similar results for both rotors. These results are also quite close to the measurements taken

by Harrington. However, the predictions consistently overestimate the thrust compared to the experimental results. This overestimation is also observed when considering the case of a single isolated rotor. One hypothesis for this discrepancy is that a portion of the measured thrust is lost due to the influence of the test stand. Specifically, the device measures the net change in total force. When the rotors generate a downward airflow, there is an upward force known as thrust. Concurrently, the air passing through the propeller induces a downward drag force. Thus, the net force change measured is the result of these two contributions. As a result, the experimentally determined thrust coefficient is expressed by:

$$C_T = \frac{T - D}{\rho A (\Omega R)^2}. \quad (4.2)$$

and is consequently lower than the value predicted by the blade element momentum theory (cf. section 2.5.2). Nonetheless, it remains inconsistent to see that Leishman's model aligns significantly better with the experimental results than the more precise models implemented in Rotare. In Figure 24 and 25, the different distributions of adimensional thrust coefficient and adimensional torque are compared between Leishman's and Rotare's simulation on both the upper and the lower rotor. For this comparison, the Harrington rotor 1 was used with a net system cT of 0.004 (cf. Table A.15).

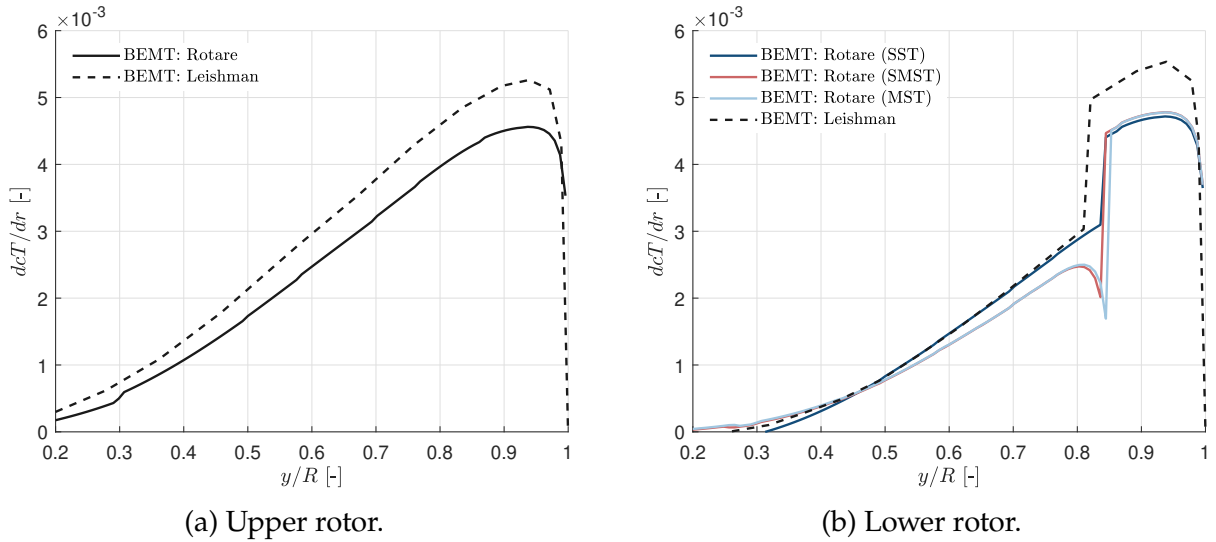


Figure 24: Distribution of the adimensional thrust coefficient on (a) the upper and (b) the lower rotor for Harrington Rotor 1, with Rotare (cf. Tables A.10 and A.15) and Leishman's simulation [23, 24].

It can be observed that even though the net system cT is 0.004 in each simulation, the nondimensional thrust distributions obtained by Leishman seem to be slightly higher for both the upper and lower rotors. This observation supports the idea that a correction might have been applied by Leishman to account for the thrust on the nacelle, although this correction is never explicitly mentioned. This hypothesis is further supported by the fact that, for the

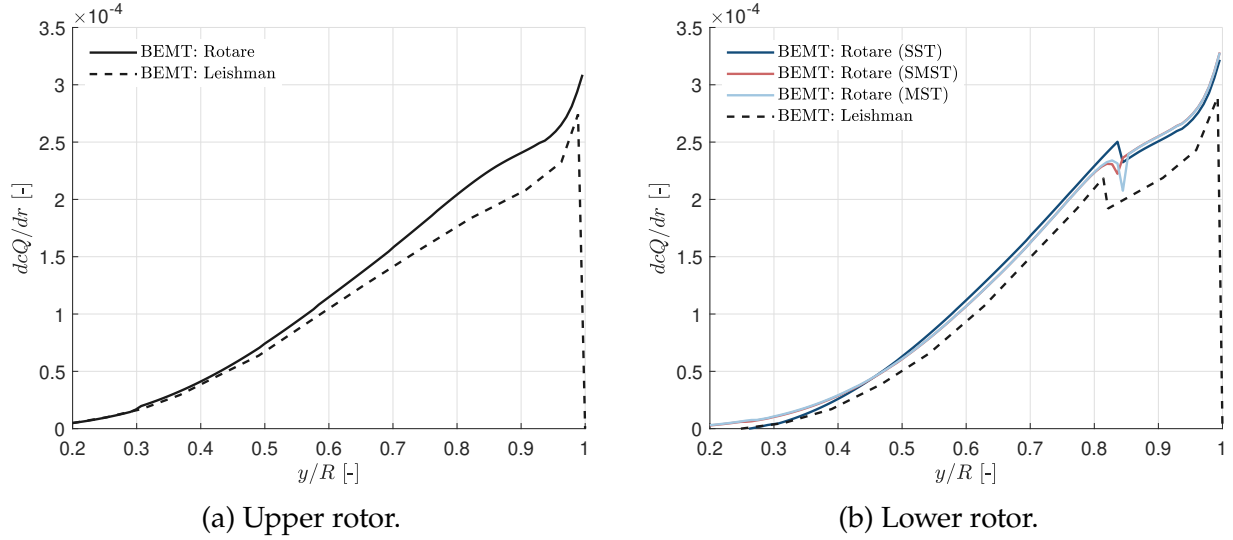
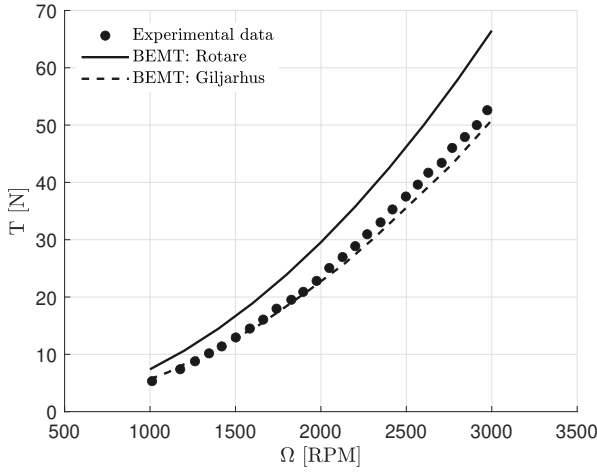


Figure 25: Distribution of the adimensional torque coefficient on (a) the upper and (b) the lower rotor for Harrington Rotor 1, with Rotare (cf. Tables A.10 and A.15) and Leishman’s simulation [23, 24].

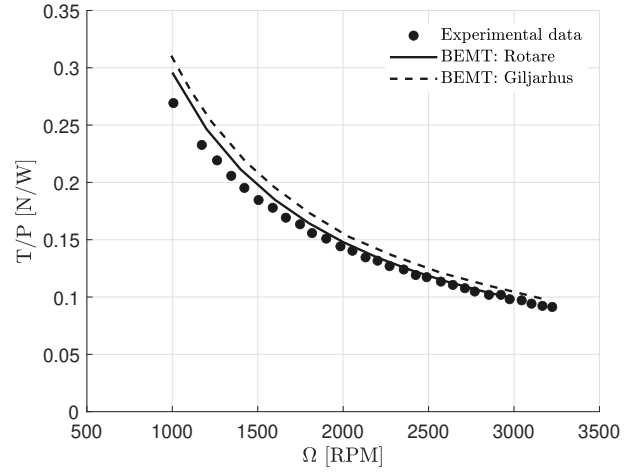
same net system thrust ( $cT = 0.004$ ), Leishman underestimates the torque compared to the models in ROTARE for both the upper and lower rotors. This is contrary to the observations made in Figure 22.

It would be valuable to compare and verify the validity of the models on another design and under different operating conditions. Additionally, in the following set of data, the thrust and efficiency values are provided separately for each rotor, allowing for a detailed comparison of these values on each rotor. For this dataset, the geometry is based on the commercial T-MOTOR G28x9.2 carbon fiber rotor, whose geometry and operating conditions are given in Tables A.16 and A.17. To maintain consistency, the rotor geometry is modeled using a single airfoil instead of the actual airfoil shape from the commercial rotor. The chosen airfoil is the Archer A18, originally designed for free-flight airplanes. Although there are some discrepancies, particularly towards the trailing edge, the overall agreement with the expected geometry is good.

First, the results obtained for a single isolated rotor will be examined. In Figure 26, a comparison is shown of the computed thrust and efficiency using BEMT from ROTARE against the experimental values for varying angular velocities. The results are also compared with another BEMT model from Giljarhus [25]. It can be observed that, despite the thrust being quite overestimated, especially at high rotation speeds, the efficiency is in good agreement with the experimental data. It is important to note that the BEMT model from [25] uses, for the sake of simplicity, a constant Reynolds number of  $Re = 175,000$ , which is approximately the Reynolds number at  $r = 0.75R$  at a rotational speed of 2000 RPM. This simplification could explain some of the discrepancies between the two BEMT simulations.



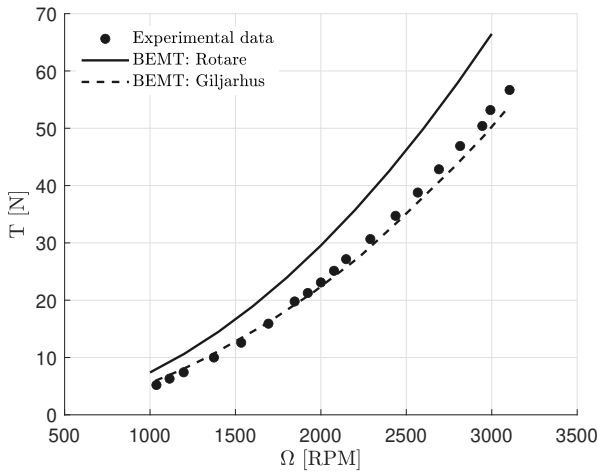
(a) Thrust



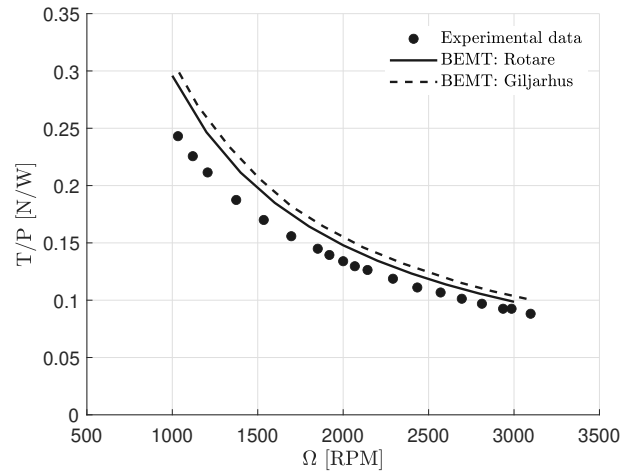
(b) Efficiency

Figure 26: Comparison between the results obtained with the coaxial models implemented by Rotare, the experimental data [25], and the results from Giljarhus's BEMT simulation [25] for T-MOTOR G28x9.2 carbon fiber single rotor (cf. Tables A.16 and A.17).

The same analysis can now be applied to a coaxial rotor system. The rotors are positioned 0.115 meters apart, rotating in opposite directions at the same angular velocity. It is important to note that for this configuration, the overall system torque is not balanced. Figures 27 and 28 present a comparison of the efficiencies and thrusts for each rotor individually.



(a) Thrust



(b) Efficiency

Figure 27: Comparison between the results obtained with the coaxial models implemented by Rotare, the experimental data [25], and the results from Giljarhus's BEMT simulation [25] for T-MOTOR G28x9.2 carbon fiber upper rotor (cf. Tables A.16 and A.17).

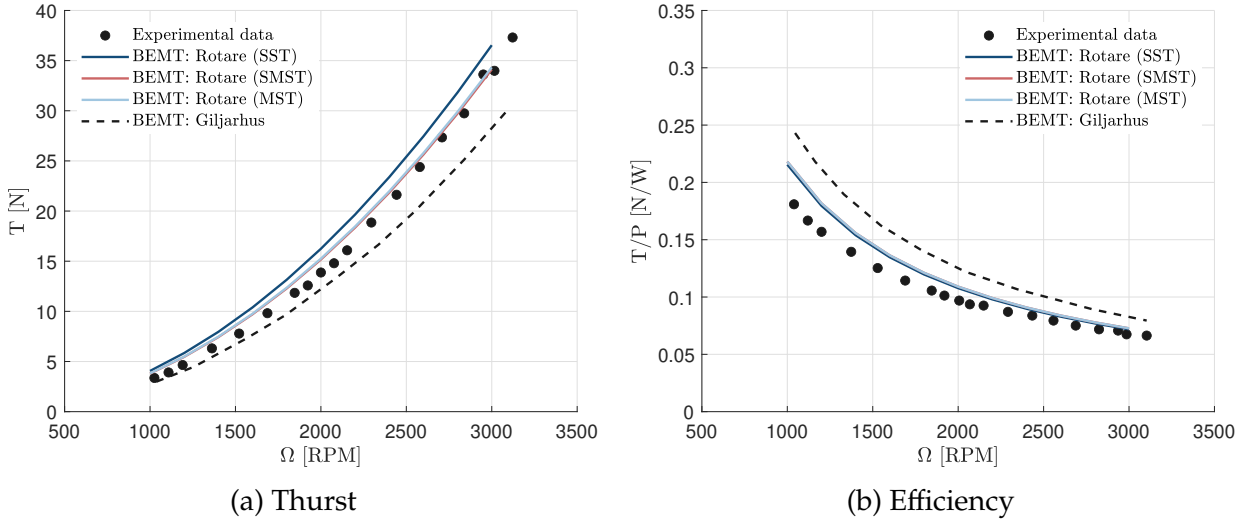


Figure 28: Comparison between the results obtained with the coaxial models implemented by Rotare, the experimental data [25], and the results from Giljarhus's BEMT simulation [25] for T-MOTOR G28x9.2 carbon fiber lower rotor (cf. Tables A.16 and A.17).

An initial observation indicates that the experimental results for the upper rotor are nearly identical to those of the isolated rotor. This suggests that the upper rotor is minimally affected by the lower rotor, thus substantiating the assumption that the upper rotor operates independently. Consequently, the efficiencies for the upper rotor are always in good agreement with the experimental data.

For the lower rotor, it is observed that both the thrust and efficiency decrease significantly. This reduction is more pronounced in the results obtained from the BEMT from Rotare, thereby reducing the discrepancy between the BEMT simulation outcomes and the experimental data. Furthermore, it is noted that multiple stream tubes models yield lower thrust compared to the single stream tube model. Nevertheless, the difference in efficiency among the models is considerably less pronounced.

#### 4.2.2 Impact of the incorporation of tangential velocity induced by the upper rotor on the lower rotor.

In this section, the impact of incorporating tangential velocity upstream of the lower rotor, as introduced in Section 3.1, will be analyzed. Figure 29 illustrates the effect of this addition on the performance of the T-MOTOR G28x9.2 carbon fiber lower rotor. This figure allows for the visualization of the impact on each of the coaxial models.

The initial observation indicates that no difference is observed for the SST model. This can be attributed to the model's assumption of a constant axial velocity upstream of the lower

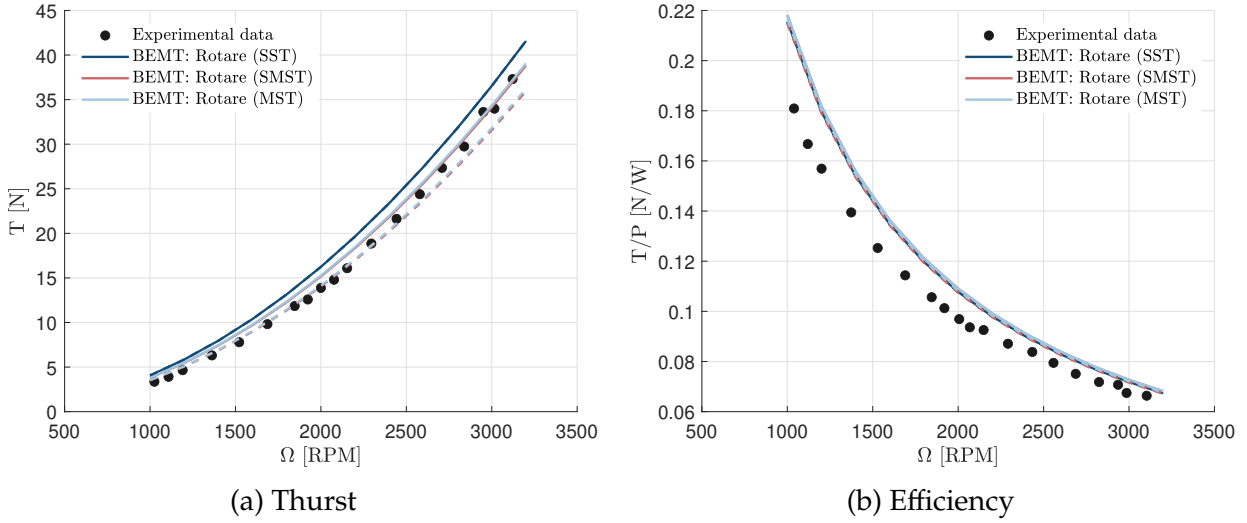


Figure 29: Comparison between the results obtained with (in full line) and without (in dot line) the incorporation of tangential velocity induced by the upper rotor on the lower rotor, for the performance of the T-MOTOR G28x9.2 carbon fiber lower rotor (cf. Tables A.16 and A.17).

rotor while neglecting the wake swirl velocity.

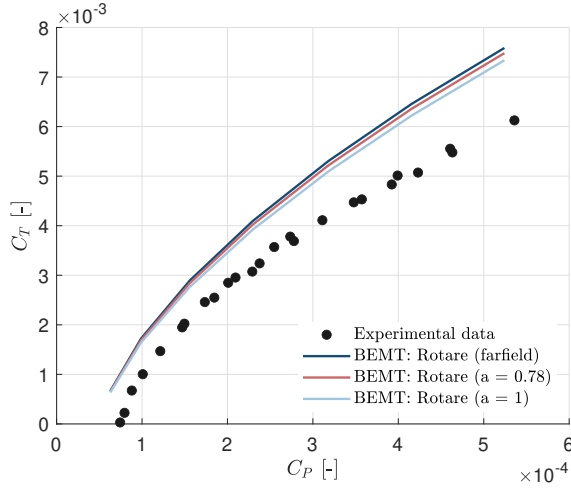
Additionally, it is observed that the efficiency of the lower rotor remains practically unaffected by this addition for the other models as well. Conversely, a significant impact on thrust generation is noted for both the MST and SMST models. As explained in Section 3.1, in a counter-rotating coaxial rotor system, the upstream tangential velocity positively contributes to and enhances the rotational velocity of the second rotor. This results in an increase in thrust due to the incorporation of this tangential velocity. Furthermore, it is observed that the magnitude of this increase is proportional to the rotational speed, a logical conclusion given that higher rotational speeds result in a greater tangential induced velocity in the upper rotor, thereby amplifying the effect on the lower rotor.

#### 4.2.3 Impact of the wake contraction

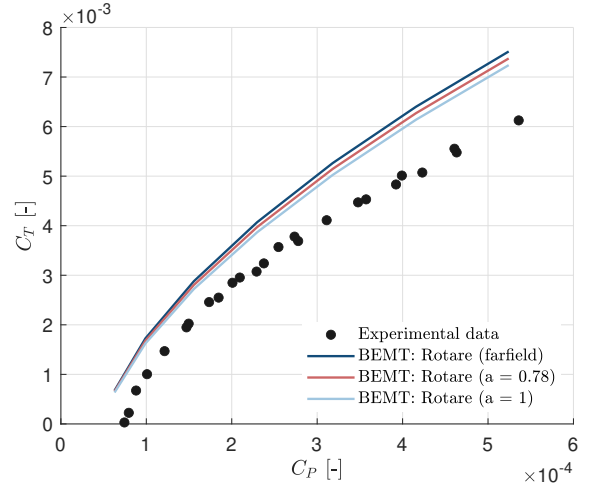
To determine the impact of wake contraction, the results for the first Harrington rotor will be compared for the far-field scenario where the lower rotor is positioned within the fully developed wake of the upper rotor and for the boundary limits of wake contraction ratios derived from the empirical case, as shown in Figure 30.

Although the discrepancy between the results obtained for the different wake contractions does not seem very significant, it is nevertheless more important than that obtained between the different contraction models (see Figure 22b). It would therefore be inconsistent to disregard this factor in the calculations. Furthermore, the difference is solely due to the con-





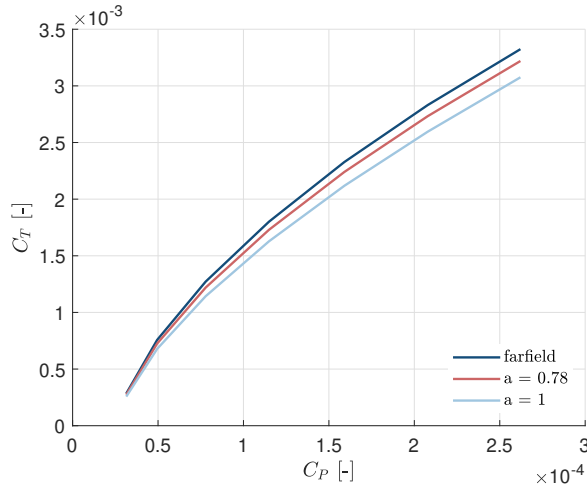
(a) Single stream tube model (SST).



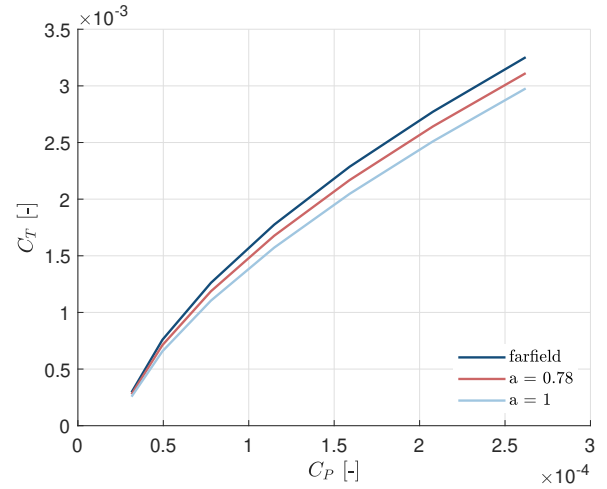
(b) Multiple stream tubes model (MST).

Figure 30: Comparison between the results for the first Harrington rotor with the far-field scenario and extreme wake contraction ratios from the empirical case (cf. Tables A.10 and A.11).

tribution of the lower rotor. To better compare the discrepancies arising from the differences in contraction, the performances are compared solely on the lower rotor in Figure 31. It is evident that the contraction taken into account will have a significant impact on the lower rotor's performance. This impact will affect the overall system performance, especially as the contribution of the lower rotor increases.



(a) Single stream tube model (SST).



(b) Multiple stream tubes model (MST).

Figure 31: Comparison between the results for the first Harrington rotor with the far-field scenario and extreme wake contraction ratios from the empirical case for the lower rotor (cf. Tables A.10 and A.11).

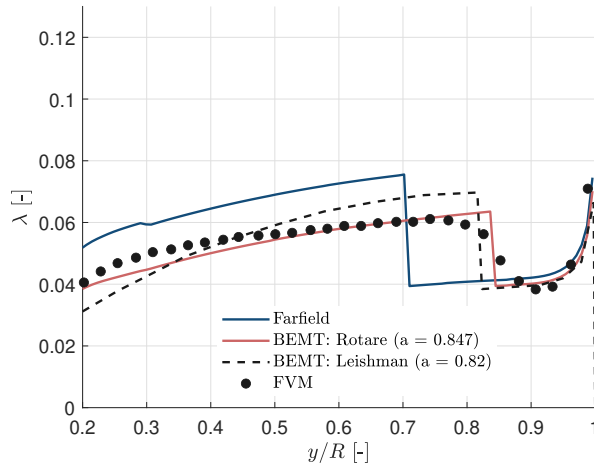
Now that the impact of wake contraction on the results is known, it is important to verify if the contraction obtained through empirical models is valid. For this purpose, the nondimensional inflow distribution for different models will be compared using the contraction predicted by the empirical model, the far-field case, and contrasted with Leishman's distribution. Note that, for the multiple stream tube models, both approaches presented in section 3.2 are compared: one that averages the data to obtain a constant wake contraction ratio  $a$  across the span, and another that uses the distributions of velocity and thrust coefficient to derive a wake contraction ratio distribution  $a(y)$ . Additionally, these comparisons will be extended to include results obtained from the Finite Volume Method (FVM), which is expected to provide higher accuracy due to the enhanced fidelity of computational fluid dynamics simulations. The FVM offers a more detailed representation of the flow field by solving the Navier-Stokes equations directly, thereby capturing complex interactions and variations in the flow that may not be accounted for by simpler methods such as Blade Element Momentum Theory (BEMT). Figure 32 shows these comparative results.

It can be observed that the inner part of the lower rotor, which is impacted by the upper rotor, is generally well-modeled with the empirical model. Specifically, it closely matches the distributions obtained by Leishman's method and the Free Vortex Method, much better than when the far-field approximation was applied. For the SST model, it is noted that the distribution aligns quite well with the FVM. However, for the MST model, the distribution deviates from the FVM distribution. Instead, it closely matches the distribution obtained by Leishman but diverges towards the outer region impacted by the upper rotor. It is also noted that for this model, using a constant contraction or a distribution of contraction yields similar results. In contrast, for the SMST model, this is no longer the case. Using a variable contraction along the span leads to results that further diverge from the distributions derived from Leishman or the FVM.

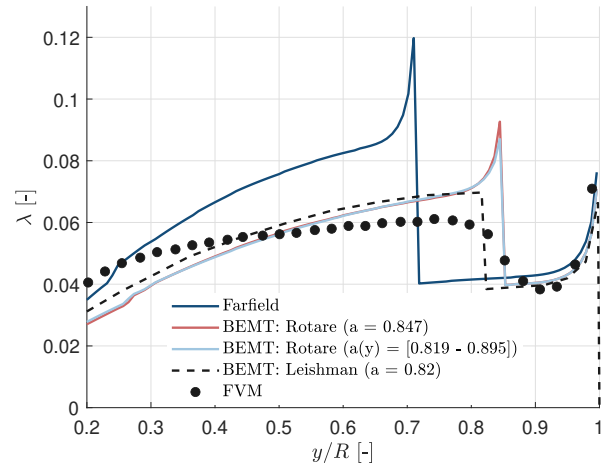
The impact of wake contraction can also be observed in the case of the T-Motor. Figure 33 compares the results for the lower rotor in the far-field scenario, where the lower rotor is positioned within the fully developed wake of the upper rotor, with the boundary limits of wake contraction ratios derived from the empirical case, alongside the experimental data.

It can be observed that under the far-field assumption, there is a significant deviation from the experimental results. Specifically, both thrust and efficiency are overestimated compared to the empirical contraction. This discrepancy is expected, as the far-field assumption further limits the area of the lower rotor within the vena contracta of the upper rotor, a region where the thrust and the efficiency are reduced compared to the scenario in which it operates in isolation.

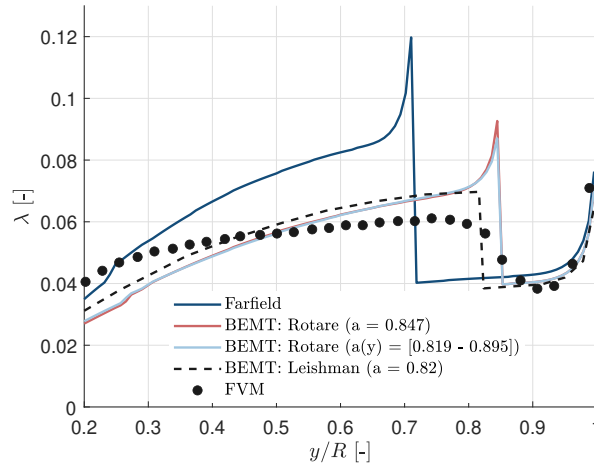
Thus, utilizing the empirical model once again demonstrates an improvement in the results. It remains essential to question whether the contraction derived from the empirical model accurately represents reality. To this end, the upstream velocity distribution at the second rotor, obtained for a rotational speed of 1600 RPM, using the empirical model, will be compared with higher-fidelity data, specifically results from computational fluid dynamics



(a) Single stream tube model (SST).



(b) Multiple stream tubes model (MST).



(c) Simplified multiple stream tubes model (SMST).

Figure 32: Comparison between the inflow distributions obtained from Rotare using the empirical Method, Leishman's BEMT, and the finite volume method (FVM) (cf. Tables A.10 and A.15).

(CFD)[25]. Additionally, these distributions will be compared to the far-field case and the distribution derived from Giljarhus' BEMT model. These comparisons are conducted for each coaxial model, as illustrated in Figure 34.

The initial observation is that the distributions obtained using the empirical model exhibit a closer alignment with those from CFD compared to the far-field assumption. Specifically, the contracted wake area is larger and more accurately reflects reality. Furthermore, the axial upstream velocity is lower across the entire span, aligning more closely with the CFD results. In the SST model, the velocity is observed to be averaged within the wake, showing a good

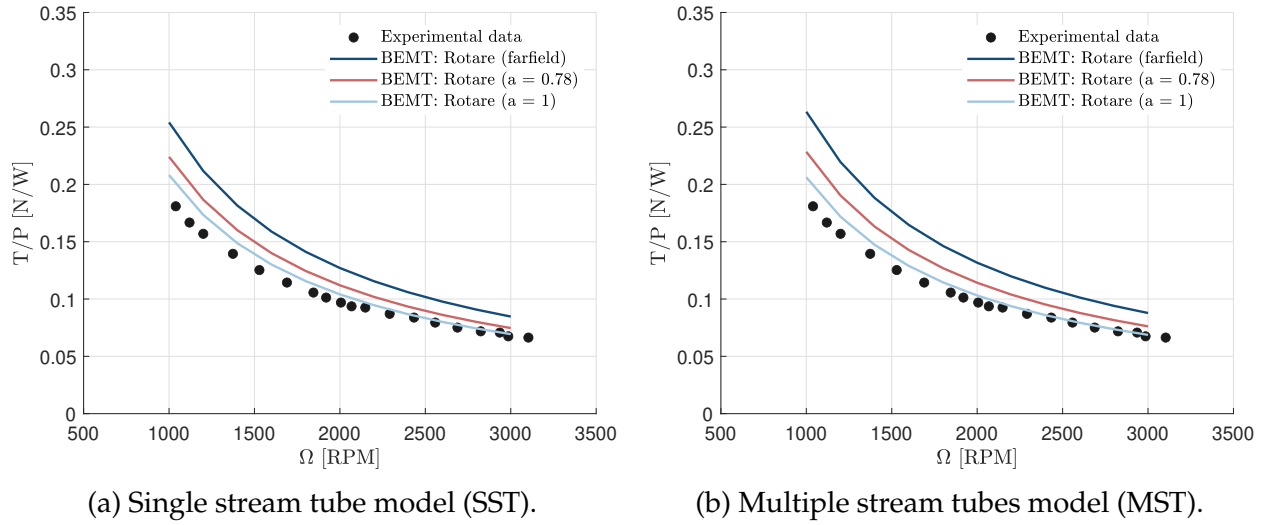
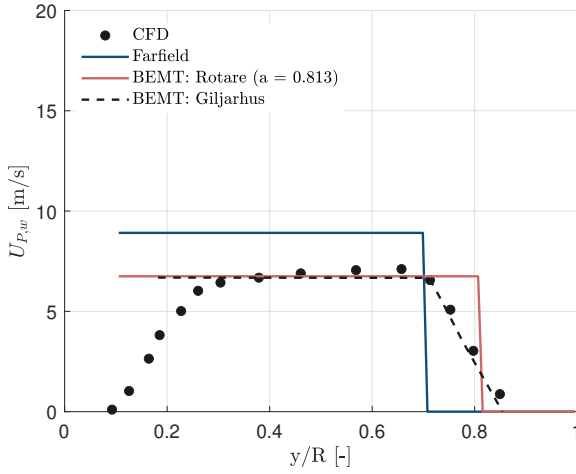


Figure 33: Comparison between the results for the T-MOTOR G28x9.2 carbon fiber lower rotor with the far-field scenario and extreme wake contraction ratios from the empirical case (cf. Tables A.16 and A.17).

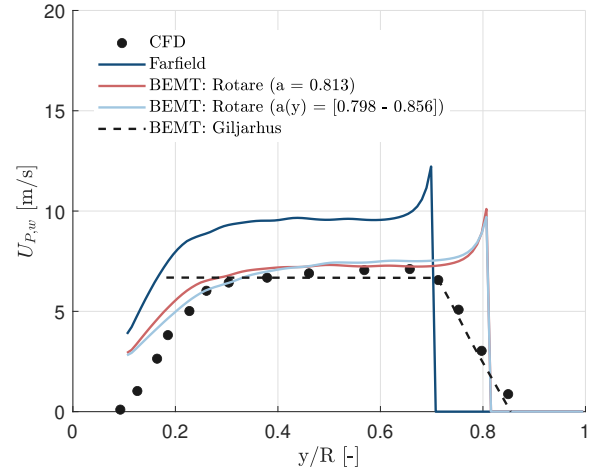
match at the wake's center but deviating near the hub and the wake's extremities. For the SMST and MST models, the velocity distribution within the wake aligns more closely with the CFD data. However, at the wake's extremities, the models predict an increase in velocity, whereas the CFD data indicate the opposite. Additionally, it is observed that consistent with previous findings for Harrington's rotor, whether the radial contraction is variable or constant has minimal influence on the MST model's results but significantly impacts the SMST model's results. One final observation is that the transition of upstream velocity on the lower rotor, between the section within the vena contracta of the upper rotor and the clean region outside the vena contracta, is very abrupt in each coaxial model. Computational fluid dynamic analysis indicates that this transition is significantly smoother in reality.

Similarly, the tangential velocity distribution along the span of this rotor under identical conditions can be analyzed. The upstream tangential velocity is consistently disregarded in the SST model and is therefore represented in Figure 35 exclusively for the MST and SMST models.

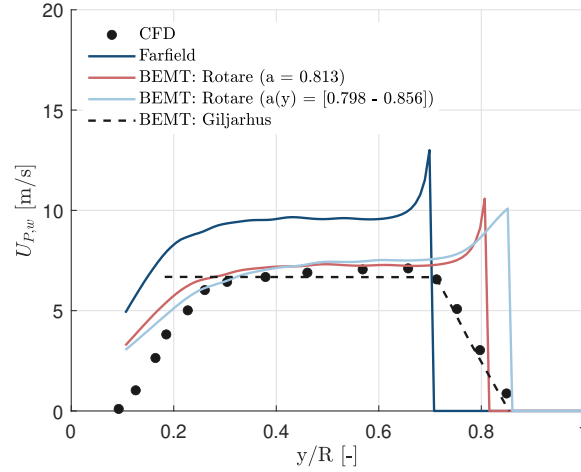
A peak is observed near the hub, with this peak being more significant when the far-field assumption is applied. Subsequently, the upstream tangential velocity increases until it becomes zero in the region unaffected by the upper rotor. In the empirical models, the higher wake contraction ratio results in a non-zero tangential velocity over a larger portion of the span. Moreover, this tangential velocity is greater throughout the outer region of the wake compared to the far-field scenario. It is also noted that the distributions for the SMST and MST models are almost identical.



(a) Single stream tube model (SST).



(b) Multiple stream tubes model (MST).



(c) Simplified multiple stream tubes model (SMST).

Figure 34: Comparison between the upstream axial velocity distributions obtained from Rotare using the empirical Method and far-field assumption with Giljarhus's BEMT [25], and the computational fluid dynamics (CFD) [25] (cf. Tables A.16 and A.18).

When the case of advancing propellers is considered, it becomes challenging to obtain high-fidelity data for validating the performance predictions of coaxial models. Additionally, determining the validity and applicable conditions of the empirical model described by Favier [15] presents significant difficulties. Therefore, it is proposed that, in a future study, wind tunnel tests be conducted on specific coaxial systems to validate the performance predictions of the different coaxial models in the context of advancing propellers. Furthermore, similar to the hover case, a CFD analysis could be performed on the coaxial system to determine the inflow ratio distribution over the span or other relevant parameters. This analysis would aid in validating the empirical wake contraction ratio model as described by Favier

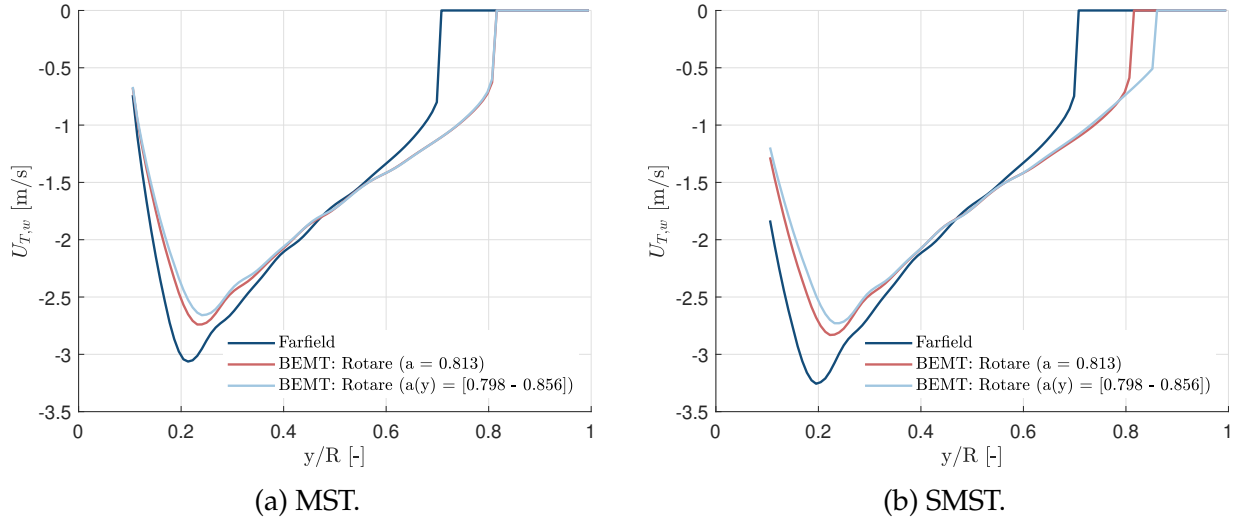


Figure 35: Comparison between the upstream tangential velocity distributions obtained from Rotare using the empirical Method and far-field assumption with Giljarhus's BEMT [25], and the computational fluid dynamics (CFD) [25] (cf. Tables A.16 and A.18).

for each of the coaxial models.

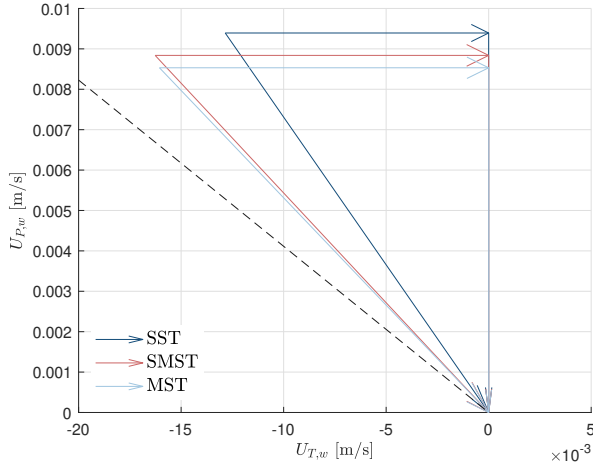
#### 4.2.4 Comparison of the coaxial models

In the preceding sections, it has been observed that comparing different models based on the overall assessment of performance validity is rather challenging. While similarities were noted in the results across models, distinctions became clearer when velocity or inflow ratio distributions along the span were analyzed. These distributions indicated that reality was more accurately represented by multi-tube models, particularly in the central wake region near the hub.

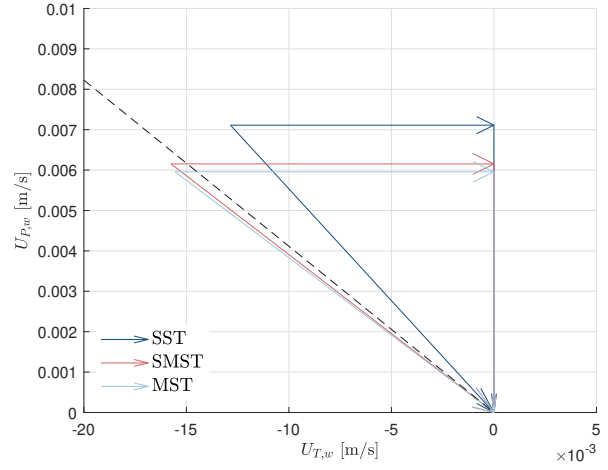
Additionally, the velocity triangles for each of the coaxial models can also be compared. This analysis is performed for the velocities upstream of the T-MOTOR G28x9.2 carbon fiber lower rotor. Figures 36 and 37 show these velocity triangles at 20 and 65 percent span, respectively. Note that the extension of the chord is also illustrated, along with the angle relative to the normal, which corresponds precisely to the pitch angle at the respective blade section.

Initially, it is generally observed that far-field contraction ( $a = 0.707$ ) results in higher axial velocities and tangential velocities comparable to those predicted by the empirical contraction model ( $a = 0.813$ ). Consequently, the inflow ratios are systematically lower with the far-field assumption.

Subsequently, for the velocity triangles at 20% span, it is noted that the coaxial models predict a higher tangential velocity and a lower axial velocity relative to the single stream tube

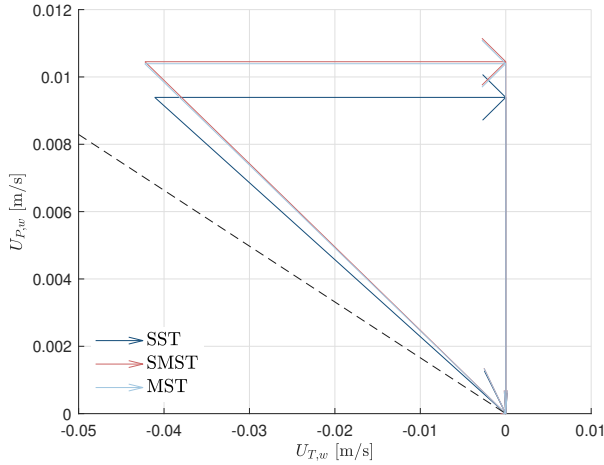


(a) Farfield wake contraction.

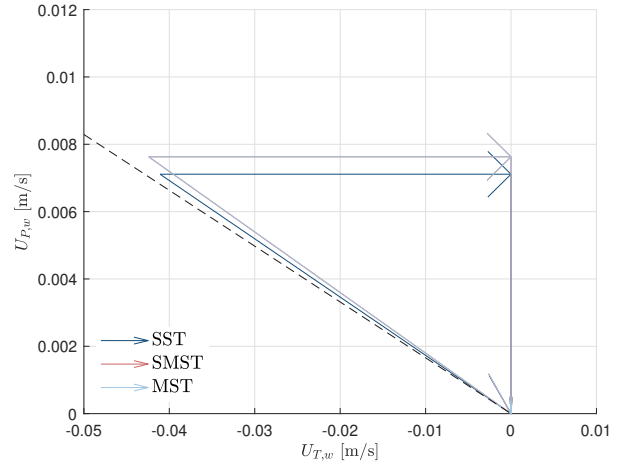


(b) Empirical wake contraction

Figure 36: Comparison of the velocity triangles upstream of the T-MOTOR G28x9.2 carbon fiber lower rotor (cf. Tables A.16 and A.18) at 20% span for each of the coaxial models.



(a) Farfield wake contraction.



(b) Empirical wake contraction

Figure 37: Comparison of the velocity triangles upstream of the T-MOTOR G28x9.2 carbon fiber lower rotor (cf. Tables A.16 and A.18) at 65% span for each of the coaxial models.

model, resulting in a substantially larger inflow angle. At 65% span, the tangential velocity remains slightly elevated with the multiple stream tube models, but the axial velocity also increases, resulting in a smaller inflow angle compared to the SST model. Additionally, it is observed that at 65% span, the angle of attack is consistently negative. At a 20% span, the angle of attack is also negative for the SST model and for the SMST and MST models under the far-field assumption.

Therefore, it is pertinent to verify that for these blade sections, the forces are directed downward and that the resultant thrust is negative in these scenarios. The thrust distributions along the span for each model are depicted in Figure 38.

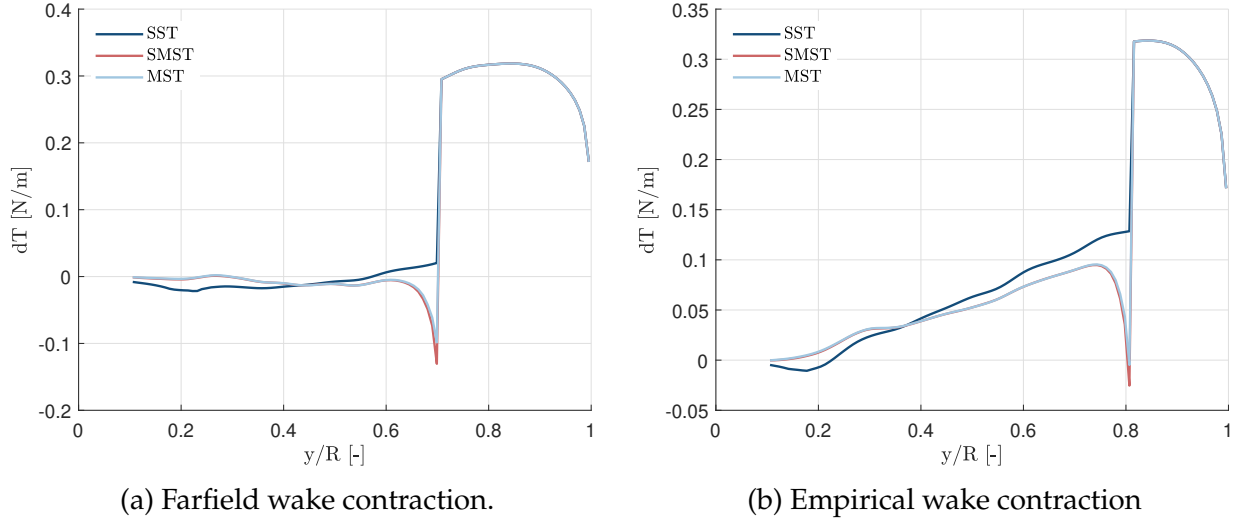


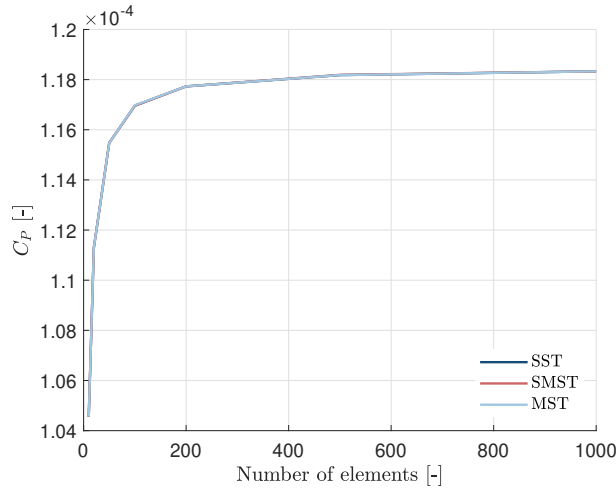
Figure 38: Comparison of the thrust distribution on the T-MOTOR G28x9.2 carbon fiber lower rotor (cf. Tables A.16 and A.18) for each of the coaxial models.

Negative thrust is observed for the models exhibiting negative angles in the velocity triangles, both at 20 percent span and at 65 percent span. Furthermore, it is observed that the relationships between the models are consistent with what is observed for the velocity triangles: smaller angles of attack indeed result in higher thrust.

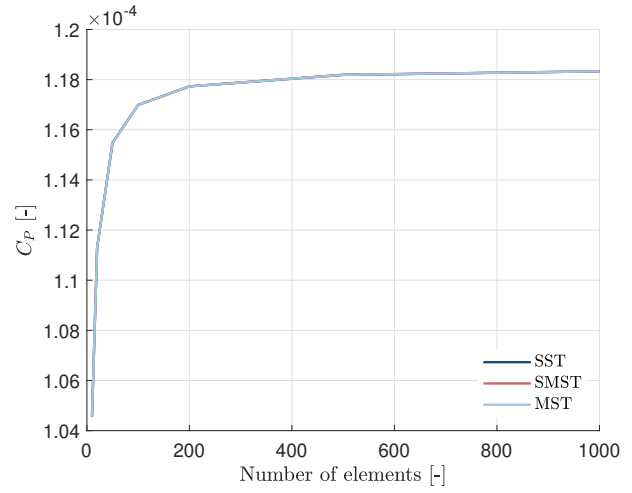
Moving forward, further investigation into model differences was pursued by examining result convergence relative to the number of elements. Figures 39 and 40 illustrate this convergence for performance parameters  $C_T$  and  $C_P$  for the first Harrington's lower rotor. This analysis is conducted for both the far-field assumption and the empirical model used to predict radial contraction. It is noteworthy that results considering variable and constant wake contraction ratios were differentiated in the latter case.

It is observed that the power coefficient converged uniformly across all models, regardless of the type of coaxial or contraction model employed. For the thrust coefficient, it has been observed that the SST model requires fewer elements overall compared to the other two coaxial models to achieve a converged solution. Furthermore, it has been noted that the  $C_T$  values to which the different models converge are more similar when the far-field assumption is employed. Conversely, when the empirical formula is utilized, the differences between the models become more pronounced. Additionally, it has been observed that when a variable wake contraction ratio is employed for the MST model, the results remain relatively similar to those obtained with a constant wake contraction ratio. However, this is not the case for



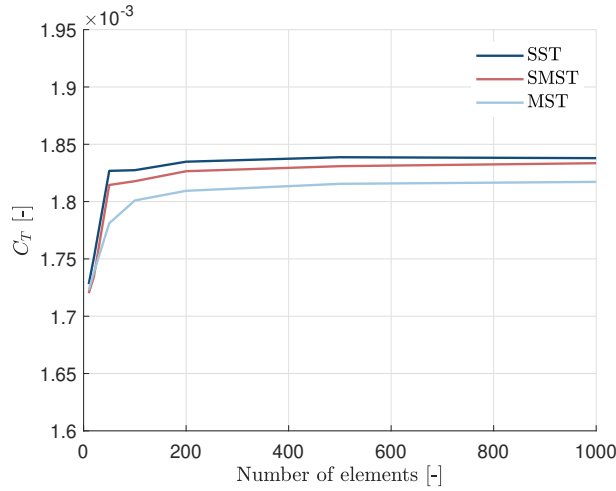


(a) Farfield wake contraction.

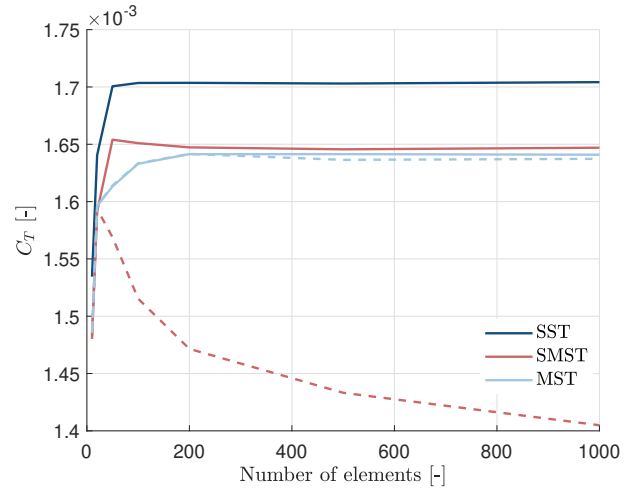


(b) Empirical wake contraction

Figure 39: Evolution of the Harrington rotor 1 power coefficient (cf. Tables A.10 and A.15) with the number of blade elements for each coaxial model. Note that the empirical graph uses '-' for a constant wake contraction ratio  $\bar{a}$  and '-' for a variable wake contraction ratio  $a(y)$ .



(a) Farfield wake contraction.



(b) Empirical wake contraction

Figure 40: Evolution of the Harrington rotor 1 thrust coefficient (cf. Tables A.10 and A.15) with the number of blade elements for each coaxial model. Note that the empirical graph uses '-' for a constant wake contraction ratio  $\bar{a}$  and '-' for a variable wake contraction ratio  $a(y)$ .

the SMST model. With a variable wake contraction ratio, the solution does not converge and tends to diverge from the solution with a constant wake contraction ratio. These observations are consistent with the upstream velocity distribution and inflow ratio on the lower rotor as

discussed in the previous section.

The investigation into the differences between the coaxial models will be extended by examining whether mass conservation is accurately maintained for each model. Indeed, ensuring the conservation among the following three mass flows is essential:

1. Mass flow across the entire previous rotor disk.
2. Mass flow in the wake after the contraction of the slipstream.
3. Mass flow on lower rotor elements inside the vena contracta after interpolation of the wake.

The difference between the first two mass flows will be zero by definition. However, an error may arise between the contracted wake and the lower rotor elements inside the vena contracta after the interpolation of the wake. Specifically, to obtain the upstream velocity on the lower rotor, the velocity in the contracted wake is interpolated from the contracted elements of the upper disk onto the elements of the lower disk. The relative conservation error between these two mass flows can be written as follows:

$$\xi = \frac{\dot{m}_{w,upper} - \dot{m}_{d,lower*}}{\dot{m}_{w,upper}}. \quad (4.3)$$

Where,  $\dot{m}_{d,lower*}$  denotes the mass flow on the lower rotor elements within the vena contracta. Figure 41 illustrates the evolution of the error with the number of elements for each coaxial model.

It is observed that for all models, except the SMST model with a variable wake contraction ratio, the error decreases as the number of elements increases. In the case of the SMST model with a variable wake contraction ratio, the error continuously increases and diverges. Notably, the error shown in the graph is in absolute value, but for the SMST model, the error is actually negative. This indicates that the mass flow after the upstream velocity interpolation on the lower rotor blade elements is significantly greater than the mass flow in the wake, resulting in an overestimation of the upstream velocity at the lower rotor disk. This phenomenon can explain why, for this model with variable wake contraction, the thrust coefficient continuously decreases as the number of elements increases (Figure 40b). Since an increase in the number of elements leads to a larger upstream mass flow perceived by the lower rotor, the inflow angle will also be increased (cf. Equation 2.21), and consequently the thrust produced by the blade will be reduced (cf. Equation 2.26). In conclusion, it can be stated that the SMST model is unsuitable for use with a variable wake contraction ratio.

Furthermore, the MST model exhibits the smallest mass flow conservation error compared to all other models. This error approaches even a negligible value both under the far-field assumption and when using the empirical formula. Conversely, for the other models, even with a large number of elements, the mass flow error always retains a residual value. This

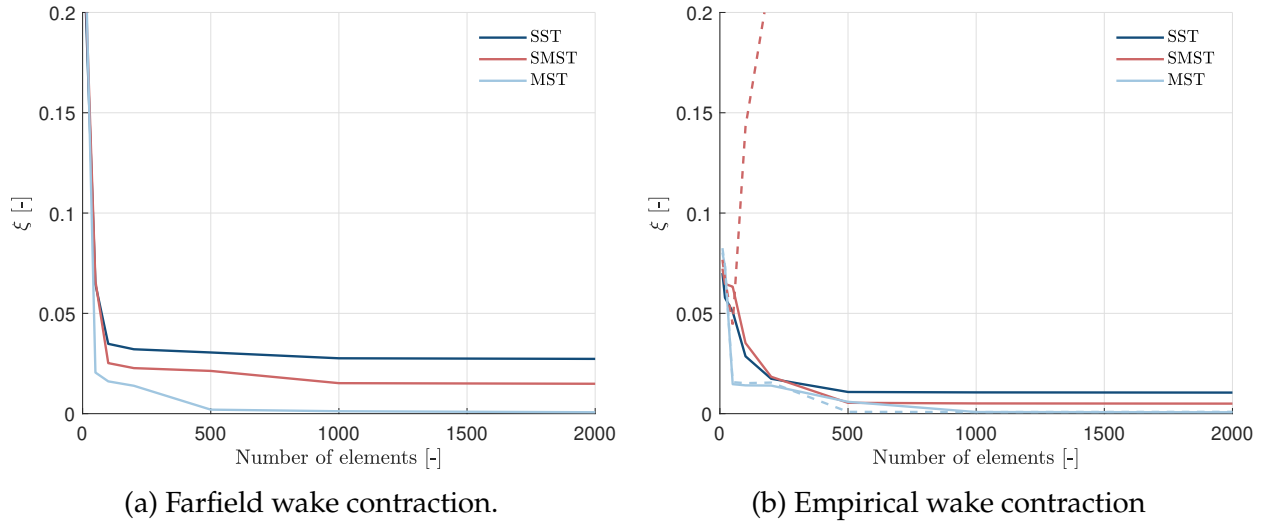


Figure 41: Evolution of the relative error on the mass flow for the Harrington rotor 1 (cf. Tables A.10 and A.15) with the number of blade elements for each coaxial model. Note that the empirical graph uses '-' for a constant wake contraction ratio  $\bar{a}$  and '- -' for a variable wake contraction ratio  $a(y)$ .

residual value is a few percent when the far-field assumption is applied and is slightly smaller when the radial contraction imposed by the empirical model is used.

A final point of comparison concerns the computation time required to evaluate performance at a given operating point. Figure 42 illustrates this time for each model as a function of the number of elements, specifically for the first rotor of Harrington. It is observed that computation time increases almost linearly with the number of elements. The computation times are substantially higher compared to the single-rotor case due to the iterative process over the torque, which significantly lengthens the overall computation process.

Despite the inherent simplicity of the SST model, it does not exhibit superior computational speed compared to other models. Conversely, the simplified multiple stream tube model exhibits a faster computation time than the general model. However, this difference is marginal. Therefore, it may be more prudent to prioritize the most accurate model, which achieves convergence with fewer elements, to minimize computation time.

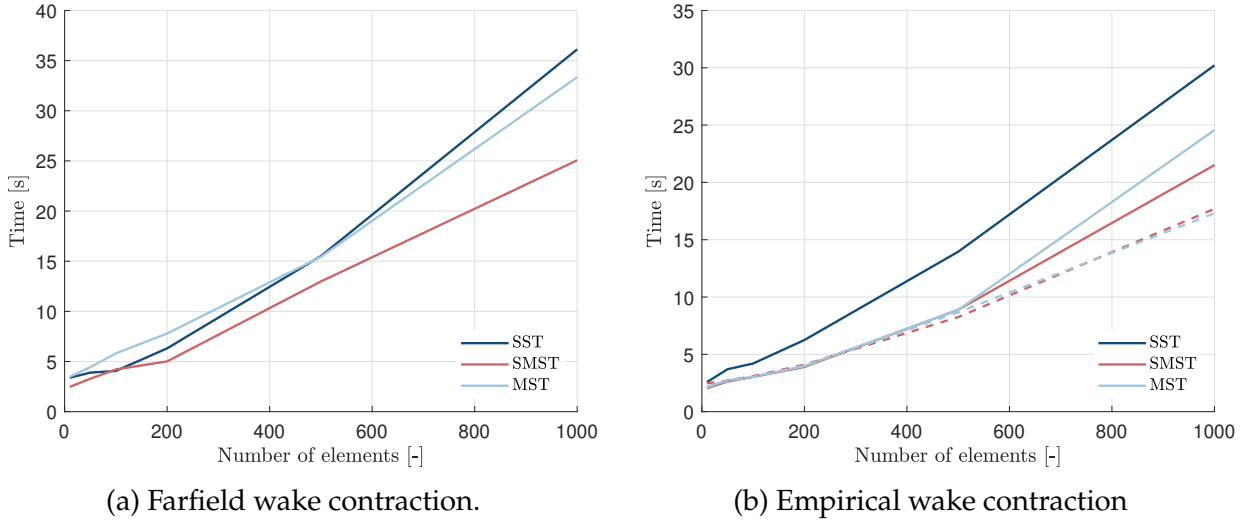


Figure 42: Evolution of the computational time for the Harrington rotor 1 (cf. Tables A.10 and A.15) with the number of blade elements for each coaxial model. Note that the empirical graph uses ‘-’ for a constant wake contraction ratio  $\bar{a}$  and ‘- -’ for a variable wake contraction ratio  $a(y)$ .

### 4.3 Summary

Throughout this section, the validity of the models implemented in Rotare has been demonstrated. Initially, for the single-rotor case, it was shown that the results obtained using each of the different methods to solve the system of equations 2.42 corresponded reasonably well with experimental data. The induced velocities approach was identified as the method that provided the most accurate and efficient results.

Subsequently, for the coaxial rotor configuration, the coaxial models were also validated in the hover case. It was observed that these models produced results generally in agreement with experimental data. The wake contraction ratio was found to have a significant impact. indeed, the results were much more precise when the wake contraction ratio was accurately estimated, compared to assuming that the lower rotor is situated within the fully developed wake of the upper rotor.

Finally, it was noted that, although the models produced very similar results, the general multiple stream tube model exhibits the highest fidelity in representing velocity and angle distributions on the lower rotor. Moreover, it also minimizes the error in mass conservation and doesn’t require significantly more computation time than the other models. Therefore, the MST model is recommended as the most suitable choice for design purposes.

## 5 Design

In a more in-depth study, it would be interesting to propose an optimal design configuration aimed at maximizing the efficiency of the coaxial rotor through various joint designs and control strategies. For instance, the optimal design for the blades, which are manufactured and tested by the industry Generix, could be identified. This identification process could be facilitated through BEMT simulations and the code implemented in Rotare.

Prior to proposing a design, it is essential to verify that the thrust generated by the code aligns with the experimentally measured thrust provided by Generix. Failure to achieve this alignment may result in a design that does not meet the necessary flight conditions for the drone. Additionally, it is critical to confirm that a torque balance achieved by the computational code is also observed experimentally. Alternatively, this can be verified by ensuring that for Generix's experimental measurements, where the torque is balanced, the BEMT simulations yield corresponding results.

This validation process is depicted in Figure 43. The results are compared for the contra-rotating coaxial rotor consisting of SAB 280 mm blades as described in Table A.19, where the operating conditions (rotational speed and collective pitch) have been determined by the company to cancel the torque.

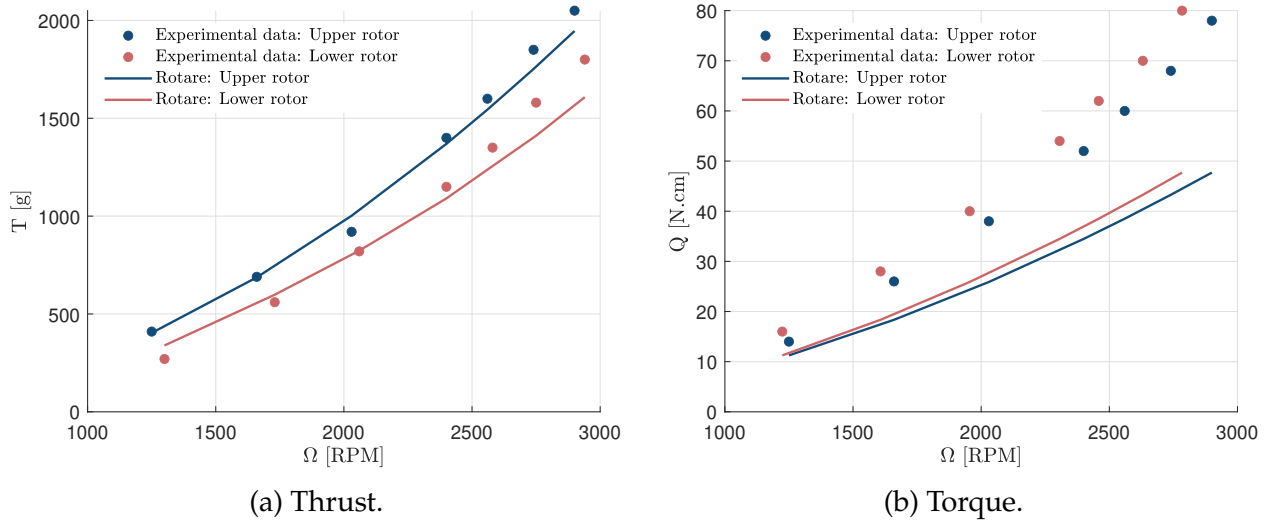


Figure 43: Comparison between the results from Rotare and the experimental measurements from Generix for the counter-rotating coaxial rotor with SAB blades (cf. Table A.19).

Firstly, it is observed that the thrust generated and calculated using Rotare is closely aligned with the measurements obtained by Generix. It should be noted that as the rotational speed increases, the thrust tends to be slightly underestimated by the BEMT, particularly for the lower rotor. Specifically, when approaching 3000 RPM, there is a relative error of approxi-

ately 5% for the upper rotor and 10% for the lower rotor. This discrepancy must be taken into account during the design phase.

Secondly, it is evident that the torque measured by Rotare shows significant deviations from the experimentally measured torque. However, despite these differences, the differential torque between each rotor remains relatively small. To illustrate this further, it is essential to analyze and compare this differential torque at each operational point, as detailed in Table 2.

Rotor angular velocity [RPM]		Differential Torque [N.cm]	
Upper	Lower	Experimental	From Rotare
1250	1300	2	1.66
1660	1730	2	3.26
2030	2060	2	3.08
2400	2400	2	2.99
2560	2580	2	4.11
2740	2750	2	4.19
2900	2940	2	5.83

Table 2: Comparison between differential torque values from Rotare (cf. Table A.19) and measurements by Generix.

The data clearly indicates that the torque is nearly balanced at most operational points, except under high angular velocities. It would be beneficial to investigate the angular velocity values for the lower rotor that would have been obtained if the torque cancellation method implemented in Rotare had been used. Table 3 presents these angular velocities and compares them with the values provided by Generix.

Experimental Angular Velocities [RPM]		Rotare Angular Velocities [RPM]	
Upper Rotor	Lower Rotor	Upper Rotor	Lower Rotor
1250	1300	1250	1228.5
1660	1730	1660	1612.6
2030	2060	2030	1961.0
2400	2400	2400	2312.7
2560	2580	2560	2465.8
2740	2750	2740	2638.4
2900	2940	2900	2792.0

Table 3: Comparison between upper and lower rotors angular velocities for a balanced torque from Rotare (cf. Table A.19) and measurements by Generix.

It can be observed that in contrast to the measurements provided by Generix, the angular velocity predicted by the code for torque cancellation is consistently lower than that of the upper rotor. This results in a discrepancy between the experimental measurements and the

simulations, ranging from 70 RPM to nearly 150 RPM. This discrepancy must also be taken into account during the design phase.

When considering the design, the primary objective is to optimize efficiency. In the subsequent section, the variation of efficiency with respect to specific parameters will be analyzed. The purpose is to qualitatively assess the impact of these parameter variations. A detailed investigation into the optimal configuration will be deferred to a more in-depth study.

### 5.1 The effect of variation in differential collective pitch.

One parameter that can be studied is the differential collective pitch. Indeed, The impact of increasing the lower rotor's pitch relative to the upper rotor on efficiency can be analyzed. In Figure 44, the efficiency curve for a coaxial rotor system with SAB blades, as described in Table A.20, is illustrated as a function of the differential collective pitch for two different angular velocities. It is important to note that these velocities refer exclusively to the upper rotor, while the angular velocity of the lower rotor is adjusted at each data point to cancel out the torque.

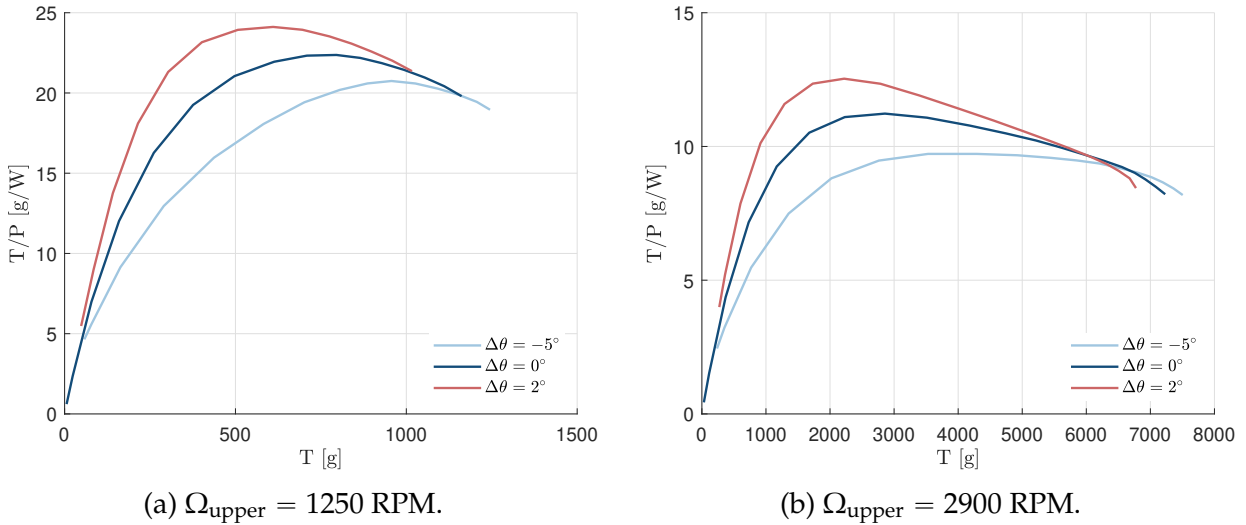


Figure 44: Evolution of the efficiency for a coaxial rotor system with SAB blades (cf. Table A.20) as a function of the differential collective pitch.

It can be observed that increasing the pitch of the lower rotor enhances efficiency. Furthermore, the peak efficiency is observed to occur at lower thrust values when the lower rotor's pitch is greater, and conversely.

## 5.2 The effect of the variation of the airfoil geometry.

The influence of airfoil selection on performance may also be considered. In this analysis, the SAB blades from Generix, incorporating NACA 4-digit airfoils, are examined. Performance curves presented in Figure 45 illustrate variations in airfoil thickness and camber. These variations enable a separate evaluation of the impact of each parameter on overall performance.

The figure clearly indicates that as the airfoil thickness increases, the performance tends to decrease. Indeed, thicker airfoils generally produce higher drag, which negatively impacts overall efficiency. However, a thicker airfoil provides enhanced structural integrity, crucial for supporting greater loads and withstanding mechanical stresses. Furthermore, thicker airfoils are capable of generating higher lift. Consequently, the selection of airfoil thickness involves a critical balance between aerodynamic efficiency and structural demands.

The camber of an airfoil is generally employed to enhance lift generation at a given angle of attack. An airfoil with a significant camber will stall at a higher angle of attack compared to a symmetrical or less cambered profile. However, a more pronounced camber not only generates more lift but also increases drag. Consequently, at lower rotational speeds, it is observed that a more cambered profile tends to decrease overall efficiency. In contrast, at high rotational speeds, the lift becomes more significant, and this trend reverses. Therefore, it is evident that the choice of airfoil geometry is a critical parameter that can greatly influence rotor performance. It must be selected carefully based on the specific requirements of the application to achieve the optimal balance between enhanced lift, increased stall angle, structural integrity, and overall efficiency.

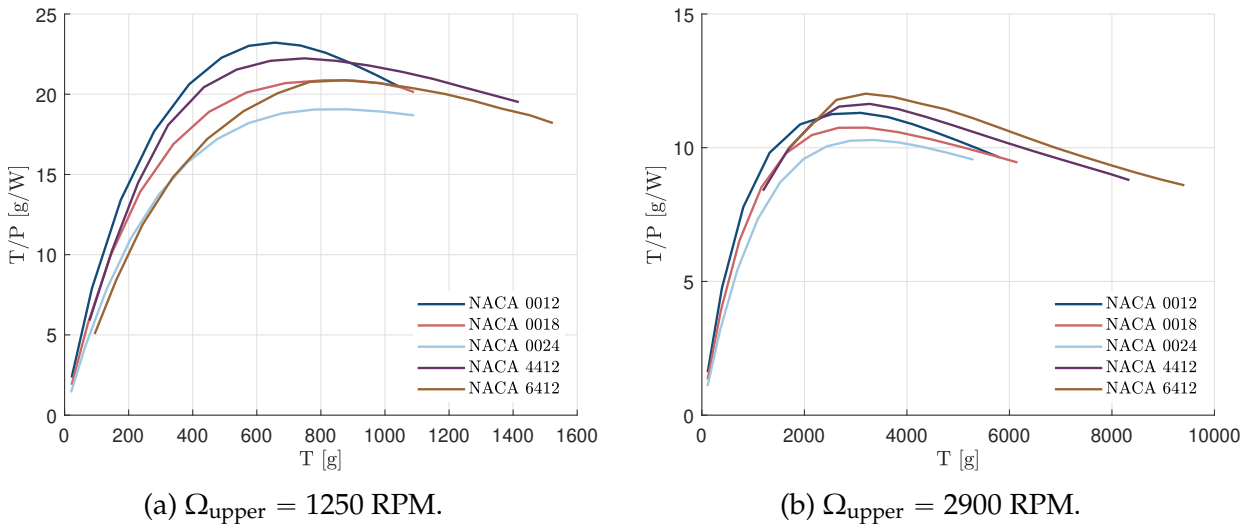


Figure 45: Evolution of the efficiency for a coaxial rotor system with SAB blades (cf. Table A.20) as a function of the airfoil geometry.



### 5.3 The effect of the variation of the chord length.

It is also pertinent to analyze the effect on the performance of varying the blade chord length, either by increasing or decreasing it. This influence is illustrated in Figure 46. It is observed that efficiency is significantly reduced as the chord length increases, primarily due to the corresponding rise in drag. However, a larger chord also enhances the lift and is essential for achieving adequate thrust. Thus, the chord size is a critical factor that must be carefully considered in rotor design.

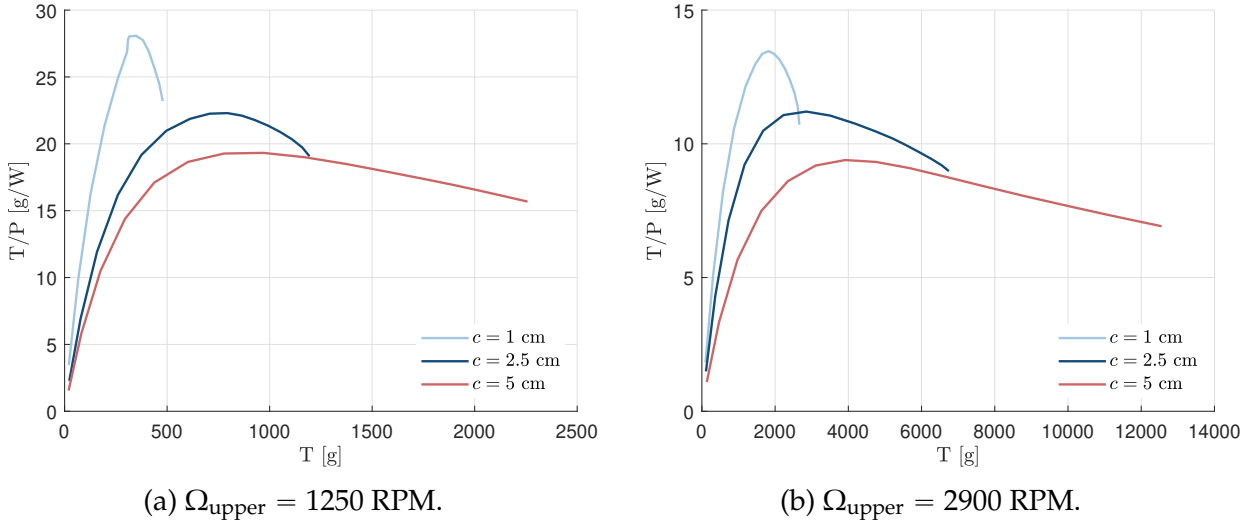


Figure 46: Evolution of the efficiency for a coaxial rotor system with SAB blades (cf. Table A.20) as a function of the chord length.

### 5.4 The effect of the variation of the inter-rotor distance.

It is also interesting to consider the effect of the inter-rotor distance. A compact design is often preferred by manufacturers. However, a reduced distance between the rotors amplifies the influence of the upper rotor on the lower rotor. The reciprocal influence, though not incorporated in the Rotare calculation, is also intensified. This amplification is anticipated to result in decreased efficiency.

Utilizing the empirical model, the influence of varying distances between the lower and upper rotors can be quantified. In hover, radial contraction exhibits exponential growth inversely proportional to the rotor separation distance (refer to equations 3.16 and 3.18). Consequently, as this distance increases, it asymptotically approaches a value of 0.78. Conversely, if it decreases, it tends towards 1.

The actual effect of this distance on the efficiency of the coaxial rotor, as presented in Table A.20, is illustrated in Figure 47. It can be seen that both the inter-rotor distance and the

resultant contraction exert minimal influence on efficiency, according to the empirical model. Nevertheless, in practical applications, this impact may be more pronounced.

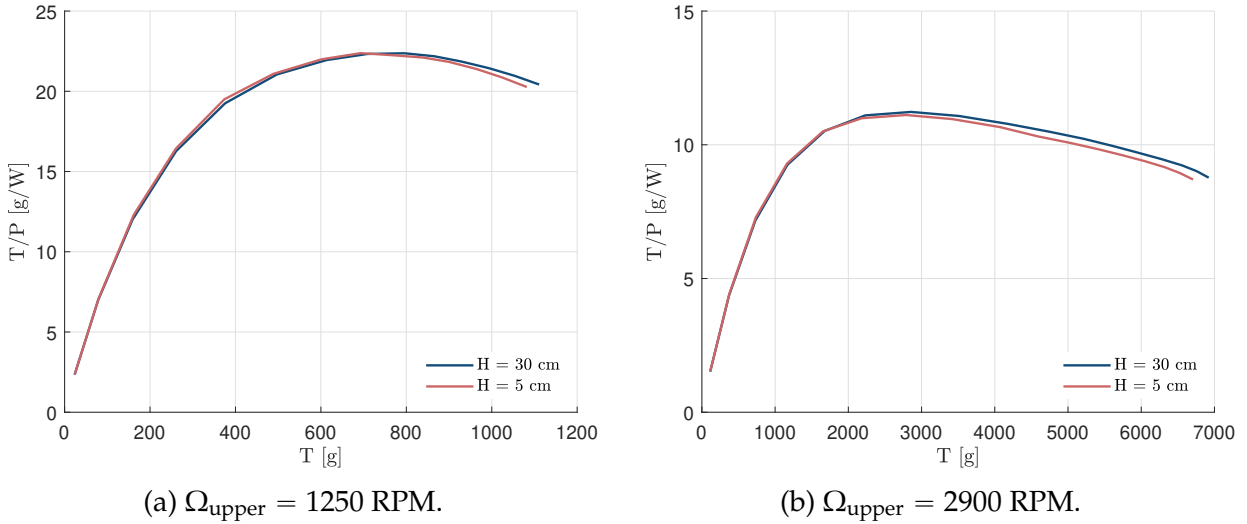
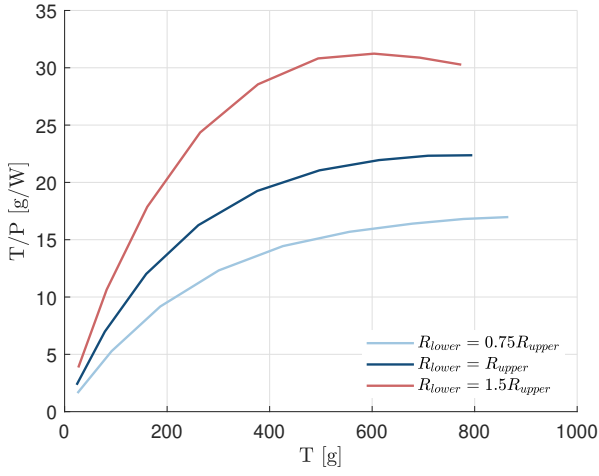


Figure 47: Evolution of the efficiency for a coaxial rotor system with SAB blades (cf. Table A.20) as a function of the distance between the rotors.

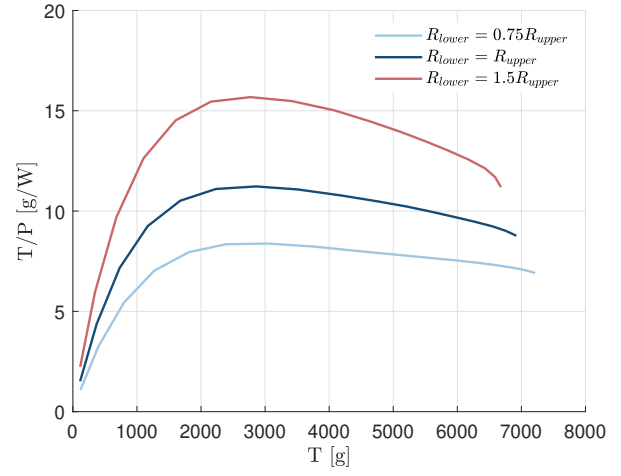
## 5.5 The effect of the variation in differential blade diameters.

The impact of differential blade diameters can also be considered. since a part of the lower rotor resides within the vena contracta of the upper rotor, efficiency is reduced in this region, thereby affecting the overall performance of the coaxial system. By increasing the diameter of the lower rotor or reducing that of the upper rotor, a larger "clean" zone, i.e., a larger area unaffected by the upper rotor, could be achieved, thus enhancing efficiency.

Figure 48 illustrates the effect of differential blade diameters on the coaxial rotor equipped with SAB blades, as specified in Table A.20. It can be observed that the effect is quite significant. Consequently, further investigation into this parameter is recommended to achieve an optimal balance between efficiency and compact design.



(a)  $\Omega_{\text{upper}} = 1250$  RPM.



(b)  $\Omega_{\text{upper}} = 2900$  RPM.

Figure 48: Evolution of the efficiency for a coaxial rotor system with SAB blades (cf. Table A.20) as a function of differential blade diameters.

## 6 Conclusion

This thesis has explored the potential of coaxial rotor designs, focusing on the validation and enhancement of BEMT and coaxial models developed in the Rotare code. The motivation for this research stemmed from the need to improve UAV performance in various applications, leveraging the unique advantages of coaxial rotors, such as superior lift-to-drag ratio and intrinsic torque cancellation.

The theoretical groundwork laid out in this study included revisiting the Momentum Theory and Blade Element Theory and introducing necessary corrections and modifications to the existing BEMT implementation in ROTARE. Significant improvements were made to account for tangential velocity interactions, and accurate wake contraction, enhancing the coaxial model's fidelity.

The validation process rigorously compared Rotare's model predictions with experimental data for both single and coaxial rotor configurations. In the case of a single rotor, the model was validated for hover and axial flight conditions, showing good agreement with experimental results in both scenarios. The induced velocities approach was identified as the most accurate and efficient for the single-rotor case and thus was utilized throughout the study. At higher blade angles, stall phenomena were observed at low speeds, causing deviations from expected outcomes. However, the BEMT model effectively accounted for stall effects. Furthermore, the influence of airfoil characteristics on the solution was highlighted, emphasizing the importance of using accurate airfoil polars in the code.

For coaxial rotors, the model was validated specifically for hover conditions. It was demonstrated that accurately estimating the wake contraction ratio was crucial for enhancing model precision. Additionally, incorporating the interaction of tangential velocities between rotors significantly influenced the outcomes. While the efficiency of the lower rotor remains largely unaffected by this tangential velocity, thrust generation is impacted by this addition. Among the evaluated models, the Multiple Stream Tube (MST) model demonstrated superior fidelity in representing velocity and angle distributions, and it effectively maintained optimal mass flow conservation, all while maintaining computational efficiency. Consequently, the MST model is recommended as the most suitable choice for rotor design purposes. When considering advancing propellers, obtaining high-fidelity validation data posed challenges, particularly in determining the validity of empirical models such as those described by Favier [15]. Therefore, future studies should include wind tunnel tests or a CFD analysis on specific coaxial systems to validate performance predictions under advancing propeller conditions.

The design phase underscored the potential for optimizing coaxial rotor systems through BEMT simulations. This investigation focused on counter-rotating coaxial rotors equipped with SAB blades, manufactured and tested by the Generix company. For this rotor, the thrust measurements obtained from Generix closely matched the computational predictions, validating the model's reliability. Furthermore, the balance of torque between the upper and lower rotors, as predicted by the computational model, aligns with critical design parameters have

been identified as essential for enhancing drone performance. Among these, the collective pitch of the lower rotor emerges as a key variable that can be optimized to achieve peak efficiency. Additionally, factors such as airfoil geometry, chord length, and differential blade diameters significantly influence overall performance. These aspects could be the focus of a more in-depth study using the BEMT code implemented in Rotare.

In summary, this thesis validated the enhanced BEMT model for coaxial rotors and demonstrated its applicability in optimizing UAV rotor designs. Furthermore, the design phase underscored the effectiveness of BEMT simulations in optimizing coaxial rotor systems. It also identified several key design parameters that, if studied further, could lead to improved efficiency.

# Bibliography

- [1] Eli B. Giovanetti. "Optimal Aerodynamic Design of Conventional and Coaxial Helicopter Rotors in Hover and Forward Flight". Dissertation. Department of Mechanical Engineering and Materials Science: Duke University, May 2015.
- [2] J. Gordon Leishman. *Principles of helicopter aerodynamics*. Second edition. Cambridge aerospace series. New York: Cambridge University Press, 2006. ISBN: 0-521-85860-7.
- [3] A.J. Ruddell, W. Groth and R. McCutcheon. *Advancing Blade Concept (ABC) Technology Demonstrator*. Tech. rep. USAAVRADCOM-TR-81-D-5. Sikorsky Aircraft Division of United Technologies Corporation, 1981.
- [4] Felice Cardito et al. "State-space coaxial rotors inflow modelling derived from high-fidelity aerodynamic simulations". In: *CEAS Aeronautical Journal* 9 (May 2018), pp. 587–606. DOI: 10.1007/s13272-018-0301-8. URL: <https://doi.org/10.1007/s13272-018-0301-8>.
- [5] Vincent M. Paglino. "Forward Flight Performance of a Coaxial Rigid Rotor". In: 1971. URL: <https://api.semanticscholar.org/CorpusID:126297529>.
- [6] E.B. Giovanetti. "Optimal Aerodynamic Design of Conventional and Coaxial Helicopter Rotors in Hover and Forward Flight". MA thesis. Department of Mechanical Engineering and Materials Science: Duke University, 2015.
- [7] Thomas Lambert. "Experimental and Numerical Analysis of Unsteady Rotating and Flapping Multi-Wing Systems". To be published. PhD thesis. Liège, Belgium: University of Liège, 2024.
- [8] Conor William Stahlhut. "Aerodynamic Design Optimization of Proprotors for Convertible-Rotor Concepts". Thesis submitted in partial fulfillment of the requirements for the degree of Master of Science. MA thesis. College Park, MD: University of Maryland, College Park, May 2012.
- [9] S.F. Ramdin. "Prandtl Tip Loss Factor Assessed". Master of Science Thesis, Faculty of Aerospace Engineering. MA thesis. Delft University of Technology, Jan. 2017.
- [10] Y. El Khchine, A. Author2 and B. Author3. "Tip Loss Factor Effects on Aerodynamic Performances of Horizontal Axis Wind Turbine". In: *Energy Procedia* 118 (2017), pp. 136–140. DOI: 10.1016/j.egypro.2017.03.030.

- [11] Emmanuel Branlard. *Wind Turbine Aerodynamics and Vorticity-Based Methods: Fundamentals and Recent Applications*. Vol. 123. Research Topics in Wind Energy. Cham, Switzerland: Springer International Publishing, 2017. ISBN: 978-3-319-55163-0. DOI: 10.1007/978-3-319-55164-7. URL: <https://doi.org/10.1007/978-3-319-55164-7>.
- [12] Koen Hillewaert. *Aerospace Propulsion*. Course AERO0014, Département Aérospatiale et Mécanique, Design of Turbomachines (DoT), University of Liège, Academic year 2022–2023. May 2023.
- [13] Hadi Winarto. *BEMT Algorithm for the Prediction of the Performance of Arbitrary Propellers*. Tech. rep. CR CoE-AL 2004-HW3-01. Australia: Centre of Expertise in Aerodynamic Loads, Royal Melbourne Institute of Technology, Mar. 2004.
- [14] Anton J. Landgrebe. *An Analytical and Experimental Investigation of Helicopter Rotor Hover Performance and Wake Geometry Characteristics*. Tech. rep. USAAMRDL Technical Report 71-24. U. S. Army Air Mobility Research and Development Laboratory. East Hartford, Connecticut: United Aircraft Corporation Research Laboratories, June 1971.
- [15] D. Favier and C. Maresca. “Étude du sillage 3D d’une hélice aérienne quadripale”. In: *AGARD-FOP on Aerodynamics and Acoustics of Propellers, CPP-366*. Paper N°15. Toronto, Canada, Oct. 1984.
- [16] J.D. Kocurek and J.L. Tangler. “A prescribed wake lifting surface hover performance analysis”. In: *Journal of the American Helicopter Society* 22.W1 (Jan. 1977), pp. 24–35.
- [17] Mark D. Maughmer and Michael S. Selig. *UIUC Propeller Database - Volume 1*. Accessed: 2024-05-17. 2019. URL: <https://m-selig.ae.illinois.edu/props/volume-1/propDB-volume-1.html>.
- [18] Muwanika Jdiobe et al. “Validation of a Wind Tunnel Propeller Dynamometer for Group 2 Unmanned Aircraft”. In: *Applied Sciences* 12.17 (2022), p. 8908. DOI: 10.3390/app12178908. URL: <https://doi.org/10.3390/app12178908>.
- [19] David Biermann and Edwin P. Hartman. *The Aerodynamic Characteristics of Six Full-Scale Propellers Having Different Airfoil Sections*. Technical Report Report No. 650. Langley Memorial Aeronautical Laboratory, 1935.
- [20] Alexander Meyer Ströborg. “Aerodynamic Analysis of Reflex Airfoils at Low Reynolds Numbers: A comparative study between XFOIL and CFD”. Degree Project in Technology. Stockholm, Sweden: KTH Royal Institute of Technology, 2022.
- [21] Kristen Kallstrom. *Exploring Airfoil Table Generation using XFOIL and OVERFLOW*. San Jose, CA, Jan. 2022.
- [22] Robert D. Harrington. *Full-Scale-Tunnel Investigation of the Static-Thrust Performance of a Coaxial Helicopter Rotor*. Tech. rep. Technical Note 2318. Langley Field, VA: National Advisory Committee for Aeronautics, Langley Aeronautical Laboratory, Mar. 1951.
- [23] J. Gordon Leishman and S. Ananthan. *An Optimum Coaxial Rotor System for Axial Flight*. Tech. rep. College Park, MD: Department of Aerospace Engineering, Glenn L. Martin Institute of Technology, University of Maryland, 2008.

- [24] J. Gordon Leishman and S. Ananthan. *Aerodynamic Optimization of a Coaxial Proprotor*. Tech. rep. College Park, Maryland 20742: Department of Aerospace Engineering, Glenn L. Martin Institute of Technology, University of Maryland, 2008.
- [25] K.E.T. Giljarhus, A. Porcarelli and J. Apeland. "Investigation of Rotor Efficiency with Varying Rotor Pitch Angle for a Coaxial Drone". In: *Drones* 6.4 (2022), p. 91. DOI: 10.3390/drones6040091. URL: <https://doi.org/10.3390/drones6040091>.



# Appendix A

## BEMT Configurations

<b>y/R [-]</b>	<b>c/R [-]</b>	<b>Pitch [°]</b>
0.15	0.109	53.88
0.20	0.127	54.60
0.25	0.142	49.63
0.30	0.153	43.66
0.35	0.160	38.79
0.40	0.162	34.70
0.45	0.161	31.36
0.50	0.156	28.62
0.55	0.149	26.21
0.60	0.139	24.26
0.65	0.128	22.64
0.70	0.116	21.07
0.75	0.103	19.55
0.80	0.090	18.27
0.85	0.077	17.21
0.90	0.066	16.54
0.95	0.051	14.29
1.00	0.036	11.88

Table A.1: Geometric parameters of the APC14x12 propeller.

Parameter	Value
$\Omega$ [RPM]	3500
Axial Velocity [m/s]	0
Collective Pitch [°]	0
Radius [m]	0.1778
Number of Blades [-]	2
Airfoil	NACA 4412
Pitch Reference	Chordline
Application	Propeller
Tip Loss	Taken into account

Table A.2: Technical information of the APC14x12 propeller.

Parameter	Value
$\Omega$ [RPM]	3500
Axial Velocity [m/s]	[3.7 19]
Collective Pitch [°]	0
Radius [m]	0.1778
Number of Blades [-]	2
Airfoil	NACA 4412
Pitch Reference	Chordline
Application	Propeller
Tip Loss	Taken into account

Table A.3: Technical information of the APC14x12 advanced propeller.

Parameter	Value
$\Omega$ [RPM]	[1500 3500]
Axial Velocity [m/s]	0
Collective Pitch [°]	0
Radius [m]	0.1778
Number of Blades [-]	2
Airfoil	NACA 4412
Pitch Reference	Chordline
Application	Propeller
Tip Loss	Taken into account

Table A.4: Technical information of the APC14x12 propeller in hover.

<b>y/R [-]</b>	<b>c/R [-]</b>	<b>Pitch [°]</b>
0.20	0.0360	46.8388
0.30	0.0525	41.7096
0.40	0.0700	36.7975
0.50	0.0760	31.9595
0.60	0.0735	28.4190
0.70	0.0660	26.3655
0.80	0.0565	24.1144
0.90	0.0450	22.8251
1.00	0.0330	22.3240

Table A.5: Geometric parameters of the 5868-9 propeller.

<b>Parameter</b>	<b>Value</b>
$\Omega$ [RPM]	800
Axial Velocity [m/s]	[12.2 50.8]
Collective Pitch [°]	0
Radius [m]	1.524
Number of Blades [-]	3
Airfoil	Clark-y
Pitch Reference	Chordline
Application	Propeller
Tip Loss	Taken into account

Table A.6: Technical information of the 5868-9 propeller.

<b>Parameter</b>	<b>Value</b>			
Blade angle	15°	20°	25°	30°
$\Omega$ [RPM]	1000	1000	800	800
Axial Velocity [m/s]	[15.2, 39.6]	[15.2, 50.8]	[12.2, 50.8]	[15.2, 61.7]
Collective Pitch [°]	-10	-5	0	5
Radius [m]	1.524			
Number of Blades [-]	3			
Airfoil	Clark-y			
Pitch Reference	Chordline			
Application	Propeller			
Tip Loss	Taken into account			

Table A.7: Technical information of the 5868-9 propeller with different blade angles.

Parameter	Value		
Blade angle	35°	40°	45°
$\Omega$ [RPM]	800	700	700
Axial Velocity [m/s]	[15.2, 73.6]	[10.7, 77.5]	[10.7, 92.81]
Collective Pitch [°]	10	15	20
Radius [m]	1.524		
Number of Blades [-]	3		
Airfoil	Clark-y		
Pitch Reference	Chordline		
Application	Propeller		
Tip Loss	Taken into account		

Table A.8: Technical information of the 5868-9 propeller with different blade angles.

Parameter	Value
$\Omega$ [RPM]	700
Axial Velocity [m/s]	17.8 , 46.2
Collective Pitch [°]	20
Radius [m]	1.524
Number of Blades [-]	3
Airfoil	Clark-y
Pitch Reference	Chordline
Application	Propeller
Tip Loss	Taken into account

Table A.9: Technical information of the 5868-9 propeller with 40° blade angle.

y/R [-]	c/R [-]	Pitch [°]	Airfoil
0.1600	0.0733	0	NACA 0030
0.2933	0.0667	0	NACA 0028
0.3067	0.0660	0	NACA 0026
0.5000	0.0567	0	NACA 0024
0.5800	0.0523	0	NACA 0023
0.7000	0.0453	0	NACA 0022
0.7667	0.0420	0	NACA 0021
0.8667	0.0367	0	NACA 0020
0.9333	0.0323	0	NACA 0018
1.0000	0.0293	0	NACA 0012

Table A.10: Geometric parameters of the blade for the first Harrington's rotor.

Parameter	Value
$\Omega$ (upper rotor) [RPM]	382
$\Omega$ (lower rotor) [RPM]	382
Axial Velocity [m/s]	0
Radius [m]	3.81
Number of Blades [-]	2
Application	Helicopter
Tip Loss	Taken into account
Torque	Balanced
Wake contraction	Empirical (constant wake contraction ratio)
Distance between rotors [cm]	70.9

Table A.11: Technical information for the first Harrington's rotor.

y/R [-]	c/R [-]	Pitch [°]	Airfoil
0.1600	0.1200	0	NACA 0028
0.3000	0.1200	0	NACA 0026
0.4267	0.1200	0	NACA 0024
0.5533	0.1200	0	NACA 0022
0.6800	0.1200	0	NACA 0020
0.8067	0.1200	0	NACA 0018
0.9333	0.1200	0	NACA 0016
1.0000	0.1200	0	NACA 0015

Table A.12: Geometric parameters of the blade for the second Harrington's rotor.

Parameter	Value
$\Omega$ (upper rotor) [RPM]	249.8
$\Omega$ (lower rotor) [RPM]	249.8
Axial Velocity [m/s]	0
Radius [m]	3.81
Number of Blades [-]	2
Application	Helicopter
Tip Loss	Taken into account
Torque	Balanced
Wake contraction	Empirical (constant wake contraction ratio)
Distance between rotors [cm]	61

Table A.13: Technical information for the second Harrington's rotor.

Parameter	Value
$\Omega$ (upper rotor) [RPM]	382
$\Omega$ (lower rotor) [RPM]	382
Axial Velocity [m/s]	0
Collective pitch (upper rotor) [ $^\circ$ ]	8.1
Collective pitch (lower rotor) [ $^\circ$ ]	8.4
Radius [m]	3.81
Number of Blades [-]	2
Application	Helicopter
Tip Loss	Taken into account
Torque	Balanced
Wake contraction	Empirical (constant wake contraction ratio)
Distance between rotors [cm]	70.9

Table A.14: Technical information for the first Harrington's rotor,  $C_T = 0.004$ .

Parameter	Value
$\Omega$ [RPM]	[1000 3000]
Axial Velocity [m/s]	0
Collective pitch [ $^\circ$ ]	0
Radius [m]	3.81
Number of Blades [-]	2
Application	Helicopter
Tip Loss	Taken into account
Torque	Not balanced
Wake contraction	Empirical (constant wake contraction ratio)
Distance between rotors [cm]	70.9

Table A.15: Technical information for the first Harrington's rotor.

<b>y/R [-]</b>	<b>c/R [-]</b>	<b>Pitch [°]</b>
0.1012	0.0304	16.9940
0.1509	0.0442	20.9580
0.2006	0.0571	22.2761
0.2504	0.0632	22.7382
0.3002	0.0702	20.3987
0.3515	0.0700	17.3588
0.4000	0.0700	15.4083
0.4513	0.0676	13.6916
0.4998	0.0647	12.3635
0.5497	0.0614	11.1135
0.5997	0.0585	10.3306
0.6510	0.0542	9.4697
0.7009	0.0503	8.7645
0.7509	0.0470	8.2927
0.7994	0.0433	7.7431
0.8507	0.0392	7.2713
0.9007	0.0351	6.8773
0.9506	0.0310	6.4055
1.0000	0.0271	6.0894

Table A.16: Geometric parameters of the T-MOTOR G28x9.2 carbon fiber rotor.

<b>Parameter</b>	<b>Value</b>
$\Omega$ (upper rotor) [RPM]	[1000 3000]
$\Omega$ (lower rotor) [RPM]	[1000 3000]
Axial Velocity [m/s]	0
Collective pitch (upper rotor) [°]	0
Collective pitch (lower rotor) [°]	0
Radius [m]	0.36
Number of Blades [-]	2
Airfoil	A18
Pitch Reference	Chordline
Application	Helicopter
Tip Loss	Taken into account
Torque	Not balanced
Wake contraction	Empirical (constant wake contraction ratio)
Distance between rotors [cm]	11.5

Table A.17: Technical information for the T-MOTOR G28x9.2 carbon fiber rotor.

Parameter	Value
$\Omega$ (upper rotor) [RPM]	1600
$\Omega$ (lower rotor) [RPM]	1600
Axial Velocity [m/s]	0
Collective pitch (upper rotor) [°]	0
Collective pitch (lower rotor) [°]	0
Radius [m]	0.36
Number of Blades [-]	2
Airfoil	A18
Pitch Reference	Chordline
Application	Helicopter
Tip Loss	Taken into account
Torque	Not balanced
Wake contraction	Empirical (constant wake contraction ratio)
Distance between rotors [cm]	11.5

Table A.18: Technical information for the T-MOTOR G28x9.2 carbon fiber rotor.

Parameter	Value
$\Omega$ (upper rotor) [RPM]	[1250 1660 2030 2400 2560 2740 2900]
$\Omega$ (lower rotor) [RPM]	[1300 1730 2060 2400 2580 2750 2940]
Axial Velocity [m/s]	0
Collective pitch (upper rotor) [°]	7.9
Collective pitch (lower rotor) [°]	9.4
Root radius [cm]	10
Tip radius [cm]	35
Chord [cm]	2.5
Twist [°]	0
Number of Blades [-]	2
Airfoil	Selig S8035
Tip Loss	Taken into account
Torque	Not balanced
Coaxial model	MST
Wake contraction	Empirical (constant wake contraction ratio)
Distance between rotors [cm]	30

Table A.19: Technical information for the blade SAB 280 mm.



Parameter	Value
$\Omega$ (upper rotor) [RPM]	1250 or 2900
$\Omega$ (lower rotor) [RPM]	Adapted to cancel out the torque
Axial Velocity [m/s]	0
Collective pitch [°]	[1 15] (same for both rotors)
Root radius [cm]	10
Tip radius [cm]	35
Chord [cm]	2.5
Twist [°]	0
Number of Blades [-]	2
Airfoil	Selig S8035
Tip Loss	Taken into account
Torque	Balanced
Coaxial model	MST
Wake contraction	Empirical (constant wake contraction ratio)
Distance between rotors [cm]	30

Table A.20: Technical information for the blade SAB 280 mm.